UNIVERSITAT POLITÈCNICA DE VALÈNCIA
DEPARTAMENT DE COMUNICACIONS

Novel multicore optical fibers for signal distribution and processing

PhD Thesis

Mario Ureña Gisbert

Supervisors:
Ivana Gasulla Mestre
Sergi García Cortijo

València, May 2023

Als de casa. A la meua estrela.

“May it be a light to you in dark places, when all other lights go out.”

J.R.R Tolkien

Agradecimientos

Para empezar, esta tesis no habría sido posible sin el apoyo recibido por parte de mis directores de tesis, Ivana y Sergi. En particular, a Ivana quisiera agradecerle la oportunidad de formar parte de este grupo de investigación y el poder realizar esta tesis doctoral. A Sergi me es imposible agradecerle completamente toda la ayuda, compañerismo y buenos consejos que me ha prestado a lo largo de todos estos años que hemos estado trabajando juntos.

Quiero agradecer también a todos mis compañeros en el PRL (en particular al *SDM team*) por contribuir a crear un entorno laboral agradable. De forma especial me gustaría agradecer a Rubén, Sergi (otra vez) y Javi por los buenos ratos en los descansos, comidas, actividades y demás momentos.

Despite being there for a short time, I would like to thank the people at the Max-Planck Institute in Erlangen for being so kind with me and for their assistance. In particular, I would like to acknowledge Dr. Michael Frosz, Linda Weise and Thomas Stelzer.

També vull agrair a tota la meua família el suport que m'han donat tots estos anys. En especial, als meus pares i a la meua germana, per animar-me a estudiar i ajudar-me sempre en tot.

Por último, quiero agradecer a mis amigos y compañeros de carrera todo el interés y el apoyo recibido todos estos años. Por supuesto, no habría podido superar el largo camino para llegar hasta aquí sin el apoyo de Esther, gracias por compartir conmigo los buenos y los malos momentos.

Abstract

Space-division multiplexing fibers emerged in the last decade as a solution to the capacity bottleneck in single-mode optical fiber communication networks. They utilize space, the last multiplexing technique in optical communications, to increase the total capacity in digital communications whilst reducing space needs. Multicore fibers, a type of space-division multiplexing fibers comprised of multiple individual cores within the same cladding, are promising for long-reach communications because of their immediate compatibility with current fiber networks. Moreover, multicore fibers have raised interest in other fields of application such as data-center interconnects, quantum communications, radio access networks and Microwave Photonics. Apart from that, these fibers exhibit great potential not only for signal distribution but also for signal processing. Signal processing functionalities can benefit significantly from using these fibers in terms of compactness and weight, while assuring broadband versatility, reconfigurability, and performance stability.

In this Thesis, we propose the exploitation of the inherent parallelism found in multicore fibers to implement distributed signal processing for optical and microwave signals. First, we study the realization of a key optical component in Microwave Photonics signal processing, the sampled true-time delay line, with heterogeneous multicore fibers. This comprises the performance validation of a previously fabricated heterogeneous 7-core fiber, the experimental demonstration of microwave signal processing functionalities including signal filtering, optical beamforming, and arbitrary waveform generation, and the design and fabrication of a heterogeneous 19-core fiber that behaves as a tunable true-time delay line. This fiber was fabricated by scaling down 3 different preforms, each with a specific refractive index profile, with a different ratio to obtain cores with determined propagation characteristics. Lastly, we propose different custom heterogeneous multicore fiber designs for novel optical signal distribution and processing applications, including quantum key distribution, parallel chromatic dispersion compensation and parallel temporal Talbot effects.

Resumen

Las fibras de multiplexación por división espacial surgieron en la última década como solución al cuello de botella en la capacidad en las redes de comunicación de fibra óptica monomodo. Utilizan el espacio, la última técnica de multiplexación en comunicaciones ópticas, para aumentar la capacidad total en comunicaciones digitales al tiempo que reducen las necesidades de espacio. Las fibras multinúcleo, un tipo de fibras de multiplexación por división espacial compuestas por varios núcleos individuales dentro de la misma cubierta, son prometedoras para las comunicaciones de largo alcance por su compatibilidad inmediata con las redes de fibra actuales. Además, las fibras multinúcleo han despertado interés en otros campos de aplicación, como las interconexiones de centros de datos, las comunicaciones cuánticas, las redes de acceso radio y la Fotónica de Microondas. Además, estas fibras presentan un gran potencial no sólo para la distribución de señales, sino también para su procesado. Las funcionalidades de procesado de señal pueden beneficiarse significativamente del uso de estas fibras en términos de compacidad y peso, garantizando al mismo tiempo versatilidad, reconfigurabilidad y rendimiento estable de banda ancha.

En esta Tesis, proponemos la explotación del paralelismo inherente que se encuentra en las fibras multinúcleo para implementar el procesado distribuido de señales ópticas y de microondas. En primer lugar, estudiamos la realización de un componente óptico clave en el procesado de señales en Fotónica de Microondas, la línea de retardo en tiempo real muestreada, con fibras multinúcleo heterogéneas. Esto comprende la validación del rendimiento de una fibra heterogénea de 7 núcleos previamente fabricada, la demostración experimental de las funcionalidades de procesado de señales de microondas; incluyendo el filtrado de señales, la conformación óptica de haces y la generación de formas de onda arbitrarias; y el diseño y fabricación de una fibra heterogénea de 19 núcleos que se comporta como una línea de retardo en tiempo real sintonizable. Esta fibra se fabricó escalando 3 preformas diferentes, cada una con un perfil de índice refractivo específico, para obtener núcleos con unas características de propagación determinadas. Por último, proponemos diferentes diseños de fibras multinúcleo heterogéneas específicos para aplicaciones novedosas de distribución y procesado de señales ópticas, incluyendo la distribución de claves cuánticas, la compensación paralela de la dispersión cromática y los efectos Talbot temporales paralelos.

Resum

Les fibres de multiplexació per divisió espacial van sorgir en la darrera dècada per a solucionar el coll de botella en la capacitat de les xarxes de comunicació de fibra òptica monomode. Utilitzen l'espai, l'última tècnica de multiplexació en comunicacions òptiques, per a incrementar la capacitat total en comunicacions digitals al mateix temps que redueixen les necessitats espacials. Les fibres multinucli, un tipus de fibres de multiplexació per divisió espacial compostes per diversos nuclis individuals situats dins la mateixa coberta, són prometedores per a les comunicacions de llarg abast per la immediata compatibilitat amb les xarxes de fibra òptica actuals. Per aquest motiu, les fibres multinucli han despertat interès en altres àmbits d'aplicació, com les interconnexions de centres de dades, les comunicacions quàntiques, les xarxes d'accés radio i la Fotònica de Microones. A més, aquestes fibres presenten un gran potencial no només per a la distribució de senyals, sinó també per al seu processament. Les funcionalitats de processament de senyals poden beneficiar-se significativament del seu ús en relació a la compacitat i al pes, mentre garanteixen versatilitat, reconfigurabilitat i rendiment estable de banda ampla.

En aquesta Tesi, proposem l'explotació del paral·lelisme inherent de les fibres multinucli per a implementar processament distribuït de senyals òptiques i de microones. En primer lloc, estudiem la realització d'un component òptic clau en el processament de senyals en la Fotònica de Microones, la línia de retard en temps real mostrejada, amb fibres multinucli heterogènies. Això comprèn la validació del rendiment d'una fibra de heterogènia 7 nuclis fabricada prèviament, la demostració experimental de les funcionalitats de processament de senyals de microones sobre aquesta mateixa fibra; la qual cosa inclou el filtrat de senyals, la conformació òptica de feixos i la generació de formes d'ona arbitràries; i el disseny i fabricació d'una fibra heterogènia de 19 nuclis que es comporta com una línia de retard en temps real sintonitzable. Aquesta fibra es va fabricar escalant 3 preformes diferents, cadascuna amb un perfil d'índex refractiu específic, per obtindre nuclis amb característiques de propagació determinades. Per últim, proposem diversos dissenys específics de fibres multinucli heterogènies per a aplicacions innovadores de distribució i processament de senyals òptiques, incloent la distribució de claus quàntiques, la compensació paral·lela de la dispersió cromàtica i els efectes Talbot temporals en paral·lel.

Contents

List of Figures

List of Tables

List of Acronyms

5G: 5th generation

AF: array factor

AWG: arbitrary waveform generation

BS: broadband source

CSE: carrier suppression effect

CME: coupled-mode equation

CMT: coupled-mode theory

CPT: coupled-power theory

CPRI: common public radio interface

DCF: dispersion-compensating fiber

DGD: differential group delay

DPO: digital phosphor oscilloscope

DSF: dispersion-shifted fiber

DSP: digital signal processing

EDFA: erbium-doped fiber amplifier

EOM: electro-optic modulator

EVM: error vector magnitude

FBG: fiber Bragg gratings

FEM: finite element method

FIR: finite impulse response

FMF: few-mode fiber

FSR: free spectral range

FWHM: full width at half maximum

GI: graded-index

IL: insertion losses

LCFBG: linearly chirped fiber Bragg gratings

LPG: long-period gratings

MCC: mode-coupling coefficient

MCF: multicore fiber

MIMO: multiple-input and multiple-output

MMF: multimode fiber

MWP: microwave photonics

NR: new radio

OSA: optical spectrum analyzer

OTDR: optical time-domain reflectometer

PAA: phased array antenna

PCC: power coupling coefficient

PD: photodetector

PMD: polarization mode dispersion

PRRM: pulse repetition rate multiplication

QAM: quadrature amplitude modulation

QBER: quantum bit error rate

QKD: quantum key distribution

QPSK: quadrature phase shift keying

RF: radiofrequency

RoF: radio-over-fiber

SDM: space-division multiplexing

SEM: scanning electron microscope

SI: step-index

SNR: signal-to-noise ratio

SMF: single-mode fiber

SSA: signal and spectrum analyzer

TA: trench-assisted

TEC: temperature controlled chamber

TTDL: true-time delay line

UWB: ultra-wideband

VDL: variable delay line

VNA: vector network analyzer

VOA: variable optical attenuator

VSG: vector signal generator

WDM: wavelength-division multiplexing

WLS: white light source

Chapter 1
Introduction and Thesis objectives

1.1. Introduction

Space-Division Multiplexing (SDM) technology in optical fibers has been welcomed as a promising solution to the impending capacity shortage of traditional single-mode fiber (SMF) communications [1]–[3]. SDM seeks to increase the number of independent light channels transported within a single optical fiber to increase the transmission capacity within a fixed bandwidth. In addition, it aims to reduce energy consumption by integrating and sharing common optical components [2], [3]. In the past years, various SDM fiber alternatives, including multicore fibers (MCFs) and multimode fibers (MMFs), have been explored in the context of long-haul, high-capacity digital communications. Coupling among the different spatial channels determines the applicability of a particular SDM fiber to a given transmission scenario. In that regard, MCFs can be designed to show negligible channel coupling (i.e., uncoupled MCFs), and this eliminates the need for digital signal processing (DSP) after transmission [1], [3]. Because of that, uncoupled MCFs are regarded as the most prominent SDM technology and have been gaining interest in other research fields, including data-center interconnects [4], high-performance computing [5], quantum communications [6] and radio access networks for wireless communications [7].

Aside from being used as parallel distribution media, MCFs can be applied to a wide range of scenarios where they have the ability for signal distribution and processing. In particular, we expect that both optical signal processing and RF signal processing functionalities can benefit significantly from using MCFs in terms of compactness and weight, while assuring broadband versatility, reconfigurability, and performance stability. Either in the case of optical signal processing (such as chromatic dispersion compensation and temporal Talbot phenomena [8]) or Microwave Photonics (MWP) signal processing [9], the propagated signals must exhibit different group delay and/or chromatic dispersion characteristics. In the last case, the key lies in

implementing a tunable sampled true-time delay line (TTDL), an optical component that creates time-delayed samples or replicas of an input signal [10], [11]. This component is at the heart of most microwave photonics signal processors and enables many functionalities, including microwave signal filtering, antenna beam-steering for phased-array antennas, multi-gigabit-per-second analog-to-digital conversion, optoelectronic oscillation as well as arbitrary waveform generation and shaping [9], [12], [13]. These processing functionalities, in turn, are required in a variety of Information Technology applications, such as broadband wireless and satellite communications, distributed antenna systems and radar systems, among others.

The trend nowadays is to dedicate a given system (either a fiber-based device/system or a photonic integrated circuit) to process the signal and a separate optical fiber link to distribute the signal. Still, many applications require addressing both processing and distribution functionalities simultaneously since they need to implement the parallelization of the same processing task that is usually carried out by "brute-force" replication of the same processing device/system. Therefore, in this PhD Thesis, we propose the implementation of the required parallel signal processing functionalities while distributing the data signal to the end user by exploiting the inherent parallelism provided by multicore fibers. This implies the development of innovative heterogeneous multicore fibers where the different cores yield different propagation characteristics (in terms of group delay and chromatic dispersion) required for signal processing.

The concept of "fiber-distributed signal processing" shows great potential in the field of current and future converged fiber-wireless telecommunications networks, as those envisioned for future communications systems. Existing telecommunication networks are anticipated to face a tough challenge from emerging information and communication technology scenarios that significantly impact our society, such as 5G and Beyond wireless communications and the Internet of Things [14]–[17]. Demanding specifications are required in terms of cell coverage (from a few meters to several kilometers), connected device count (over 5 billion 5G connections globally [18]), supported applications and usage scenarios (such as 4K video streaming, autonomous driving, augmented reality, etc.), smooth and adaptive integration of the fiber and wireless segments, and energy efficiency [14]–[17], [19]. Fig. 1.1 depicts a typical fiber-wireless communications scenario where the use of MCFs brings an important reduction in space, weight and power consumption compared to using a bundle of single-core SMFs.

To sum up, the main goal is to exploit the inherent spatial parallelism of custom-designed heterogeneous multicore fibers to implement fiber-distributed signal processing operation by merging distribution and processing capabilities in a single optical fiber. Such a simultaneous operation can bring unique properties in terms of stability, compactness, power efficiency, flexibility and bandwidth in different fields of application where optical and RF signal processing is required.

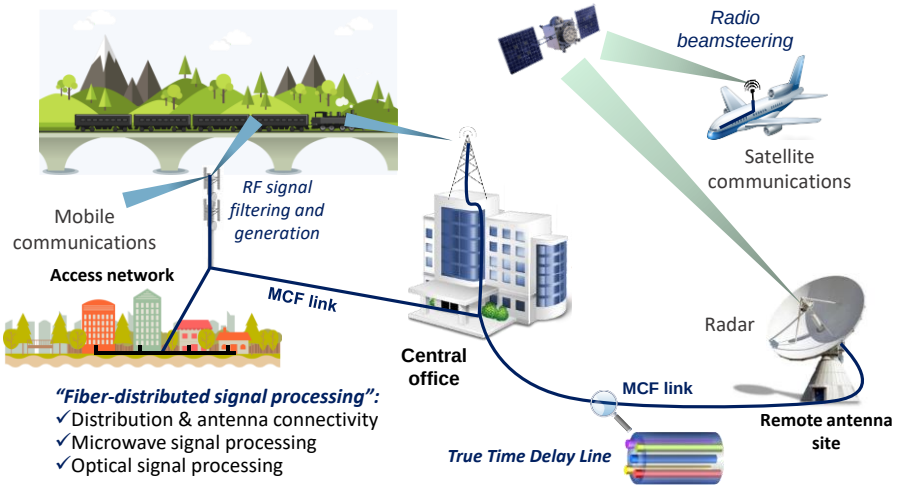

Fig. 1.1. Crucial fiber-wireless communication scenarios for the development of fiber-distributed signal processing using MCFs.

This PhD Thesis has been developed at the Photonics Research Labs (PRL), group within the ITEAM Research Institute at the Universitat Politècnica de València (UPV), Spain. This work has been carried out within the framework of the Spanish project *Multicore fibers for next-generation fiber-wireless applications* and the European project *Revolutionizing fibre-wireless communications through space-division multiplexed photonics* (InnoSpace) funded by the European Research Council (ERC).

1.2. Thesis objectives

The general objective of the Thesis is the validation, implementation and design of fiber-distributed signal processing solutions over heterogeneous multicore fibers for both optical and microwave signals. The Thesis is structured into 7 chapters, including this introductory one and a last one where we summarize the Thesis along with the main conclusions and propose potential future work. The specific Thesis objectives are:

1) The experimental characterization of a previously fabricated heterogeneous 7-core MCF-based TTDL regarding inter-core crosstalk, chromatic dispersion and differential group delay.

2) The experimental evaluation of the impact of external effects (bends, twist and temperature) over the signal processing performance.

3) The experimental demonstration of distributed radiofrequency signal processing including signal filtering, optical beamforming for phased array antennas and arbitrary waveform generation.

4) The experimental demonstration of low-crosstalk signal distribution over a heterogeneous MCF.

5) The design, fabrication and characterization of a high-core-count heterogeneous MCF-based TTDL.

6) Obtaining an ultra-low crosstalk MCF design for simultaneous quantum key distribution and classical channel transmission.

7) The proposal and design of an MCF with negative dispersion cores for dispersion compensation.

8) Designing a heterogeneous MCF for pulse repetition rate multiplication via parallel Talbot phenomena.

1.3. Outline of the Thesis

Starting with chapter 2, we review the state-of-the-art of multicore fibers for optical communications and their applications. In this chapter, we also introduce the research background on which this Thesis is based. As such, we present the field of Microwave Photonics and the concept of tunable optical TTDL, as well as its implementation with custom heterogeneous multicore fibers.

In chapter 3, we present the characterization of a heterogeneous 7-core MCF-based TTDL in terms of the basic optical propagation parameters (insertion losses, inter-core crosstalk, chromatic dispersion and differential group delay). Also, we delve into the detrimental effects that could impair the TTDL performance. This includes group delay variations induced by temperature fluctuations as wells as fiber bending and twisting. This serves as a validation stage of the TTDL performance of this fiber that will be essential for the following chapters.

Accordingly, chapter 4 deals with the implementation of several MWP signal processing functionalities that are built on the heterogeneous 7-core MCF-based TTDL. This includes reconfigurable RF signal filtering, tunable optical beamforming for phased-array antennas and arbitrary waveform generation. Additionally, we evaluate the performance of this fiber as a compact transmission medium for high-frequency 5G signals when exploiting all the cores.

In chapter 5, we present the design, fabrication and initial characterization of a novel heterogeneous 19-core MCF-based TTDL built using three different fiber preforms, each with a distinct refractive index profile. The fiber was fabricated at the Max Planck Institute for the Science of Light (MPL) in Erlangen, Germany. The three preforms were fabricated by the company Prysmian. After obtaining a preliminary fiber design, we focus on readapting it after characterizing the fabricated preforms. We also describe the fabrication process followed by the preliminary characterization of this multicore fiber.

Lastly, chapter 6 moves away from the topic of TTDL, as we propose three different heterogeneous MCF designs meant for quantum key distribution, dispersion compensation and parallel Talbot effects. In the first case, we propose an ultra-low crosstalk heterogeneous MCF design that allows the coexistence of classical and quantum signals in the same fiber. In the second case, we propose a dispersion compensation MCF, evaluating both and homogeneous and heterogeneous

alternatives. In the third case, we introduce the concept of parallel Talbot effects by designing a fiber with a specific chromatic dispersion in each core.

1.4. Original contributions

We would like to highlight several original research contributions presented in this Thesis:

- The experimental demonstration of tunable optical beamforming for phased array antennas on a heterogeneous 7-core MCF-based TTDL link (Chapter 4).
- The experimental demonstration of arbitrary waveform generation applied to ultra-wideband pulse generation built upon a heterogeneous 7-core MCF-based TTDL (Chapter 4).
- The design, evaluation and fabrication of a novel heterogeneous 19-core MCF where each core features the required group delay and chromatic dispersion behavior for tunable sampled TTDL operation (Chapter 5).
- The design of a novel heterogeneous MCF featuring ultra-low crosstalk, intended for the simultaneous transmission of quantum and classical channels in the same fiber (Chapter 6).
- The proposal of an original MCF design with negative dispersion cores, produced from the same fiber preform, intended for dispersion compensation (Chapter 6).
- The design of a unique heterogeneous MCF for parallel pulse repetition rate multiplication via the temporal Talbot effect (Chapter 6).

Chapter 2
State of the Art and research background

2.1. Multicore optical fibers

2.1.1. Introduction

Current high-capacity optical communication systems employ SMFs to transmit digital information. The maximum capacity of these fibers is considered to have reached its maximum capacity, with commercial systems being able to transmit between 70-100 Tb/s per fiber [2], [3]. In parallel, the demand for higher data rates has been experiencing a growth rate between 40% and 60%, doubling every 1.5 to 2 years, sustained by the popularity of services such as ultrahigh definition video streaming, cloud computing and the rise of machine-to-machine communications [2]. To increase the capacity of fiber-optic networks, operators are putting into service fiber that's already installed and upgrading the hardware in outdated systems. However, this is nothing more than a temporary measure that will not be able to alleviate the ever-increasing capacity demands for long. This situation could lead to a capacity crunch era in which the cost to increase capacity scales linearly (i.e., deployment of more fibers).

In view of that situation, SDM is regarded as the most promising approach to deal with that capacity crunch [1]–[3]. In the best case, SDM aims to increase the transmission capacity over a fixed bandwidth by increasing the number of light paths that are transmitted within a single optical fiber. And, at the same time, reduce the cost per bit and the energy consumption. Different SDM technologies have been proposed including high-density fiber bundles, MMFs and MCFs. Fiber bundles are a simple solution to obtain multiple independent spatial channels. However, the spatial density is low compared to in-fiber solutions, which can also benefit from component sharing in the whole fiber link (e.g., common light sources, amplifiers or shared DSP hardware) [2], [3]. A deeper integration can be achieved with SDM

fibers, which is expected to increase the energy efficiency and reduce the cost-per-bit.

Among SDM fibers, one alternative is to employ the orthogonal modes of a MMF as individual spatial channels. High spatial density is obtained in that case, but multi-input multiple-output (MIMO) processing is generally required to undo the coupling between modes. In that regard, fibers with less guided modes, i.e., few-mode fibers (FMFs) were introduced to reduce processing requirements. Although they considerably reduce the mode coupling, MIMO-less transmission distance is still limited up to a few hundreds of meters. Another alternative are MCFs, which consist of several individual cores arranged within the same fiber cladding. The need for MIMO signal processing depends on the degree of coupling between fiber cores, and that relates to the spatial channel density. When coupling is low enough, each core can be considered as an independent spatial channel. In contrast to FMFs, negligible coupling between the different spatial channels can be obtained with MCFs even at moderate propagation distances (5-50 km). Therefore, we focus on MCFs in this thesis as they enable the immediate implementation of fiber-distributed signal processing.

We can classify MCFs based on different fiber design parameters, to list the most important ones:

- Core separation or core pitch (Λ), determines the degree of coupling between cores and, consequently, the core count.
- Spatial homogeneity, depending on whether all cores are identical (homogeneous MCF) or not (heterogeneous MCF).
- Core modal regime, single-mode or few-mode. If all cores have the same regime, MCFs can be grouped as single-mode MCF or few-mode MCFs.
- Core refractive index profile, step-index (SI) cores are generally used in single-mode designs, while in few-mode fibers a graded-index (GI) profile is more common. When a trench layer is added around the core, it is referred to as a trench-assisted (TA-) core.
- Core arrangement or core layout, which depends on the number of cores to distribute and the use case application. Cores can be distributed in a linear array, square lattice, hexagonal lattice (also known as hexagonal closed-packed structure), ring, etc.

Figure 2.1 represents the different types of MCF attending to the core pitch. MCFs can be grouped into weakly-coupled or uncoupled, in which each core can be considered as an independent fiber and inter-core crosstalk is undesirable; and coupled-core where strong coupling between cores is intended [1], [3]. While coupled-core MCFs can host more cores for the same area than weakly-coupled MCFs, MIMO DSP after coherent detection is required to revert coupling along the propagation distance. On the other hand, weakly-coupled MCFs can be easily integrated into current networks because don't require complex transceiver technologies and have good compatibility with existing SMF-based systems.

Coupled-core can be further divided into randomly-coupled MCF and strongly-coupled MCF (also known as systematic coupling MCF). Each subtype has specific propagation characteristics (differential group delay, mode-dependent loss, etc.), which are related to the coupling strength [20]. While in a strongly-coupled MCF the propagation in spatial modes (or supermodes) leads to large differential group delay (DGD), in randomly-coupled MCF the random coupling between them reduces the delay spread which in turn diminishes DSP complexity.

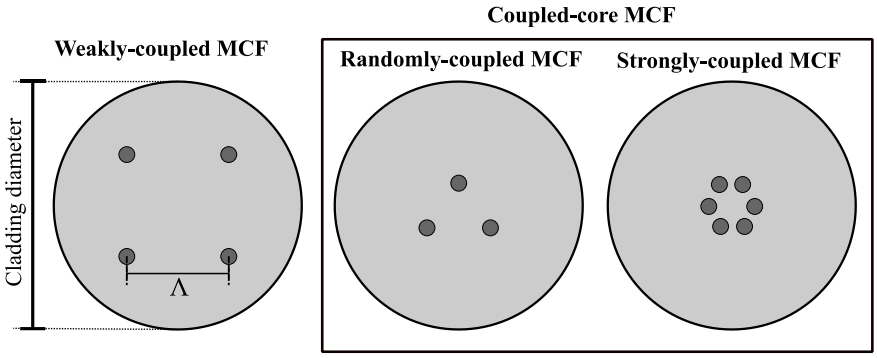

Fig. 2.1. Types of MCF classified by their coupling regime.

2.1.2. Weakly-coupled multicore fibers

Focusing on weakly-coupled MCFs, Fig. 2.2 displays some MCFs examples based on core homogeneity and modal regime. First, homogeneous MCF can be implemented by packing together cores with the same propagation characteristics. These fibers are easy to fabricate, especially when considering step-index cores, but suffer from higher crosstalk which limits the core density and transmission distance. Several strategies have been proposed to lower inter-core crosstalk. A straightforward approach is to design the core refractive index profile with a high core-to-cladding index and a small radius to increase mode confinement [21]. Another approach is increasing the core pitch, but that reduces core density and increases the thickness of the fiber. Moreover, embracing a more complex profile, such as trench-assisted [22] or hole-assisted cores [23], is proven to have a great impact on crosstalk. Thanks to this, fibers can be designed with a lower pitch resulting in higher spatial density. For instance, a 260-μm cladding diameter single-mode MCF was presented in 2015 [24] with 22 trench-assisted cores placed in a two-pitch layout with average pitches of 41 and 48 μm.

A different strategy is the use of cores with distinct refractive index profile. A fiber like this is commonly known as a heterogeneous MCF and was proposed in 2009 by Koshiba et al. [25]. In the case of fibers for high-capacity communications, three or four types of cores have been demonstrated [26], [27], which are usually arranged in a triangular lattice so that cores of the same type do not neighbor themselves. Inter-core crosstalk is substantially reduced because the phase-matching condition is prevented. Exceptionally, a 19-core MCF with 125-μm cladding diameter and nine types of cores distributed with a 23-um pitch was proposed in [28]. Later, a combination of both heterogeneous and trench-assisted strategies led to the

fabrication of a 37-core single-mode MCF, which features a 248-µm cladding diameter and three kinds of trench-assisted cores [29]. Moreover, the inclusion of few-mode cores increases the number of spatial channels further. A MCF containing 38 cores with 3 modes per core (114 spatial channels) was fabricated with a cladding diameter of 312 µm and a core pitch of 40 µm [30]. This fiber is, up to date, the one with the highest spatial channel density per cladding diameter.

Most of the previously cited MCFs possess a cladding diameter larger than the standard for SMFs (125 µm). Increasing the cladding diameter is related to a worse mechanical reliability as compared to SMFs [31], [32]. Matsuo et al. [32] investigated the failure probability dependence with the cladding diameter. A larger cladding diameter is related to an increased failure probability (compared to a 125-µm cladding diameter) of the deployed fibers and an increase of splicing losses as well (as cores are more separated from the center of the fiber). Fiber production is considered another issue with the current fabrication methods. For instance, to fabricate 1000 km of a 250-µm cladding diameter MCF the preform needs to be 4 m long with a 120-mm radius [31]. For these reasons, several MCF designs with a cladding diameter of 125 µm have been developed. For instance, Matsui et al. present several designs that have optical compatibility with G.652, G.657 and G.654 ITU-T standards, [31], [33]. And each design corresponds to a different use case application; namely, access networks, terrestrial long-haul and submarine long-haul, respectively. A heterogeneous design has also been demonstrated with four cores placed around a central one aimed for interconnecting with SMFs [34].

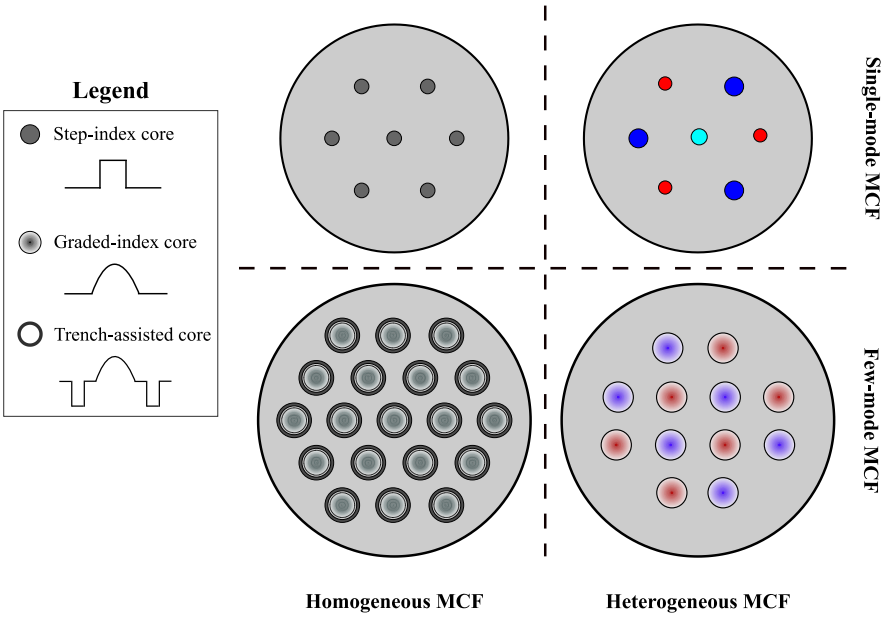

Fig. 2.2. Weakly-coupled MCF classification by core homogeneity and modal regime. Different colors indicate a different type of core.

2.1.3. Inter-core crosstalk modeling

Inter-core crosstalk is produced by the expansion of the optical fields propagating in one of the cores to the rest of them. Small crosstalk contributions produced at multiple points during signal propagation throughout the fiber accumulate with an arbitrary time delay and a random polarization, thus acting as noise [35], [36]. This random noise can break the integrity of the signals being transported. Therefore, a low inter-core crosstalk ensures each core can be considered as an independent channel. As we saw in the previous section, several strategies have been developed to deal with coupling in weakly-coupled MCFs. Accompanying the development of MCFs, a significant effort has been made to model it.

The coupled-mode theory (CMT) deals with the interaction of the optical fields in different modes (or cores) during propagation [37]. A set of coupled first-order equations, i.e., the coupled-mode equations (CME), predict the evolution of the amplitude of the different modes along the propagation direction (z). The CME for an unperturbed waveguide with two modes (or cores) with amplitudes A_n and A_m is

$$\frac{dA_m(z)}{dz} = -j\sum_{n\neq m}\kappa_{mn}A_n(z)e^{-j(\beta_m-\beta_n)z}\,, \tag{2.1}$$

where κ_{nm} is the mode-coupling coefficient (MCC) between the modes, and β_n and β_m the propagation constants of cores n and m. Formally, the MCC can be expressed as in [38]:

$$\kappa_{mn} = \frac{\omega\varepsilon_0\iint(n^2-n_n^2)\mathbf{E}_m^*\cdot\mathbf{E}_n dxdy}{\iint\hat{z}(\mathbf{E}_m^*\cdot\mathbf{H}_m+\mathbf{E}_m\cdot\mathbf{H}_m^*)dxdy}, \tag{2.2}$$

being ω the angular frequency, ε_0 the electric permeability in vacuum, n the refractive index distribution of the whole coupled region, n_m the refractive index distribution of the unperturbed waveguide m, $\mathbf{E}$ and $\mathbf{H}$ the normalized vector fields of the electric and magnetic fields of each mode, and * indicates the complex conjugate. Here we note that under certain conditions the MCC between a couple of SI or trench-assisted SI (TA-SI) cores can be calculated analytically, as shown in Table AI.1 which gathers a list of analytical expressions to calculate the MCC for homogeneous and heterogeneous cores. However, when the refractive index profile of the core is different than a SI, for instance a graded-index (GI) profile, the calculation of the MCC must be performed numerically (as explained in section AI.2 of Annex AI).

The CMT can be utilized to model the propagation through the different cores of an MCF, but in its classical form it considers an ideally unperturbed waveguide. This is not the case in optical fibers as fiber bending and twisting alter the refractive index profile [39]. The conformal mapping model [40] was introduced to account for the bending-induced refractive index change on the fiber. Using that model, we can express the equivalent propagation constant ($\beta_{eq,n}$) of a bent MCF core n as:

$$\beta_{eq,n} = \beta_n\left(1+\frac{r_n}{R_b}\cos\theta_n\right), \tag{2.3}$$

being R_b the bending radius and (r_n, θ_n) the local polar coordinates of core n.

Variation along the propagation coordinate is introduced by solving the CMT numerically. The propagation length is divided into small steps and a phase offset is applied to Eq. (2.1), so that the change on the propagation constant because of bending and twisting is considered [41]. However, a model like that reflects only the deterministic evolution of the fiber structure [42]. To solve that, a random phase contribution is introduced to model the structural variations [41]–[43]. The accuracy of these models depends on the step size and the statistical parameters chosen in each case. A high number of simulations needs to be carried out in order to represent accurately inter-core crosstalk [39], [42].

Further work has focused on finding another approach for inter-core crosstalk estimation. A simpler description of the power in the cores is obtained with the coupled-power theory (CPT). Analogously to the previous case, a set of coupled first-order equations are derived for a couple of cores with average power P_m and P_n [41]:

$$\frac{dP_m(z)}{dz} = \sum_{n \neq m} h_{mn}(z)\left[P_n(z) - P_m(z)\right], \tag{2.4}$$

where h_{mn} is the z-dependent power coupling coefficient (PCC). In turn, the PCC can be described by an autocorrelation function that takes into account the variation-induced bending and twisting, as well as the random structural variations. In [41], they propose three different autocorrelation functions with exponential, gaussian and triangular distributions, respectively.

If we consider the multicore fiber is bent at a constant bending radius R_b while being twisted at a constant rate γ, then the average of the longitudinal varying local PCC is expressed as:

$$\bar{h}_{mn} = \frac{\gamma}{2\pi} \int_0^{2\pi/\gamma} h_{mn}(z)dz. \tag{2.5}$$

From Eq. (2.4), Koshiba et al. [44] developed a closed-form expression for the average PCC $\bar{h}_{mn}$ assuming an exponential autocorrelation function. The analytical expression of the average PCC is written as

$$\bar{h}_{mn} = \sqrt{2}\mathrm{K}_{mn}^2 d \left| \frac{1}{\sqrt{a\left(b+\sqrt{ac}\right)}} + \frac{1}{\sqrt{c\left(b+\sqrt{ac}\right)}} \right|, \tag{2.6}$$

where K_{mn} is the redefined MCC [44], d is the correlation length, and the rest of parameters are defined by

$$
\begin{aligned}
a &= 1+\left(\Delta\beta_{mn}d-\frac{B_{mn}d}{R_b}\right)^2,\\
b &= 1+\left(\Delta\beta_{mn}d\right)^2-\left(\frac{B_{mn}d}{R_b}\right)^2,\\
c &= 1+\left(\Delta\beta_{mn}d+\frac{B_{mn}d}{R_b}\right)^2,\\
B_{mn} &= \sqrt{\left(\beta_m x_m-\beta_n x_n\right)^2+\left(\beta_m y_m-\beta_n y_n\right)^2},
\end{aligned}
\tag{2.7}
$$

being $\Delta\beta_{mn} = \beta_m - \beta_n$ and (x_m, y_m) the coordinates of the center of core m at $z = 0$. The analytical expression in Eq. (2.7) accounts for a generic MCF, either with homogeneous or heterogeneous cores, including the case of trench-assisted structures as well. From, this coefficient, one can easily derive the crosstalk between cores m and n for a fiber link of length L as:

$$XT = \tanh\left(\bar{h}_{mn}L\right), \tag{2.8}$$

which can be approximated as $XT \approx \bar{h}_{mn}L$ for low values of $\bar{h}_{mn}$.

Here, we note that the inter-core crosstalk has a different behavior depending on the core homogeneity of the MCF. In homogeneous MCFs, fiber bending benefits crosstalk as it induces a change on the propagation constant β that depends on the position of the core. Hence, crosstalk tends to increase with the bending radii in homogeneous MCFs, as shown in Fig. 2.3(a). On the other hand, heterogeneous MCFs are designed to have a $\Delta\beta \neq 0$. Because of that, phase matching between a given pair of cores ($\Delta\beta = 0$) can arise when the fiber is curved with a particular bending radius, the critical bending radius (R_{pk}). We see this in Fig. 2.3(b), when $R_b <= R_{pk}$ crosstalk depends proportionally on R_b, whilst when $R_b > R_{pk}$ it depends on the correlation length d.

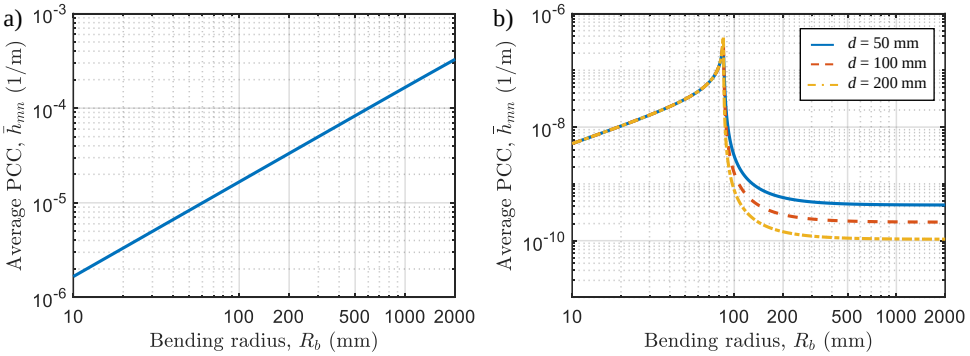

Fig. 2.3. Average PCC for a couple of (a) homogeneous and (b) heterogeneous cores. A correlation length d = 50 mm is used in the homogeneous case.

The critical bending radius R_{pk} can be calculated from B_{mn} in Eq. (2.7) as [44], [45]:

$$R_{pk} = \frac{B_{mn}}{\left|\Delta\beta_{mn}\right|} \approx \Lambda \frac{n_{eff,m}}{\left|\Delta n_{eff,nm}\right|}, \tag{2.9}$$

being $\Delta n_{eff,nm} = n_{\mathrm{eff,m}} - n_{\mathrm{eff,n}}$, the effective index difference between cores.

2.1.4. Applications of MCFs in optical communications

2.1.4.1. High-capacity digital data transmission

Numerous digital data transmission experiments have been demonstrated in which entire optical communication systems are basically replicated in the different spatial paths. The number of spatial paths, the total data rate and the spatial-spectral efficiency (SSE) are used to categorize these systems. The spatial-spectral efficiency is the spectral efficiency divided by the cladding area with respect to the SMF cladding area. These demonstrations can be categorized depending on whether the signal is recirculated (multi-span experiments), or a single fiber span is employed (single span or short-reach experiments) and the type of fiber used [3].

Centering on short-reach experiments, a total data rate of 2.15 Pb/s was obtained with a 22-core single-mode MCF for a 31-km link [24]. A wideband optical comb was employed in this experiment to generate 402 spatial super channels resulting in an SSE of 49.69 b/s/Hz/A_{SMF}. In the case of few-mode MCFs, a rate of 10.66 Pb/s (the largest rate to date) was attained with a 13-km long 38-core MCF in which each core guided three modes [46]. Similarly, a total rate of 10.16 Pb/s was achieved by means of a 11.3-km long 19-core MCF with 6 modes per core [47]. These two experiments featured the same 114 spatial channels and a comparable data rate. The cladding diameter in each case was 312 and 267 μm, respectively, which in turn bring in an SSE of 185.99 and 240.74 b/s/Hz/A_{SMF}. Compared to the single-mode case, few-mode MCFs increase greatly the data rate efficiency.

In multi-span (long) distance experiments, the transmitted signals in each core need to be amplified. The longest transmission experiment was performed with a 12-core single-mode MCF over 14,350 km [48] but individual Erbium-doped fiber amplifiers (EDFAs) were employed. Cladding-pumped multicore EDFAs are generally used with higher-core-count MCFs [49], [50], while core-pumped multicore EDFAs are limited to 7-core MCFs [51]. Furthermore, when considering more than one mode per core, the 38-core 3-mode few-mode MCF was used again in [52] to reach 6.2 Pb/s in 65 km. Mode-dependent loss was pointed out as the limitation to reach a longer link length.

These experiments showed that data rates can be greatly improved with the use of weakly-coupled MCFs. However, the fibers employed have a cladding diameter larger than the standard one for SMFs (125 μm). This could affect the competitiveness of these fibers with SMF arrays as well as their mechanical reliability [3], [31]. To solve that, researchers at NICT have demonstrated data rates per core of the same order of magnitude than the maximum achievable rate in SMFs (100 Tb/s-200 Tb/s) [53] or even higher [54]. Of course, here we need to take into account that

other aspects also determine the total data rate of a fiber link, such as the optical bandwidth and the modulation format. Nonetheless, these achievements pave the way for future high-capacity fiber deployments built entirely upon MCFs.

2.1.4.2. Quantum Key Distribution (QKD)

Quantum key distribution (QKD) provides a secure way to distribute secret keys between remote parties [55]–[57]. Since QKD is based on quantum mechanics principles, resistance against eavesdroppers is granted as the secrecy of the distributed keys can be verified. Early QKD experiments focused upon the feasibility of the technology, starting from proof-of-principle laboratory experiments. The secure bit rate has been increased by three orders of magnitude to 1 Mb/s over 50-km fiber thanks to the development of efficient QKD protocols [58] and high-speed single-photon detectors [59]. Telecommunication networks were the next target of QKD systems. Initially, backbone and metropolitan QKD network demonstrators were built to enable multi-user connectivity [60]–[62]. Then, these systems focused on the integration of QKD systems into access networks. Here, a point-to-multiple-point (P2MP) architecture is more suitable to allow simultaneous access by multiple users rather than resorting to P2P QKD links. For instance, in [63] the authors demonstrated a quantum access network of this type by sharing the most expensive element, the high-speed detector, for up to 64 users.

As in classical networks, the full capacity of QKD can be unleashed by incorporating the SDM domain on top of the existing wavelength-division multiplexing (WDM) layer. MCFs are especially attractive as they can be designed to render a negligible inter-core crosstalk. Hence, they can be employed as a transmission media to increase the capacity of QKD systems, either by allowing the parallel transmission of independent keys between different final users sharing the same transmission medium (a feature desired in access networks) or by multiplying the capacity of key transmission by suitable disassembly, transmission and final assembly of a high-speed quantum key between two end users.

Several groups have reported experimental work connected to the use of MCFs for QKD transmission. For instance, in [64], researchers demonstrated the successful transmission of QKD signals coexisting with classical data signals launched at full power in a 53-km 7-core fiber, while showing negligible degradation in performance. The QKD signal was transmitted at a different core than the classical channels and in a different wavelength to reduce the impact of intercore crosstalk. Similarly, the transmission of 11.2-Tb/s channels was demonstrated in another 7-core fiber along 50 km [65]. Further, the excess noise produced by 30 WDM channels at the neighboring cores of the quantum core was characterized on a homogeneous 19-core MCF [66]. Quantum channel transmission in the guard band between WDM channels is shown to be feasible. Additionally, counter-propagation and wavelength interleaving between classical and quantum channels was proven to reduce crosstalk impairment [67]. Lastly, classical-quantum channels coexistence in the same core was demonstrated in a heterogeneous 37-core MCF [68]. This is the largest number of cores used in a demonstration until now, and the record secure key rate transmission (105.5 Mbps).

2.1.4.3. Optical distribution networks for 5G and Beyond

Another scenario in which MCFs could excel is optical distribution networks for mobile networks. Optical distribution networks are nowadays comprised of SMF bundles, with schemes based on passive optical networks and WDM [7]. The fifth generation of mobile networks (5G) established certain requirements on data rate, latency and user density. 5G is expected to provide up to 1000x increase in capacity, a latency less than 1 ms and up to 100x multiplication in the number of connected devices compared to 4G [15], [16], [19]. The development of 5G New Radio (NR) is expected to cover all these requirements, especially with the introduction of millimeter-wave bands (mmWave). But it poses a challenge to optical distribution networks as the leading fronthaul technology, common public radio interface (CPRI), scales poorly with high frequency and MIMO antenna deployments. The use of mm-wave signals also increases the bandwidth requirements for CPRI, which are said to scale from Gb/s to Tb/s in complex deployments. The analog fronthaul alternative proposed by Rommel et al. [69]] is based on the use of MCFs for signal distribution. In that work, a homogeneous 7-core MCF was employed to transmit a 25.5-GHz 5G new radio signal in downlink and uplink configurations using different cores in each case. In a similar way, Morant et al. [70], [71] employed a 4-core MCF for the transmission of MIMO signals. In both works, optical beamforming is performed externally with a different optical device (i.e., a photonic integrated chip).

Additionally, Vazquez et al. studied the possibility of achieving power-over-fiber in multicore fibers for radio-over-fiber (RoF) systems [72]. Some cores are devoted to power delivery while others can be used for RF signal distribution. In fact, power-over-fiber was demonstrated in a 10-km long 7-core MCF applied to a 5G fronthaul situation [73]. A maximum optical power of 133 mW could be transmitted with negligible BER impact. Moreover, WDM transmission in the central core of a 7-core MCF with a 60-W co-propagating signal in the outer cores was demonstrated in [74].

2.2. Thesis research background

2.2.1. Introduction to Microwave Photonics

Microwave photonics is an interdisciplinary field that combines microwave and photonic engineering. MWP aims to fulfill the tasks of generating, transmitting, and processing microwave signals in the optical domain. These “tasks” are implemented nowadays by traditional electronic systems that suffer from frequency-dependent loss and narrow bandwidth operation [12], [13], [75]. In contrast, optical systems bring the advantages of high bandwidth, immunity to electromagnetic interference and low loss (independent with the radiofrequency). In addition, they present the advantage of fast tunability and reconfigurability, attributes that are difficult to obtain in electronic systems [9]. MWP has the potential to solve the capacity bottleneck in current electronic systems, especially in the mm-wave bands.

Figure 2.4 represents the typical MWP link consisting of a light source (typically a tunable laser or an incoherent source), an electro-optic modulator (EOM) which converts the RF input signal to the optical domain, the optical system itself and the

receiver that converts the signal back to the electrical domain. The optical system is implemented typically by an optical fiber or an integrated photonic circuit [9]. Depending on the application, other optical components are present on the link such as optical filters, amplifiers or delay lines. The characteristics of the output signal depend on the response of the optical system, which in turn depends on the elements present in the link and how the RF signal is up-converted.

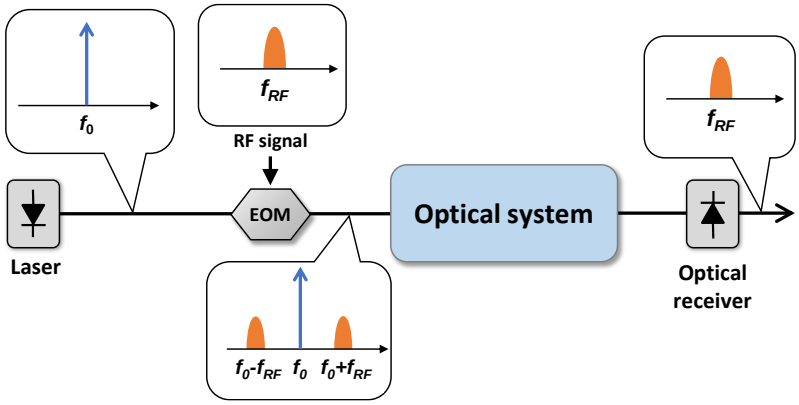

Fig. 2.4. Simplified scheme of an analog microwave photonics link.

A prominent topic of interest that takes advantage on the low loss and broadband operation of MWP are RoF systems. The distribution of radio signals via optic fibers is used nowadays in a multitude of wireless networks, including in-door distributed antenna systems and outdoor cellular networks. Due to the proliferation of connected, high-capacity smart devices and the expansion of broadband multi-media services available to consumers, there is an unheard-of demand for wireless access to high-speed data communications. It is necessary then to develop integrated optical/wireless networks that can reliably and affordably meet present and future capacity requirements, traffic growth rates, new service requirements, and numerous wireless standards [76]. The biggest attraction of RoF systems is that they provide flexible multiple antenna distant connectivity with less sophisticated systems. This happens as a result of consolidating the majority of transceiver functionalities in the central office, sending wireless signals over fiber in their modulated format, and integrating a streamlined antenna module closer to the consumer.

Another essential application field of MWP is signal processing. In addition to the inherent benefits of photonics, processing RF signals in the optical domain offers previously unheard-of benefits over conventional electronic technologies, including the ability to: (1) handle high-speed RF signals by overcoming the sample speed limitation of electronic signal processors; (2) provide adaptive and reconfigurable operation; and (3) enable integration into existing fiber-optic systems (since the signals to be processed are already in the optical domain) [9], [77], [78]. Many functionalities have been developed to deal with RF signals in the microwave and the emerging millimeter-wave bands, including signal filtering, beamforming networks for phased arrays antennas, analog-to-digital conversion, frequency up/down

conversion, instantaneous RF measurement, optoelectronic oscillation, as well as arbitrary waveform generation and shaping [9], [77], [78].

Even with all the benefits that MWP can bring to overcome capacity bottleneck in communications, mass adoption is limited by the bulky, heavy and power-consuming nature of its systems [79]. One of the major challenges that MWP must overcome nowadays is related to the reduction of size, weight and power consumption while assuring broadband seamless reconfigurability and stability. In this sense, integration is key to achieve these goals. On one hand, photonic integrated circuits can perform a large variety of signal processing functionalities with a footprint similar to the size of electronic circuits [80]. This can be referred as "vertical integration" [10], as components and subsystems are integrated in monolithic photonic circuits. On the other hand, "horizontal integration" can be achieved with SDM fiber-distributed technologies. The multitude of spatial paths found in SDM fibers can be exploited to distribute multiple signals as in classical systems or to implement fiber-distributed signal processing. A key building block to these functionalities is the TTDL.

2.2.2. True-time delay line (TTDL)

A TTDL produces a set of time-delayed samples of an input signal that are defined by a constant differential delay ($\Delta\tau$) between them. In general, we can find in the literature two different approaches to induce a given time delay between samples. First, exploiting the group velocity variation with the optical wavelength, i.e., the wavelength dimension, as it is done in fiber grating inscription [81] or photonic crystal fibers [82]. Second, the use of optical fibers or waveguides with a different length, i.e., exploiting the space dimension, such as switched configurations in fiber-based [83] or integrated platforms [84]. Additionally, another approach can be realized which merges together the previous ones. We can resort to both the space and the wavelength dimensions without requiring different lengths or complex configurations by properly controlling the group index behavior on different optical waveguides. To achieve that, we propose the exploitation of the inherent parallelism of SDM fibers to behave as tunable sampled TTDLs.

Until now, a few approaches of TTDLs based on SDM fibers have been proposed. First, sampled TTDLs based on commercial fibers: (1) a homogeneous MCF with selectively inscribed fiber Bragg gratings (FBGs) [85] and (2) 4-LP-mode step-index FMF with long-period gratings (LPGs) inscribed [86]. However, those approaches do not provide continuous time delay tunability. To obtain that, SDM fibers are customized to provide the required performance in each core or mode, i.e., to provide the appropriate value of chromatic dispersion. In that regard, we have developed: (1) a 19-core photonic crystal fiber where each silica core is surrounded by a different configuration of air holes [87]; (2) a 7-LP-mode ring-core FMF with LPGs inscribed for 4-sample operation [88]; (3) a 5-mode-group double-clad FMF [89] and (4) a dispersion-diversity heterogeneous MCF with seven trench-assisted cores drawn from seven different preforms [90]. The last two TTDL SDM-fiber designs have been demonstrated experimentally. Regarding the fiber (5), in Chapter 3 we will present a complete optical characterization, while in Chapter 4 we will apply it to perform several signal processing experimental demonstrations.

To realize a tunable TTDL in MCFs, each core must feature different propagation characteristics (in terms of group delay and chromatic dispersion) [10], [11]. Fig. 2.5 depicts how sampled TTDLs operate when either the space diversity or the wavelength diversity is employed. In the space diversity domain, a single carrier (λ_m) is modulated and coupled into each core of the MCF. At the MCF output, N samples of the RF signal are obtained with a constant group delay difference. Tunability of this delay difference with the optical wavelength requires incremental group delay slopes between adjacent samples, in other words, incremental values of the chromatic dispersion. This way, we can change the differential group delay between adjacent samples by tuning the operation wavelength of the optical source. In contrast, in the wavelength diversity domain we utilize M different carriers ($\lambda_{1...}\ \lambda_M$) to obtain a set of M different samples at the output of a given core n. The separation between samples determines the delay difference between samples. All together, we can obtain 2-D operation when both the space and wavelength diversities are exploited.

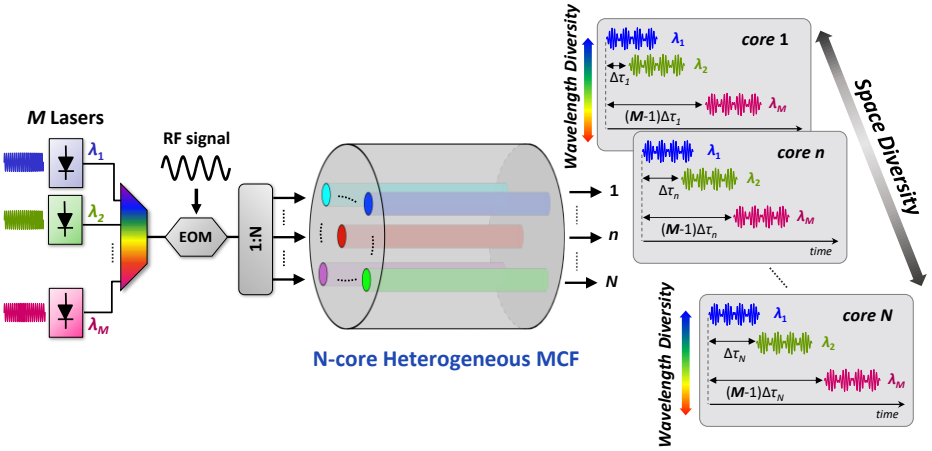

Fig. 2.5. Principle of operation of a tunable sampled TTDL built upon an N-core heterogeneous MCF.

2.2.3. TTDL implementation with heterogeneous MCFs

A group-index variable delay line implies a variation in the propagation velocity of the optical spatial paths involved [11]. The design of a heterogeneous MCF to behave as a group-index-variable delay line requires that each core features an independent group delay with a linear dependence on the optical wavelength λ, as depicted in Fig. 2.6(a). To study this, we can expand the group delay of a given core n per unit length, $\tau_n(\lambda)$, as a 2nd-order Taylor series around an anchor wavelength λ_0:

$$\tau_n(\lambda) = \tau_0 + D_n(\lambda - \lambda_0) + \frac{1}{2} S_n(\lambda - \lambda_0)^2, \tag{2.10}$$

where D_n is the chromatic dispersion and S_n the dispersion slope of core n, both at the anchor wavelength λ_0. From Eq. (2.10), we perceive that for proper TTDL operation: (1) all cores share a common group delay τ_0 at the anchor wavelength λ_0; (2) the chromatic dispersion D_n needs to increase with the core number on an incremental

basis; and (3) the effect of the dispersion slope S_n must be minimized as it introduces a quadratic term on the group delay. The basic differential delay, in other words, the delay difference between adjacent samples, is obtained differently in each diversity domain. As a consequence, we address each diversity domain individually.

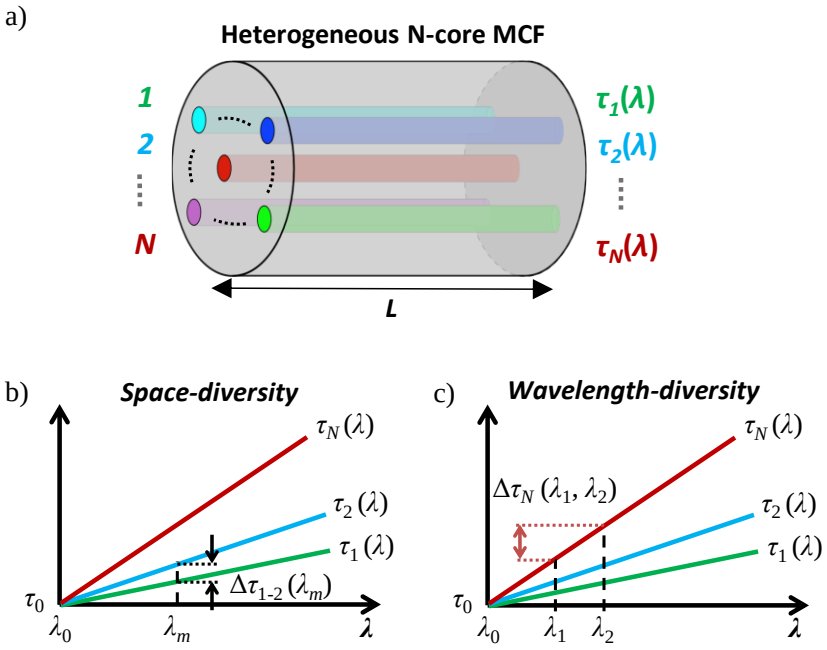

Fig. 2.6. (a) An *N*-core heterogeneous MCF-based TTDL. The spectral group delay of the *N* cores when the space-diversity (b) or the wavelength-diversity (c) domains are exploited.

In the spatial diversity domain (shown in Fig. 2.6(b)), the basic differential delay $\Delta\tau_{n,n+1}$ is given by the propagation difference created between a pair of adjacent cores for a particular wavelength λ_m. From Eq. (2.10):

$$\Delta\tau_{n,n+1}(\lambda_m) = \Delta D(\lambda_m - \lambda_0) + \frac{\Delta S}{2}(\lambda_m - \lambda_0)^2, \tag{2.11}$$

where $\Delta D = D_{n+1} - D_n$ is the incremental dispersion, which must be constant for every pair of adjacent cores, and $\Delta S = S_{n+1} - S_n$ is the dispersion slope variability between those same cores. The linear dependence of the basic differential delay with the optical wavelength requires the minimization of ΔS. We can define the differential group delay relative error induced by this effect as the ratio between the second and the first terms of the right-hand side of Eq. (2.11), that is:

$$\Delta\tau_{n,n+1}(\lambda_m)\Big|_{rel\_err} = \frac{\Delta S}{2\Delta D}(\lambda_m - \lambda_0), \tag{2.12}$$

which shows that the detrimental nonlinear effect raised by ΔS increases with the operation wavelength.

When the delay line operates in the optical wavelength diversity domain (shown in Fig. 2.6(c)), the differential group delay experienced between two contiguous wavelengths (λ_m, λ_{m+1}) in a particular core *n* is given by:

$$\Delta\tau_n\left(\lambda_m,\lambda_{m+1}\right)=D_n\delta\lambda+S_n\left(\lambda_1-\lambda_0\right)\delta\lambda+\frac{1}{2}S_n\left(2m-1\right)\delta\lambda^2, \tag{2.13}$$

where $\delta\lambda = \lambda_{m+1} - \lambda_m$ is the separation between the two adjacent optical sources, λ_1 the wavelength of the first optical source and $1 \leq m \leq M - 1$, being M the total number of optical sources. In this case, the variation introduced by the higher-order dispersion is characterized by both a linear ($\delta\lambda$) and quadratic ($\delta\lambda^2$) dependence. The quadratic dependence can be avoided by setting slightly different wavelength separations between optical sources (i.e., making $\delta\lambda$ a λ-dependent function) as to obtain a constant basic differential delay.
Now, the differential group delay relative error is defined as:

$$\Delta\tau_n\left(\lambda_m,\lambda_{m+1}\right)\Big|_{rel\_err}=\frac{S_n\left[\left(\lambda_1-\lambda_0\right)+\frac{1}{2}\left(2m-1\right)\delta\lambda\right]}{D_n}. \tag{2.14}$$

As Eq. (2.14) shows, when we exploit the wavelength diversity, the differential group delay relative error depends on the values of both S_n and D_n of the particular core used. On the other hand, when we use the spatial diversity instead, this error depends on the variabilities between cores ΔS and ΔD, as shown in Eq. (2.12).

Chapter 3

Heterogeneous 7-core MCF-based TTDL: Characterization

3.1. Introduction

As previously explored, a TTDL can be implemented in a heterogeneous MCF by independently tailoring each core's propagation characteristics. Following this concept, the first MCF-based TTDL was designed and fabricated in 2019 [91]. It has seven cores and features a tunable differential group delay between cores of up to 150 ps in a 30-nm range. A first characterization of this fiber was carried out in that work (also presented in [90]), where preliminary insertion losses, inter-core crosstalk, chromatic dispersion and DGD were measured. However, some aspects of these properties that could influence TTDL performance still need to be fully characterized.

First, we characterize the dependence of the insertion losses and inter-core crosstalk with the optical wavelength. As TTDL tunability is based on modifying the optical wavelength of operation in a particular range, a high variation of either the insertion losses or inter-core crosstalk could alter the application being implemented. Similarly, inter-core crosstalk temporal fluctuations could distort the response of the final application. Then, moving to the actual TTDL performance of this fiber, we characterize it in detail by measuring the differential group delay between cores and its stability, and the chromatic dispersion of the whole fiber link using the carrier suppression effect (CSE) at different optical wavelengths. Lastly, we evaluate experimentally some detrimental effects that can affect the TTDL performance, such as temperature changes and fiber bending and twisting. This last effect is investigated on a commercial 7-core homogeneous fiber for practical reasons.

3.2. Previous work: design and fabrication

The fabricated heterogeneous MCF was designed with seven distinct trench-assisted step-index cores placed in a hexagonal grid with one core in the center. Fig. 3.1 represents the core distribution in the fiber (a) and the refractive index profile of the cores (b). The core pitch (Λ) is 40 µm and the cladding diameter is 150 µm. The core structure consists of a GeO_2-doped core layer (core radius a_1 and core-to-cladding relative index difference Δ_1) surrounded by a pure silica inner cladding (core-to-trench distance a_2) and a 1%-Fluorine-doped trench (width w). The refractive index profile of each core was tailored independently by varying the core design parameters (a_1, a_2, w and Δ_1), as shown in Table 3.1.

The design was obtained by adjusting the necessary core optical properties (τ_g, D, S and n_{eff}) requirements for TTDL operation, low inter-core crosstalk and robustness to fabrication tolerances [90]. To minimize crosstalk in a 7-core fiber, the cores must be distributed in the cross-sectional area of the MCF based on their n_{eff} similarity. This is necessary to avoid phase matching between adjacent cores. In typical 7-core heterogeneous designs, three core groups are enough to reduce crosstalk. Therefore, as indicated in Fig. 3.1(a), cores are grouped as follows: group #1 is comprised of core 2 (yellow core); group #2 of cores 1, 3 and 4 (blue cores); and group #3 of cores 5 up to 7 (orange cores). The minimum effective index difference between adjacent cores is around $6.8 \cdot 10^{-4}$, which leads to a threshold bending radius of 85 mm.

Overall, a design with a common group delay was obtained at the anchor wavelength λ_0 = 1530 nm, and chromatic dispersion ranging from 14.3 up to 20.3 ps/km/nm with an incremental dispersion (ΔD) of 1 ps/km/nm at λ_0. As shown in Fig. 3.1(c), the simulated group delay of each core increases linearly with the optical wavelength. Cores 3-7 provide a DGD between cores that can be tuned up to 150 ps in a 30-nm range. This range covers most of the optical C band (1530-1565 nm), which is also the typical operation bandwidth of an EDFA. On the other hand, cores 1 and 2 (i.e., the smallest cores) were more affected during fabrication but can still be used in a shorter range (up to 10 nm) with an acceptable delay mismatch (depending on the application). It's worth mentioning that all cores can be used for wavelength diversity operation and for signal distribution purposes.

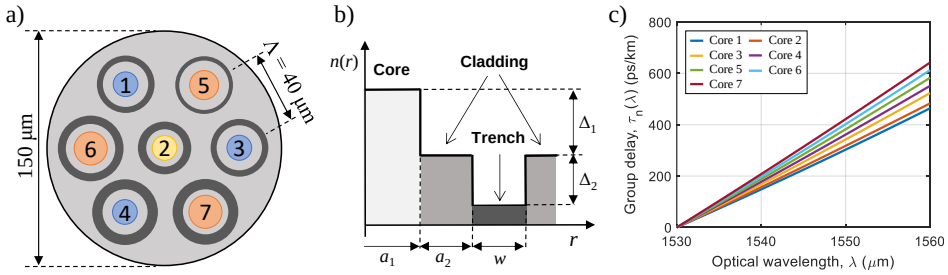

Fig. 3.1. (a) Cross-section of the designed heterogeneous 7-core fiber. Core coloring indicates the core is in a group with similar mode effective index. (b) Refractive index profile of the trench-assisted cores in the fiber. (c) Computed group delay performance with the optical wavelength.

Table 3.1. Core design parameters and optical properties at λ_0 = 1530 nm.

Core n	Core design parameters				Optical properties		
	a_1 (µm)	Δ_1 (%)	a_2 (µm)	w (µm)	D (ps/km/nm)	n_g	n_{eff}
1	3.3	0.335	5.8	3.2	14.3	1.46710	1.4455
2	3.2	0.300	2.4	4.1	15.3	1.46710	1.4448
3	3.5	0.315	4.5	4.0	16.3	1.46710	1.4455
4	3.7	0.301	3.7	3.6	17.3	1.46710	1.4455
5	4.8	0.293	5.8	3.0	18.3	1.46710	1.4463
6	5.0	0.287	4.6	6.0	19.3	1.46710	1.4463
7	5.3	0.279	3.3	6.0	20.3	1.46710	1.4463

The fabrication of the MCF was carried out by the Chinese company YOFC. The fiber has a length of 5038 meters and is coiled in a 150-mm-diameter spool. The MCF cladding diameter is 147.54 µm and the average core pitch is 40.99 µm. A couple of fan-in/fan-out devices allow us to inject/extract the light to/from the cores. Fig. 3.2(a) shows a photograph of the MCF, where each core can be distinguished by the dimension of its layers. Seven individual preforms were required to fabricate this MCF. Each preform constitutes an individual core and was created according to the core design parameters by properly scaling the radial dimensions and matching the refractive indices. Fig. 3.2(b) shows the measured refractive index profile of core 4 preform (measurement provided by YOFC). The inset corresponds to the scanning electron microscope (SEM) image of core 4.

An estimate of the proportion of the various layers and their refractive indices can be obtained using the preform refractive index profile measurements. Table 3.2 contrasts the relationships between the intended cores and the observed preforms in terms of the core-to-cladding distance, trench width with respect to the core radius, and core refractive indices. All the preforms appear to be a priori in line with our design, with only minor discrepancies that can be attributed to either manufacturing errors or measurement errors.

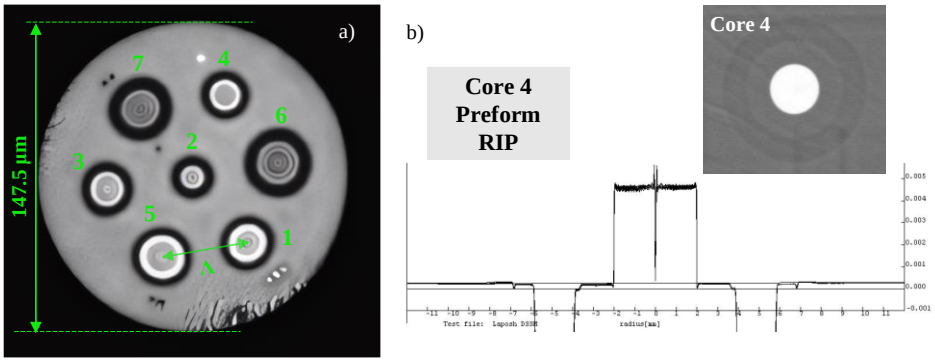

Fig. 3.2. (a) Cross-section photograph of the fabricated fiber (b) Preform refractive index profile and SEM image of core 4 (inset).

Table 3.2. Comparison of the fiber design parameters with the measured ones after fabrication.

Core *n*	Designed parameters			Measured parameters		
	a_2/a_1	w/a_1	n_1 at 633 nm	a_2/a_1	w/a_1	n_1 at 633 nm
1	1.758	0.970	1.46194	1.762	0.972	1.46234
2	0.750	1.281	1.46142	0.742	1.265	1.46173
3	1.286	1.143	1.46165	1.282	1.141	1.46213
4	1.000	0.973	1.46144	0.975	0.976	1.46162
5	1.208	0.625	1.46132	1.211	0.623	1.46152
6	0.920	1.200	1.46123	0.903	1.175	1.46158
7	0.623	1.132	1.46111	0.617	1.121	1.46133

3.3. Insertion losses and inter-core crosstalk

3.3.1. Insertion losses

First, we measured the optical power losses in the fiber. We use commercial homogeneous 7-core fan-in/fan-out devices (provided by the company YOFC) to inject/extract light from each fiber core individually, which feature average insertion losses of 3 dB and negligible crosstalk (<-60 dB). Fig. 3.3(a) shows the optical time domain reflectometer (OTDR) trace for each core obtained at the optical wavelength of 1550 nm. Optical propagation losses for the 5038-m link range from 0.18 to 0.50 dB/km. Cores 5 to 7, which have higher mode confinement, present an optical attenuation near the standard SMF attenuation (0.2 dB/km at 1550 nm). In contrast, the rest of the cores exhibit higher losses that could come from confinement losses and/or material impurities during fabrication. Fig. 3.3(b) shows the total insertion loss (IL) spectra, considering fan-in/fan-out devices and optical propagation losses, measured with a tunable laser and an IL characterization instrument. The measurement was performed by sweeping the laser from 1520 to 1570 nm. As expected, cores 1 and 4 present the worst IL of all cores. Most cores show a low IL variation with the optical wavelength, except for cores 2 and 4, which show variations of up to 2 dB. At 1550 nm, the total insertion losses range from 4.10 to 7.70 dB.

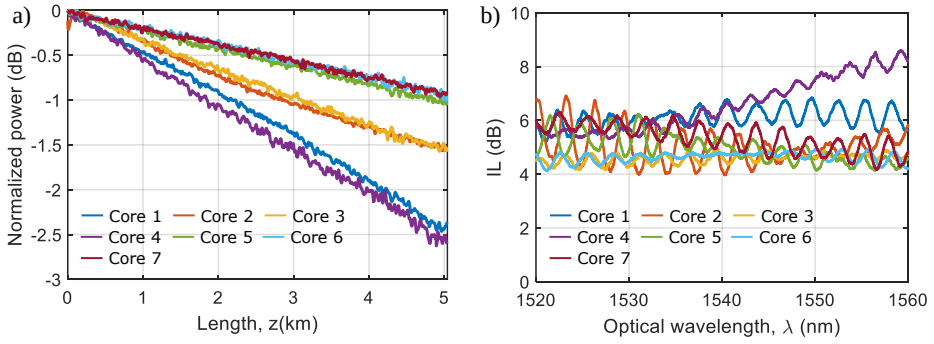

Fig. 3.3. Fiber loss characterization (a) OTDR traces at 1550 nm showing in-fiber losses per core (b) Insertion losses spectra (including fan-in/fan-out devices).

3.3.2. Inter-core crosstalk

Then, we characterized the inter-core crosstalk in the optical wavelength and time domains to investigate the risk of performance degradation in our MCF-based TTDL. In the first place we investigate the crosstalk dependence with the optical wavelength and then the time variation.

3.3.2.1. Wavelength dependence

Figure 3.4 represents the experimental setup to measure the inter-core crosstalk spectrum of each core. The core output power spectrum is measured by an Optical Spectrum Analyzer (OSA) while sweeping the optical wavelength of a tunable laser from 1520 to 1570 nm. A programmable optical switch was used to automate the process of output core selection. The optical switch and the different instruments (OSA and tunable laser) were controlled from a PC via a USB interface.

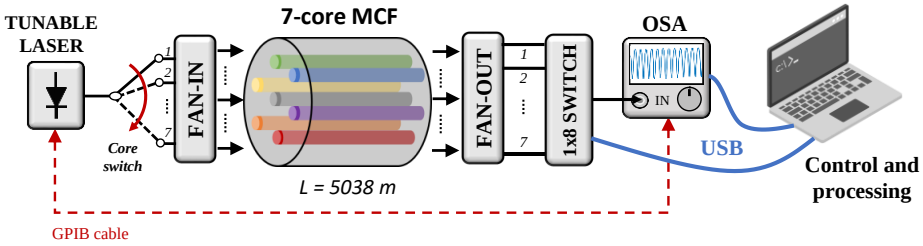

Fig. 3.4. Experimental setup for the characterization of the power spectrum of each core in the heterogeneous 7-core MCF. OSA: Optical Spectrum Analyzer.

Figure 3.5 shows the measured inter-core crosstalk spectra when the central core is excited. As stated previously, the cores can be divided into three groups based on their n_{eff}. Group #1 is composed only of core 2, which has the lowest n_{eff}. Being the central core, the coupling strength with the other cores is determined mainly by the effective index difference (Δn_{eff}) between cores. The mean Δn_{eff} with the other groups of cores is $7 \cdot 10^{-4}$ for group #2 and $14 \cdot 10^{-4}$ for group #3. This is observed in Fig. 3.5, where cores from the same group have a similar crosstalk level to core 2. Additionally, the inter-core crosstalk increases with the optical wavelength as the mode confinement decreases in the cores. Core 2 has a maximum inter-core crosstalk level of -25.1 at 1569.44 nm with core 1.

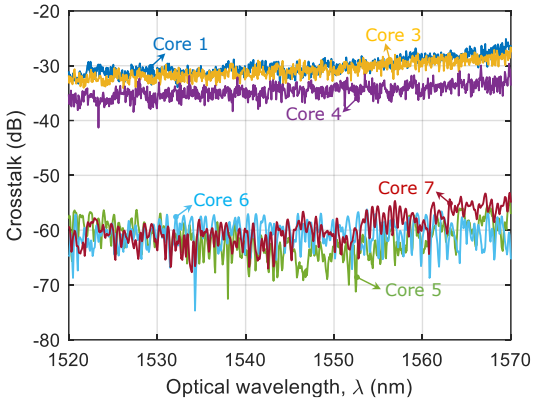

Fig. 3.5. Measured inter-core crosstalk spectra of the fiber outer cores when the central core is excited.

Figure 3.6 gathers the inter-core crosstalk spectra when cores 1(a), 3(b)-7(f) are excited individually. Here, we observe that the power in the output cores is mostly determined by the separation from the input core. This can be observed clearly for cores 3, 5, 6 and 7. In other cases, such as in the case of cores 1 and 4, crosstalk levels cannot be so easily explained, and the coupling level is higher for non-adjacent cores (core 3 in (c)). In this case, light could follow an indirect path by coupling to the central core first and from there to that particular core. Opposite to this is the case of the biggest cores, cores 6 and 7, which show a negligible level of coupling with the other cores. Finally, all cores have a significant level of coupling with the central core, with a maximum crosstalk of -24.8 dB at 1569.02 nm for the core pair 1-2.

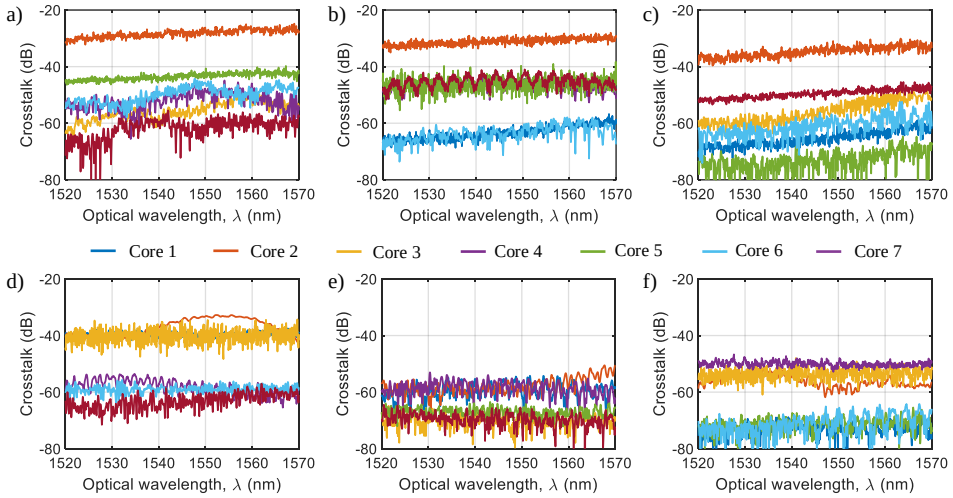

Fig. 3.6. Measured inter-core crosstalk spectra of core 1 (a), and cores 3 to 7 (c-f). Line coloring is consistent in each subfigure (as in Fig. 3.5).

3.3.2.2. Temporal variation

Lastly, we measured the temporal stability of the inter-core crosstalk by repeating the measurement from the previous section, represented in Fig. 3.4, with a time interval of 5 minutes between measurements. A different input core is connected to the fan-in device in each measurement. The spectra of all cores are measured at the output of the fiber in a controlled laboratory with temperature variations below 1ºC.

Figure 3.7 represents the temporal evolution of inter-core crosstalk for core 1 for two different wavelengths, 1530 and 1550 nm. For the first core, the measurement period was two days and a half (60 hours). Black dashed lines indicate the 10 AM time of each day in the measurement period. This was done to capture possible effects due to day-night temperature changes. We can see how inter-core crosstalk fluctuates with time and some cores show a repetitive pattern. In that regard, core 6 in (a) shows an approximate 10-dB fluctuation pattern that could be related to the temperature variation between day and night. Still, when we look at the same result for 1550 nm (b), core 6 inter-core crosstalk seems quite stable while core 7 is the one that shows a pattern. This illustrates that the inter-core crosstalk depends on the wavelength of operation. At 1550 nm, core 1 couples considerably to core 2 with an average inter-core crosstalk of -28.02 dB and a min-max variation of 3.79 dB.

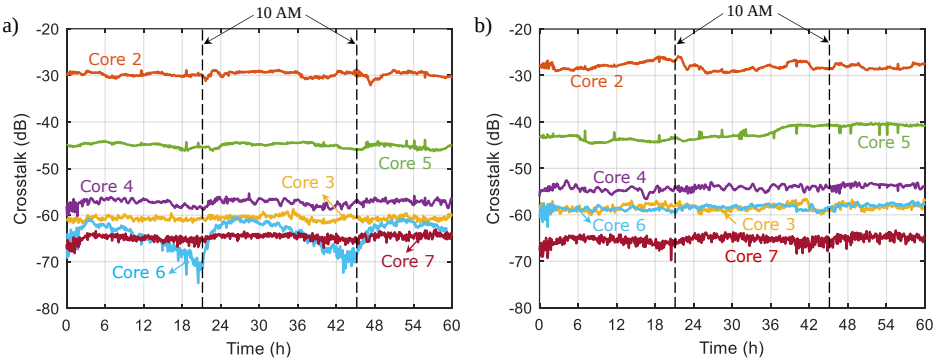

Fig. 3.7. Core 1 inter-core crosstalk 60-hour temporal evolution at (a) 1530 nm and (b) 1550 nm. Black dashed lines indicate the 10 AM time.

Figure 3.8 shows the 24-hour characterization of inter-core crosstalk for the rest of cores at 1550 nm. Similarly, inter-core crosstalk is quite stable most of the time with sudden changes in certain time periods. These changes at the start and end of the temporal evolution could be related to small vibrations of people passing by (as the room was used for other experiments). In other cases, a more "active" behavior was captured, as is the case of cores 5 in (b) and 3 (d) temporal evolution, where erratic fluctuations in the inter-core crosstalk were measured. High crosstalk fluctuations generally correspond to the cores with a low inter-core crosstalk level, for instance, core 5 in (b) or core 3 in (f), whereas cores with high inter-core crosstalk are more stable.

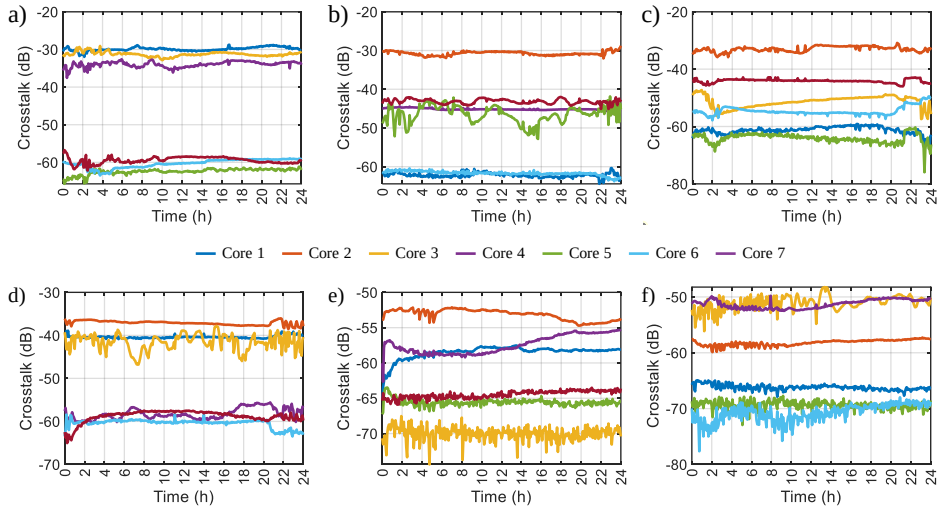

Fig. 3.8. Inter-core crosstalk temporal variation measurement at 1550 nm, when a different core is used as input: 2 (a) – 6 (f). Line color is consistent in each subfigure.

Figure 3.9 shows the joint representation of inter-core crosstalk dependence on both time and frequency for a given pair of cores. Red squares correspond the 24-hour temporal mean of inter-core crosstalk while error bars represent the standard deviation of the measurement. The inter-core crosstalk behavior for cores 1 and 2 is depicted in Fig. 3.9(a). A maximum standard deviation of 0.78 dB is obtained at 1550 nm, while the highest mean crosstalk is −26.9 dB at 1560 nm. Likewise, Fig. 3.9(b) represents the inter-core crosstalk for cores 2-4, showing a mean crosstalk of -34.3 with a standard deviation of 0.7 dB. Here we can clearly see how inter-core crosstalk tends to increase with the optical wavelength, but it also depends on the specific wavelength.

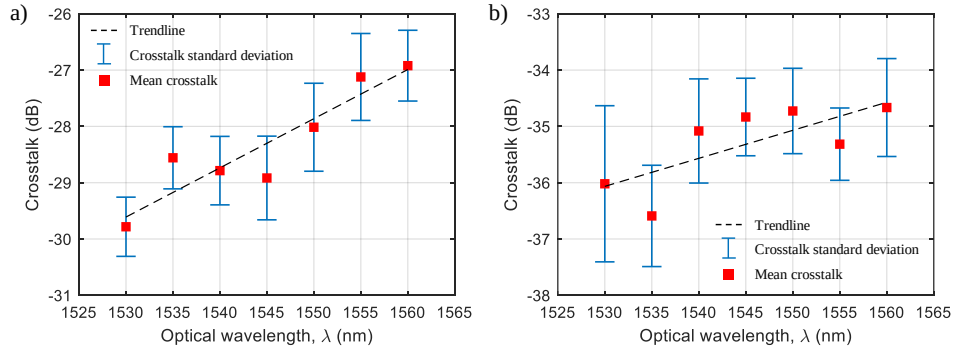

Fig. 3.9. Crosstalk time and wavelength dependence. The error bar represents the 24-hour standard deviation and the red square markers correspond to the mean crosstalk. The black dashed line shows the trend with the optical wavelength. Input core – output core: (a) 1 – 2; (b) 2 – 4.

Table 3.3 summarizes the average inter-core crosstalk of each core combination for the measurement period at 1550 nm. A maximum average inter-core crosstalk of -28 dB is obtained for cores 1-2. All in all, crosstalk levels between all pairs of cores are not strong enough to inflict any serious distortion on the signal being propagated in a given core. Only in the case of core 1 at the optical wavelength of 1560 nm, the maximum inter-core crosstalk is close to -25 dB.

Table 3.3. 24-hour average inter-core crosstalk at 1550 nm for all cores.

Output\Input	Core 1	Core 2	Core 3	Core 4	Core 5	Core 6	Core 7
Core 1	-	-30.2	-62.2	-61.2	-40.4	-58.5	-66.2
Core 2	-28.0	-	-30.7	-33.0	-37.1	-53.1	-58.2
Core 3	-58.4	-29.3	-	-51.4	-41.6	-70.0	-51.1
Core 4	-54.2	-34.3	-45.2	-	-58.3	-57.4	-51.3
Core 5	-42.4	-62.8	-46.5	-64.1	-	-65.6	-69.4
Core 6	-58.4	-61.6	-61.7	-54.6	-60.4	-	-70.8
Core 7	-65.3	-60.8	-43.2	-44.1	-58.8	-64.5	-

3.4. Performance as tunable delay line

3.4.1. Differential group delay measurement

We measured the DGDs for different optical wavelengths ranging from 1530 up to 1560 nm by means of an interferometric-based technique [92]. The setup used for this measurement is represented in Fig. 3.10. The interference pattern between two cores is captured by an OSA by sweeping the optical wavelength of a tunable laser and is then processed offline to obtain the DGD between the different core paths. A set of Variable Delay Lines (VDLs) are used to compensate group delay mismatches at the anchor wavelength λ_0 = 1530 nm. These mismatches are probably caused by fiber fabrication and differential path lengths inside the components (couplers, fan-in/fan-out devices, etc.). Core 1 is used as reference while the rest of cores are connected one by one to measure the interference. Fig. 3.11(a) shows the measured interference pattern between cores 1 and 2 in a 1-nm wavelength range. The result of post-processing the measured pattern is represented in Fig. 3.11(b), where a temporal pulse is located at the 100-ps position, indicating that is the differential delay between those cores.

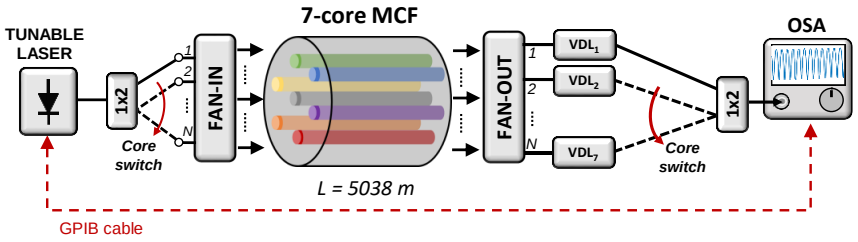

Fig. 3.10. The experimental setup used to measure the DGD between the cores of a 7-core MCF. VDL: variable delay line. OSA: optical spectrum analyzer.

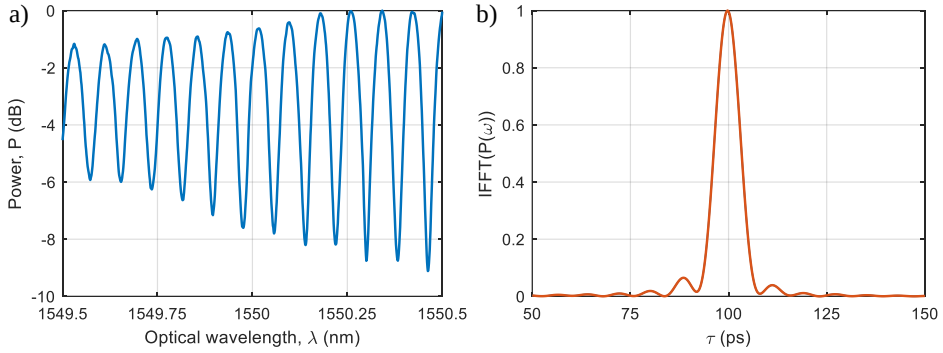

Fig. 3.11. (a) Measured spectral interference pattern of cores 1 and 2. (b) Inverse fast Fourier transform (IFFT) of the measured interference pattern.

Figure 3.12 shows the measured DGDs between core 7 and the rest, where circle markers represent the experimental values and solid lines the designed ones. We see that the measured DGDs of cores 3 to 7 match well the designed values up to a 30-nm range. Cores 1 and 2 (i.e., the smallest cores) were more affected during fabrication but can still be used in a shorter range (up to 10 nm) with an acceptable delay mismatch (depending on the application).

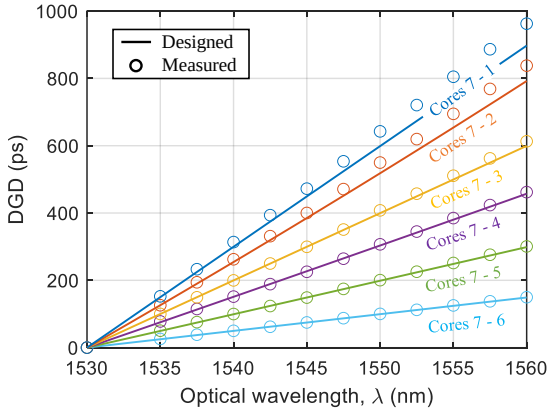

Fig. 3.12. Differential group delay performance of the fiber. The DGD is represented as the difference between core 7 and the rest of the cores. Solid lines indicate the expected performance from the design, and circles indicate the experimental measurements.

3.4.2. DGD temporal stability

We carried out an experiment to test the temporal stability of the TTDL. The optical spectrum of each core pair was measured in a similar way as in Fig. 3.10, but using an IL characterization instrument instead of an OSA. The optical spectrum was measured by sweeping a tunable laser from 1530 to 1570 nm. A 120-minute experiment was performed by triggering single sweep measurements every 30 seconds. The measurement was divided into two sets of cores, {1-2, 3-4, 5-6} and {2-3, 4-5, 6-7}, that were measured simultaneously. The differential delay was obtained by calculating the inverse Fourier transform as in the previous section. Fig. 3.13 represents the normalized differential group delay between adjacent cores at 1540 nm (a) and 1550 nm (b). Measurements were performed at room temperature in our laboratory, with a maximum temperature fluctuation below 1 ºC during the measurement time. The results provide DGD variations below 1.1 ps at 1540 nm and below 0.3 ps at 1550 nm. This shows that for a relatively large time period, the delay between cores is highly stable.

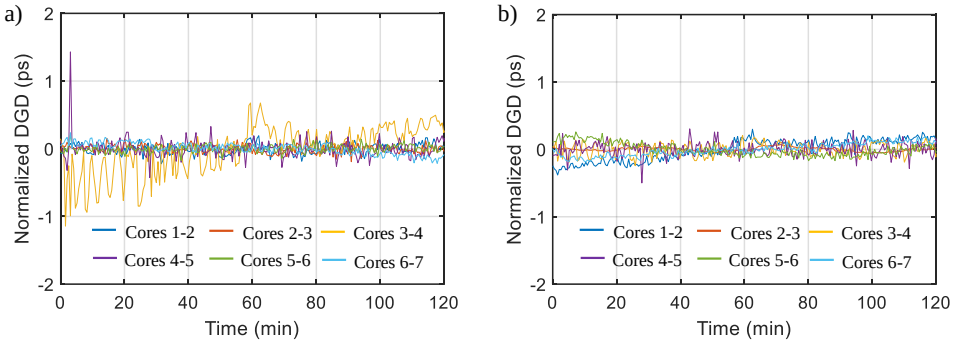

Fig. 3.13. Normalized DGD change between adjacent cores at the optical wavelength of (a) 1540 nm and (b) 1550 nm.

3.4.3. Chromatic dispersion

We also measured the chromatic dispersion by evaluating the CSE that affects the RF response of the 5038-m link. Fig. 3.14 represents the setup scheme used to measure this effect. A tunable laser generates the optical signal, which is then modulated by a dual-drive EOM. An RF signal generated by a vector network analyzer (VNA) feeds the modulator. The signal is then injected into one of the MCF cores via a fan-in device. At the output of the MCF, the signal is extracted by a fan-out device and converted to the electrical domain at the photodetector (PD). The RF response of the channel is obtained by sweeping the RF frequency spectrum up to 50 GHz.

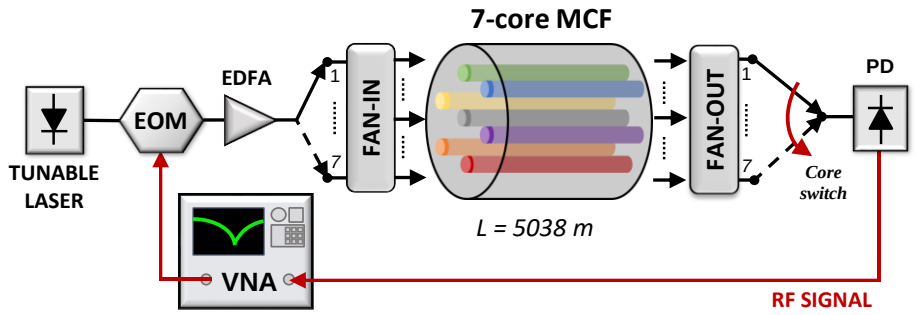

Fig. 3.14. Experimental setup to measure the RF response of each fiber core. EOM: electro-optic modulator. EDFA: Erbium-doped fiber amplifier. VNA: vector network analyzer. PD: photodetector.

Because of chromatic dispersion in the fiber link, modulation sidebands experience slightly different delays when propagating. At a certain RF frequency this produces a destructive interference when the signal is detected. While this is a detrimental effect on the channel response, it can be used in our favor to measure the chromatic dispersion. The intensity of the detected RF signal can be approximated by [93]:

$$I(f) \propto \cos\left[\frac{\pi\lambda_0^{\,2} D(\lambda) f^{\,2} L}{c} + \tan^{-1}(\alpha_{lw})\right], \tag{3.1}$$

where λ is the optical wavelength, D is the chromatic dispersion, f is the RF frequency, L is the link length, c is the speed of light, and α_{lw} is the modulator chirp parameter. The frequency at which a null is produced can be derived from the previous expression such that:

$$f_k = \sqrt{\frac{c}{2D(\lambda_0)L\lambda_0^{\,2}}\left(1 + 2k - \frac{2}{\pi}\tan^{-1}(\alpha_{lw})\right)}, \tag{3.2}$$

where k is the order of the resonance. With this expression, we can see that the location of the zeroes depends mainly on the chromatic dispersion and on α_{lw}. This last parameter is characteristic of each modulator, and it can be adjusted by tuning the bias voltage applied to it [93]. Depending on the chirp sign, the position of the notch is either lowered (positive chirp) or increased (negative chirp). The problem comes when the optical wavelength changes, because the bias voltage needs to be re-adjusted to match the quadrature point again. To evaluate this effect, an experimental measurement was performed on a 21.2-km long single-core SMF for the optical wavelength range of interest here (1530-1560 nm). The results are gathered in Fig. 3.15 and show the chromatic dispersion value calculated from the first frequency response notch (blue line). An erratic dispersion value is obtained in this case with no clear wavelength dependence. The compensated result (orange line) was obtained by getting the first two consecutive frequency zeroes and then calculating the accumulated dispersion per total length as:

$$D \cdot L = \frac{c}{(f_{k+1}^2 - f_k^2)\lambda_0^2}. \tag{3.3}$$

By doing this, the chirp effect on the chromatic dispersion measurement can be evaded, and a more accurate result can be obtained. We can also obtain α_{lw} by deriving an expression from Eq. (3.2). The calculated chirp parameter for the modulator used here ranges from 0.06 to 0.23.

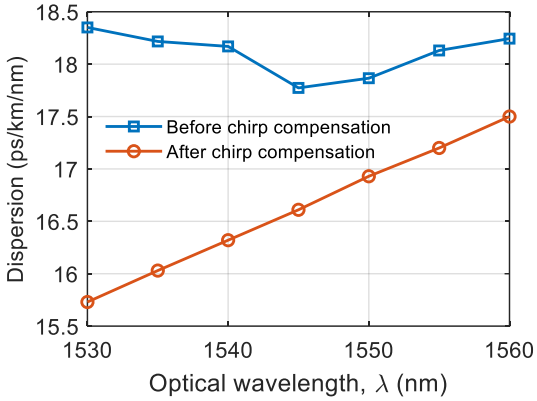

Fig. 3.15. Dispersion measurement result of 21.2-km long SMF fiber using the CSE effect.

Figure 3.16 gathers the measured RF response of the fiber at 1530 nm (a) and 1550 nm (b). Here we took advantage on the chirp effect, by using a modulator with a high positive chirp. This shifts the frequency zeroes towards lower frequencies, thus allowing us to measure all the cores with a 50-GHz VNA. In particular, this enabled the measurement of core 1 notch at 1530 nm, as in the case with no chirp the second resonance would be in a much higher frequency, and we could not obtain an accurate result.

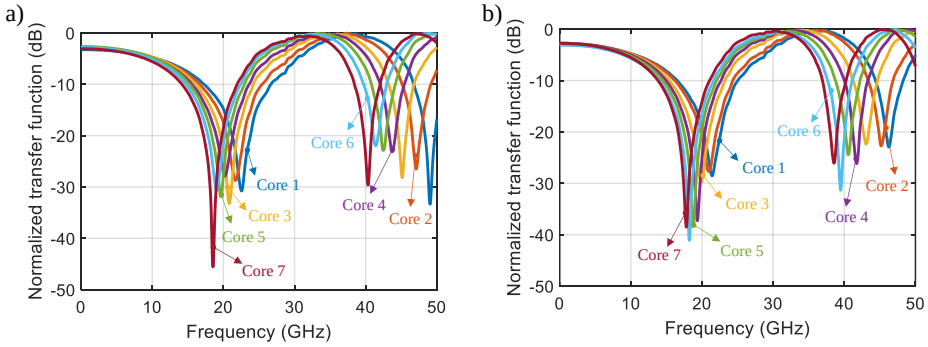

Fig. 3.16. Measured RF response for each core in the fiber at the optical wavelength of (a) 1530 nm and (b) 1550 nm.

Finally, as the measured dispersion differs from the design and what we truly care are the dispersion differences, Fig. 3.17 shows the measured incremental dispersion ($D_7 - D_n$, $n = 1, 2, \ldots, 6$) as a function of the optical wavelength in comparison to our design (dashed lines). We see how the chromatic dispersion for cores 3 to 7 matches well the designed values up to a 30-nm range, while cores 1 and 2 were more affected by fabrication and do not preserve the designed chromatic dispersions.

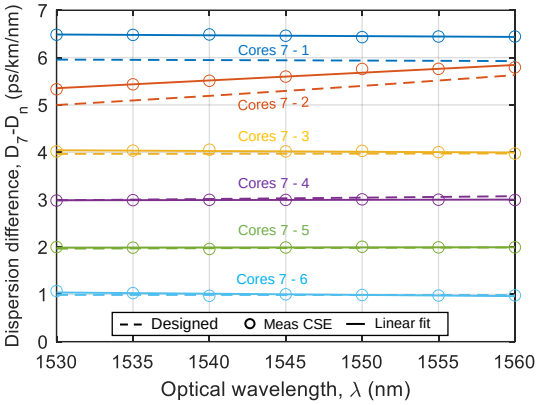

Fig. 3.17. Measured results for the dispersion difference between cores (circles). The designed dispersion difference is represented for comparison (dashed lines). A linear fit of the measured results is represented as a visual aid (solid lines).

3.5. Performance degradation sources

3.5.1. Temperature effect

3.5.1.1. Context

The effect of temperature over the chromatic dispersion and group delay on different types of optical fibers has been studied in the past [94], [95]. As stated in [96], the change of the group delay is caused by the refractive index change in the core and by fiber elongation (thermal expansion). The calculated combined impact of these two effects results in a group delay change of 40 ps/km/K for unjacketed silica fibers. In the case of P_2O_5/GeO_2 doped fibers, the group delay change is experimentally measured to be 35.7 ps/km/K. This could pose a problem for time-delay sensitive applications, as the functionality of the implemented application depends on specific differential delays. Fortunately, it has been proven that MCFs have an advantage over single-core fibers as the measured dynamic skew between the cores of a seven-core homogeneous MCF is 40 times lower than the skew between two spans of SMFs of similar length [97]. In that work, the fibers involved were placed in a temperature controlled chamber (TEC) and the temperature was varied to capture the dependence of the group delay with the temperature. After temperature stabilization, the skew of the link formed by SMF spans continued to change whilst the one composed of MCFs did not. Here we check the effect of temperature changes over the DGD on the heterogeneous 7-core MCF.

3.5.1.2. Experimental measurement

Figure 3.18 depicts the experimental setup to measure the DGD between the central core and the outer cores of the heterogeneous 7-core TTDL MCF. First, the MCF spool was placed inside the TEC together with the fan-in/fan-out devices. A 1x2 coupler divides the signal coming the tunable laser into two paths, which are injected to the MCF via a fan-in device. One path goes to the central core and the other path to one of the outer cores. After propagation through the MCF, individual fiber pigtails are connected to the fan-out device, forming the compensation stage together with VDLs. The signal from the central core and an outer core is coupled together to obtain the interference pattern, which is then captured by the OSA. The outer core is switched every time to obtain the DGD with all the cores. The interference pattern is postprocessed in the same way as in section 3.4.1.

Group delay equalization was performed after setting the TEC to 25ºC for two hours. The group delay of the central core was adjusted to be around 100 ps upon the rest of the cores, avoiding zero-delay situations where the interferometric method is less accurate. The optical wavelength was centered around 1550 nm with a sweeping range of 1 nm. The DGD between core 2 and the rest of the cores at 25 ºC is used as reference for the rest of measurements. In each measurement, the TEC was left heating or cooling for several hours to ensure temperature stabilization. Five measurements were taken for each core pair and per temperature step to average the result, and the maximum standard deviation is below 2 ps.

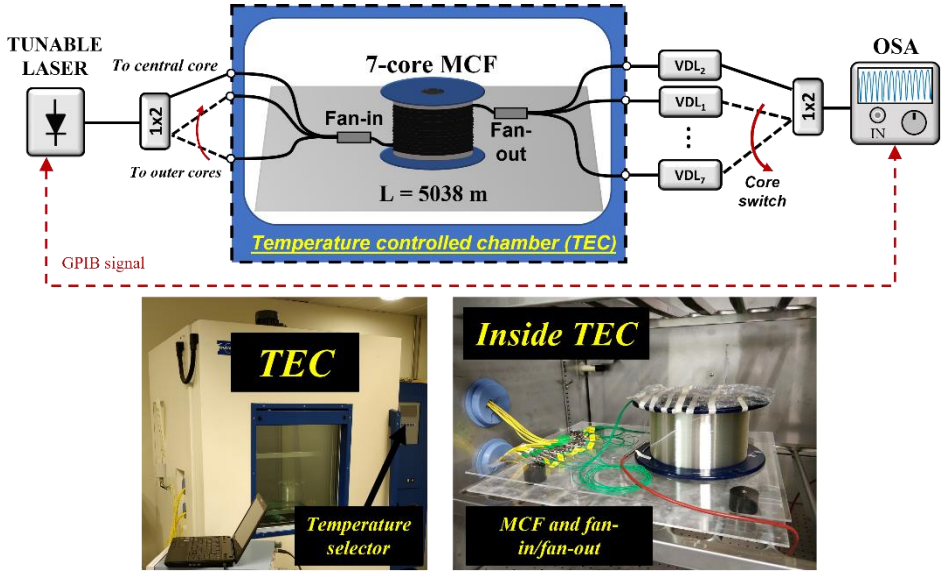

Fig. 3.18. (Top) Schematic of the experimental setup for the measurement of DGD between central core and outer cores at different temperatures. (Bottom) The TEC used in this experiment (left) and TEC inside with the MCF, fan-in/fan-out devices and input/output pigtails (right). VDL: variable delay line. OSA: optical spectrum analyzer.

Figure 3.19 shows the average normalized DGD between the outer cores and the central core when the temperature is changed from 5 to 55 ºC. A maximum 35.28-ps variation is obtained for core 7 in a 50-ºC range. However, since humidity in the TEC

decreases and increases considerably for higher and lower temperatures, we take a shorter temperature range, for instance from 15 to 35 ºC. In this range, the maximum DGD remains below 15.08 ps (less than 1 ps/ºC). This goes in line with the experimental results presented in section 3.4.2, where the measured dynamic DGD between cores is below 1 ps for a less than 1ºC temperature variation.

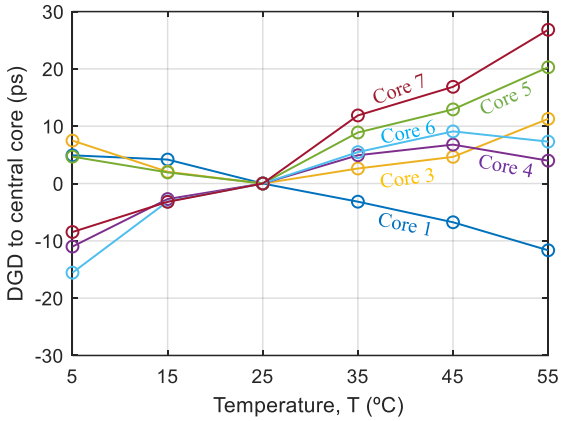

Fig. 3.19. Measured normalized DGD to the central core as a function of temperature.

All in all, the experimental results agree well with literature as a similar result was obtained in [98] for 7-core and 19-core homogeneous MCFs. In both cases, static delays are of the order of nanoseconds while dynamic delays are of the order of tens of picoseconds. In that work, the random DGD behavior with the temperature is attributed to polarization mode dispersion (PMD). Related to this, the use of polarization trackers and thermal insulation allowed the measurement of a remarkably low inter-core skew change of 40 fs/km/ºC on a homogeneous 7-core MCF [99]. This low skew change in MCFs allows clock-synchronized transmissions without active phase tracking on data center networks. Besides, it has been shown that in an actual fiber deployed scenario (MCF testbed in the Italian city of L'Aquila), the measured dynamic skew is of the order of picoseconds [100].

3.5.2. Fiber bending and twisting

3.5.2.1. Introduction

Fiber bending is known to produce excess losses because of mode deformation [40], [101] and is one of the main concerns in fiber designs. Apart from the losses, bends induce a refractive index change on the fiber that ultimately affects its propagation constants (i.e., group delay). This is especially critical in MCFs because each core experiences a group delay change that depends on the bend direction and its position in the cladding. The mismatch introduced by bends on the delay of a spatial path could degrade TTDL performance and affect its operability. Therefore, we study the effect of bending and twisting on the group delay of a 7-core MCF (with one central core and six outer cores).

3.5.2.2. Theoretical modelling

First, we model the equivalent refractive index distribution $n_{eq,m}$ of a bent fiber core m as described in [40]:

$$n_{eq,m} = \left[n_m^2 \left(1 + 2\frac{r_m}{R_b}\cos\theta_m \right) \right]^{1/2} \approx n_m \left(1 + \frac{r_m}{R_b}\cos\theta_m \right), \tag{3.4}$$

where R_b is the bending radius, n_m is the refractive index of core m in the corresponding straight fiber and (r_m,θ_m) are the local polar coordinates of core m, as shown in Fig. 3.20(a). Cores located on the right-hand side of the tangential plane (red dotted line) increase their refractive index, while cores on the left side decrease their refractive index. Fig. 3.20(b) represents the refractive index profile of cores located along the curvature line.

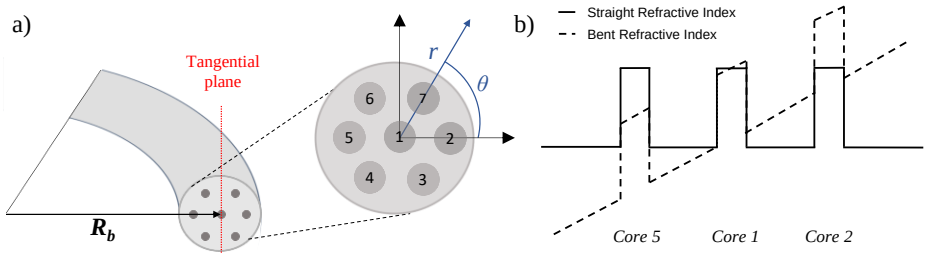

Fig. 3.20. (a) Multicore fiber curvature with a bending radius R_b and local polar coordinates (r,θ) indicated in the MCF cross-section. (b) Effect of the fiber curvature on the refractive index profile of cores 1, 2 and 5 as compared to the straight condition.

The effect of fiber twisting with a constant twist rate γ can be understood as a linear rotation of the fiber cross-section along a given fiber length L; in other words, as a linear increment of the angle θ_m for a given core m. If we applied an ideal curvature with a fixed bending radius over the whole fiber length, the angle θ_m of each core m would be preserved. The DGD between the outer cores and the central core would then accumulate linearly with the fiber length unless that core m is placed at an angle $\theta = \pi/2 + k\pi$, $k \in Z$ (where the core belongs to the curvature tangential plane and the DGD is canceled out). The longitudinal evolution of the angular coordinate of core m in the cross-sectional area of the fiber can be denoted by $\theta_m = \theta_{m,i} + \gamma z$, being z the longitudinal coordinate and $\theta_{m,i}$ the initial angular position (i.e., when $z = 0$). The worst case DGD of a core with group delay τ_m occurs when $\theta_{m,i} = k\pi$, and can be calculated as in [102]:

$$DGD_{Worst\ case,\ accumulated} = \frac{\tau_m r_m L}{R_b} \mathrm{sinc}(\gamma L)(-1)^k . \tag{3.5}$$

3.5.2.3. DGD measurement

The effect of bending and twisting on the DGD of a commercial homogeneous 7-core fiber (*Fibercore MCF*) was investigated following the experimental setup illustrated in Fig. 3.21. The fiber has step-index cores (core radius $a = 4$ µm and core-to-cladding relative index difference $\Delta = 0.31\%$) and a core pitch of 35 µm. We measured the

DGDs between straight and bent fiber conditions over a small piece of fiber (L = 1 m). This way, we can carry out the straight fiber measurements and properly manage the applied twist while curving the fiber. Three plastic cylinders were fabricated in a 3D printer with the specific radii of 25, 35 and 50 mm (below the typical fiber spool radius). These small bending radii are applied to force a representative variation in the core group delays when the fiber is bent. As Fig. 3.21 shows, the fiber is locked with clamps at both ends, before fiber winding, a first clamp holds the fiber at one point, while the second clamp maintains the curvature and twisting conditions after winding.

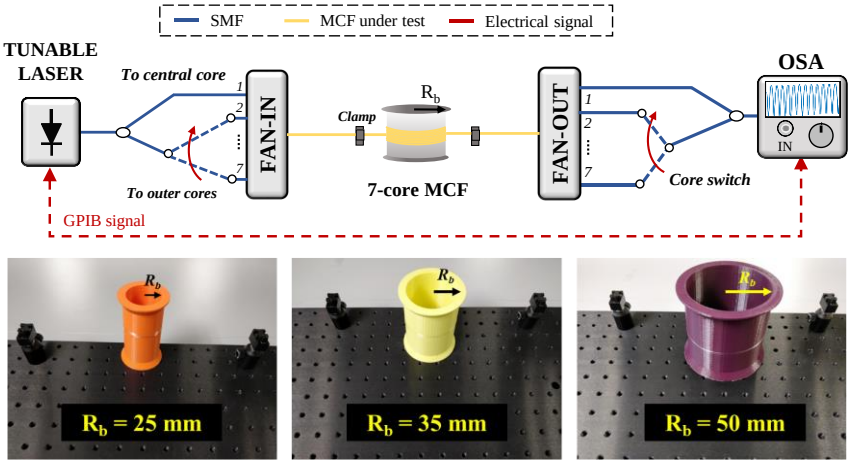

Fig. 3.21. (Top) Experimental setup for the measure of the DGD between central and outer cores. (Bottom) Photographs of the 3D-printed cylinders used to wind the MCF.

The optical signal coming from a tunable laser is injected into the central core (Core 1) and one of the outer cores (Cores 2-7) of the MCF. Prior to each measurement, we adjusted the optical paths for the central core to have a differential delay of around 20 ps greater than the outer cores. This was done to avoid zero-DGD situations in which the DGD measurement method is not accurate. At the fiber output, both signals are coupled together and injected into an OSA. Sweeping the optical wavelength of the laser reveals the interference pattern from which we measure the differential delay between both cores, [92].

Table 3.4 gathers the measured DGD values between the outer and central cores for the three bending radii when two different conditions are applied: (a) the fiber is bent among the cylinder carefully trying not to induce any fiber twisting; and (b) the fiber is bent while forcing an intentional twist. For the forced twist experiments, the fiber twisting was manually performed by introducing several intentional rotations distributed along the 1-m fiber while fiber winding. We can see as expected that the DGD is bigger as the bending radius is smaller, as well as how twisting the fiber produces an important reduction on the core DGDs. Slightly asymmetric behavior between the cores with opposite delay variation can be attributed to both fabrication mismatches on the core positions (radial, r_m, and angular, $\theta_{m,i}$) with respect to the ideal configuration and also to measurement tolerances.

Table 3.4. Normalized inter-core DGD (ps/m) values measured between pair of cores for different bending and twisting conditions.

Cores	No twist			Twist		
	25 mm	35 mm	50 mm	25 mm	35 mm	50 mm
1-2	-3.1	-2.0	-2.7	-1.0	-0.8	-0.7
1-3	2.1	1.3	-0.4	-0.5	0.1	-0.3
1-4	4.8	3.5	2.3	0.7	0.9	0.2
1-5	2.2	1.9	2.4	1.0	0.1	0.0
1-6	-2.4	-1.6	-0.3	0.3	-0.4	0.3
1-7	-6.0	-4.1	-3.3	-1.2	-1.3	-1.1

Figure 3.22(a) depicts the core DGDs located inside the fiber cross-section for the representative case of R_b = 35 mm with and without twist. The position of the tangential plane has been estimated from the core DGD measurements gathered in Table 3.4. As shown, cores located at one side of the tangential plane have DGDs with opposite signs than those located in the other side. Moreover, the DGD of those cores located in opposite radial positions (i.e., $\theta_{m,i} - \theta_{n,i} = k\pi$) have similar absolute value (ideally identical) but opposite signs. The worst-case DGD variation occurs when the core forms an angle of $\pm\pi/2$ with the tangential plane, but this case cannot be measured with precision since we do not have control over the curvature plane (which we assume random) during the measurement process. However, we can estimate the worst-case DGD from the measured values by doing a plane correction. For instance, in the case of the tangential planes of Fig. 3.22(a), we can apply the plane correction θ_c (in degrees) that satisfies:

$$\frac{DGD_2}{\cos(60-\theta_c)} = \frac{DGD_7}{\cos(\theta_c)}, \tag{3.6}$$

being DGD_2 and DGD_7 the differential group delays of cores 2 and 7, respectively. Once the angle of the plane correction θ_c is calculated, we can estimate the worst-case DGD as $DGD_{worst\text{-}case} = DGD_7/\cos(\theta_c)$. Following an analog procedure, we can estimate the worst-case DGD for each measured case. Fig. 3.22(b) shows the estimated worst-case DGD from the measured values as compared to the theoretical curves obtained from Eq. (3.5) (solid line), when we fix the twist rate to 0. We see that the measured worst-case DGDs in the absence of twist are well-matched with the theoretical curves. On the other hand, we observe an important reduction on the worst-case DGD when an intentional twist is applied while bending the fiber, as expected.

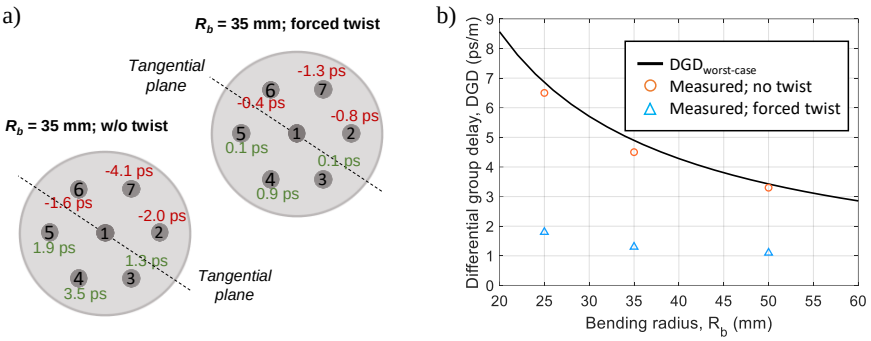

Fig. 3.22. (a) Measured core differential group delays between bent and unbent fiber for a bending radius of 35 mm with and without twist. (b) Differential group delay dependence on the bending radius: Solid and dashed lines correspond to the worst-case computed theoretical responses without twist, while error bars represent the worst-case experimental values (red bars: no twist, blue bars: forced twist).

3.5.2.4. Impact on MWP filtering application

Non-desired group delay variations between cores could affect applications where time-delay control and synchronization play a crucial role, as it is our case here. Therefore, we have experimentally evaluated how bending and twisting affect a delay-sensitive application such as Microwave Photonics signal filtering. We implemented a 7-tap finite impulse response filter with a free spectral range (FSR) of 10 GHz by adjusting the group delay difference between adjacent filter samples (or basic differential delay) to $\Delta\tau$ = 100 ps. The filter frequency response was measured for two different fiber conditions: (1) bent without intentional twist and (2) bent with a forced twist, each one for three different bending radii: 25, 35 and 50 mm.

The experimental setup for measuring the filter electrical response is depicted in Fig. 3.23. The optical signal is generated by a broadband source (BS) which is then filtered to obtain an optical carrier with a -3-dB bandwidth of 0.3 nm. The use of a BS makes the filter response insensitive to environmental changes such as temperature or vibrations. The optical signal is then modulated and equally launched to all cores using a 1x8 coupler and a fan-in device. The fiber condition is change for each curvature/twist case similarly to what we did with the group delay measurement. At each fan-out output, 2 cm of SMF (approximately 100-ps delay) were added incrementally from tap to tap to obtain the basic differential delay. A series of VDLs at the output of the MCF were used to finely tune the tap delays, while variable optical attenuators (VOAs) keep a uniform amplitude distribution. Output signals are combined before photodetection. The electrical response is measured by a VNA, which also generates the RF input signal.

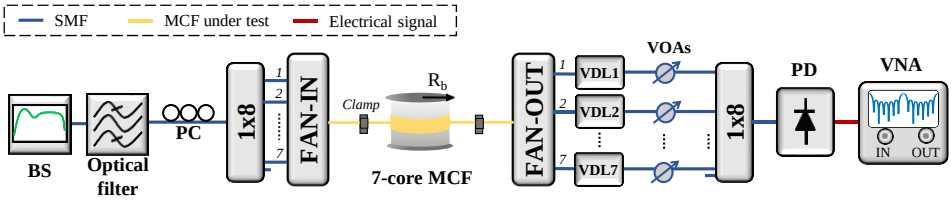

Fig. 3.23. Setup scheme for the experimental measure of the microwave signal filtering response. EOM: electro-optic modulator. VNA: vector network analyzer. VOA: variable optical attenuator. VDL: variable delay line. PD: photodetector. PC: polarization controller. BS: broadband source.

Figure 3.24 illustrates the measured filter transfer function as a function of the RF frequency for the different bending/twisting cases stated before. The blue solid line represents the case in which the fiber is wound over the cylinder with a forced regular twist and the red dash-dotted line represents the case where the fiber is bent trying not to produce any twist. In the absence of twist, the filter response when the fiber is bent at 25 mm, Fig. 3.24(a), experiences distortions even in the first resonance. When the curvature radius is 35 mm, Fig. 3.24(b), the distortions are less important but still present at high frequency resonances. Finally, in Fig. 3.24(c), distortions become relevant only at the last resonance. In all cases, the filter response greatly improves when the intentional twist is applied due to the reduction in the DGDs, as we have seen in section 3.5.2.3. This is particularly important for high-frequency resonances where bent-induced DGD deviations have a strongest effect on the RF response. These results display how applying a moderate twist to the fiber helps to reduce the DGD variations introduced by the fiber itself and, thus, improve the performance of the implemented signal processing functionality.

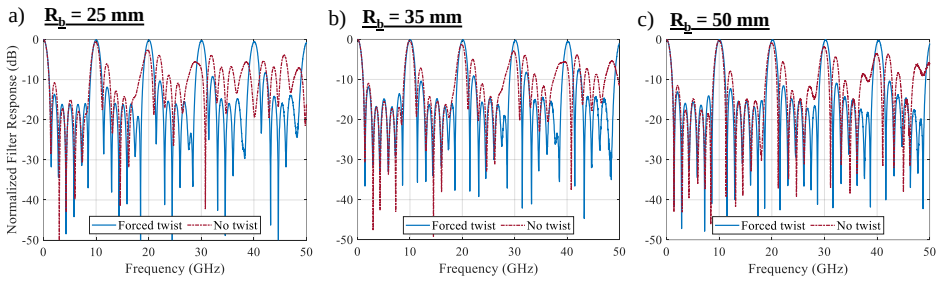

Fig. 3.24. Measured filter response for: (solid blue) fiber bent with high twist, (dash-dotted red) fiber bent with low twist; and different radius: (a) 25 mm, (b) 35 mm, (c) 50 mm.

3.6. Conclusions

In this chapter, we have reported the characterization of a 5-km long dispersion-diversity heterogeneous 7-core fiber that operates as a TTDL. First, we measured the optical insertion losses (including fiber propagation) and inter-core crosstalk for all cores, accounting for both optical wavelength dependence and temporal fluctuation. The measured propagation losses range from 0.18 up to 0.50 dB/km for the different fiber cores, while the overall insertion losses, including both fan-in/fan-out insertion

losses and fiber propagation losses along the 5-km propagation, range from 3.9 to 7.7 dB at 1550 nm. The highest inter-core crosstalk is -25 dB between cores 1 and 2 at 1560 nm. Further, the performance of this fiber as a TTDL was characterized by measuring the DGD and the chromatic dispersion of each core. The results are in a good agreement with the designed values for cores 3-7, while cores 1 and 2 seem to be more affected by fabrication. We also evaluated the temporal stability of the TTDL, and we found DGD to be very stable with variations below 1 ps in a 2-hour measurement period at room temperature in our laboratory, with a maximum temperature fluctuation below 1 ºC. Related to this, we measured the impact of temperature as well over the DGD, displaying similar results as the ones found in literature. The worst-case DGD change with temperature is less than 1 ps/ºC. This goes in line with the measured DGD variation over time and indicates a gradual temperature variation doesn't have a meaningful impact on the TTDL performance.

Additionally, we modelled and measured the effect of bending and twisting on the DGD in a homogeneous 7-core commercial fiber. Although this experiment was performed on a different fiber, it should be pointed out that these results can be extrapolated to any other 7-core fiber with hexagonal core disposition, since the DGD variation due to fiber curvatures depends mainly on the position of the cores, while the fact of having heterogeneous cores is, in comparison, negligible. The results showed that the variations on the DGD due to fiber curvatures cannot be neglected, although twist-induced perturbations can help to diminish their effect. But eventually, we have to take into account that this detrimental effect is generally static and thus it can be easily compensated after fiber deployment.

Chapter 4

Heterogeneous 7-core MCF-based TTDL: Experimental Demonstrations

4.1. Introduction

In this chapter, we present several experimental demonstrations in which the dispersion-diversity heterogeneous 7-core MCF is employed for signal distribution and processing applications. Due to the tailored propagation characteristics of each fiber core, we obtain dispersion-managed distributed signal processing that can be tuned by varying the optical wavelength.

Regarding microwave signal processing, we demonstrate, first, the reconfigurable characteristics of the implemented TTDL when it is applied to radiofrequency signal filtering. Then, optical beamforming for phased array antennas is demonstrated on an actual antenna by measuring its radiation pattern. Lastly, we realize arbitrary waveform generation applied to the generation of ultra-wideband waveforms. A brief review of the operation principle of every application is presented at the beginning of each section.

In addition, we realize a signal transmission experiment with a 5G radio signal to evaluate the possible detrimental effects introduced by the fiber.

4.2. Microwave signal filtering

4.2.1. Introduction

An MWP filter is an optical structure that aims to perform the same function as its electrical counterpart with the intrinsic advantages of photonics (electromagnetic immunity, low loss, high bandwidth, reconfigurability, tuneability, etc.) [9], [77], [103]. We can define its frequency response based on discrete-time signal processing, where a different number of weighted and time-delayed samples of the RF signal are generated in the optical domain and combined prior detection. Two main configurations can be found based on the number of samples, finite impulse response (FIR) and infinite impulse response. Considering the FIR filter, the transfer function can be expressed as:

$$H\left(f_{RF}\right)=\sum_{n=0}^{N-1}a_n e^{-i2\pi n f_{RF}\Delta\tau}, \tag{4.1}$$

where a_n represents the weight of the sample n, N the number of samples, $\Delta\tau$ the delay difference between samples, and f_{RF} the RF frequency. The differential delay $\Delta\tau$ defines the periodicity of the spectral response or FSR, FSR = 1 / $\Delta\tau$. Depending on the optical source characteristics, an MWP filter operates either in the incoherent (i.e., $\Delta\tau >> \tau_c$) or the coherent regime ($\Delta\tau << \tau_c$), being τ_c the coherence time of the optical source. In the coherent regime, the filter's response is susceptible to environmental changes. That is impractical on long-length components such as optical fiber links. For that reason, we will focus exclusively on the incoherent regime. In the next section, we experimentally demonstrate the implementation of incoherent microwave signal filtering with our MCF exploiting both space and wavelength diversity domains, as introduced in section 2.2.2.

4.2.2. Experimental demonstration of microwave signal filtering

As we see in Eq. (4.1), the filter response depends mainly on the sample amplitude and differential delay. To generate the given signal samples, we carried out two different experiments depending on the diversity domain exploited. Briefly, we find that in the spatial diversity domain, the differential delays come from the combination of the cores at the MCF output when a single optical carrier is modulated and coupled into them (as demonstrated by Eq. (2.11)). In the wavelength domain, an array of lasers operating at different equally-space wavelengths is injected into one core. In this case, the sample time delays are created by the different propagation velocities experienced at each wavelength. Therefore, the carrier separation sets the time delay between samples (as shown in Eq. (2.13)). We observe that for the same carrier separation, we can use a different core to tune the filter response. Furthermore, we can utilize both multiplexing diversities (space and wavelength) at the same time by using an array of lasers in the same configuration.

Figure 4.1 represents the experimental setup that is used to measure the RF filter transfer function. The optical signal is generated by: (1) a BS (required to avoid optical coherent interference) followed by a 0.1-nm-bandwidth optical filter (which is necessary to avoid high-frequency fading effects due to the BS, [104]) in the

spatial-diversity domain; (2) a 4-tuneable-laser array in the wavelength-diversity domain. A dual-drive EOM modulates the optical signal with the RF signal generated by a VNA. Single-sideband modulation is implemented to avoid the CSE. The signal is then split and injected into all the fiber cores using a fan-in device. After propagating through the fiber, the signals are extracted using a fan-out device. These signals are treated differently depending on the operation regime. In the spatial-diversity domain, all cores are combined at the fiber output and VOAs finely equalize the output power of the samples for uniform amplitude distribution. In the wavelength-diversity domain, a single core is chosen to create the RF filtering functionality. VDLs were used to compensate for group delay fabrication mismatches at the anchor wavelength. An optical switching matrix is used to select: (1) a set of *N* cores or (2) a specific core *n*.

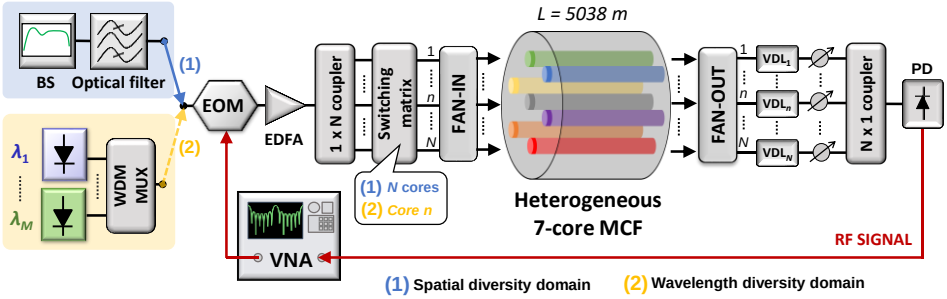

Fig. 4.1. Experimental setup to measure the RF transfer function response (S21) in the spatial-diversity domain (1) and wavelength-diversity domain (2). The optical signal is generated in a different manner in each domain. A switching matrix selects the appropriate cores in each case as well. EOM: electro-optic modulator. EDFA: Erbium-doped fiber amplifier. VDL: variable delay line. VNA: vector network analyzer. VOA: variable optical attenuator. PD: photodetector. BS: broadband source. WDM: Wavelength Division Multiplexing.

First, in the spatial-diversity experiment, we evaluate the 5-tap filter built by cores 3 to 7. Fig. 4.2 shows the measured RF filter transfer function up to 30 GHz for different operation wavelengths. Blue solid, red dashed, yellow dash-dotted, purple dotted and green solid lines represent the measured filtering response at the optical wavelengths of 1540, 1545, 1550, 1555 and 1560 nm, respectively. The differential delay between samples corresponding to these optical wavelengths is 50, 75, 100, 125 and 150 ps. Taking into account that the filter FSR is given by the inverse of the differential delay, we observe that varying the central wavelength changes the FSR from 20 GHz at 1540 nm down to 6.7 GHz at 1560 nm. We appreciate no significant degradation in the lowest-order resonances and the main-to-secondary sidelobe level is generally below -10 dB. Only at higher-order resonances and for an operation wavelength far from λ_0, the filter response distorts a little bit. Moreover, we must note that we can continuously reconfigure the filter FSR from 6.7 GHz up to the mm-wave band by properly tuning the operation wavelength from 1560 down to 1530 nm.

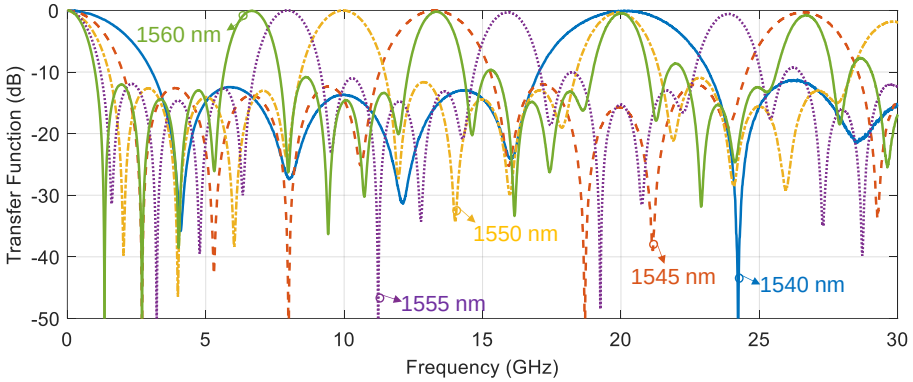

Fig. 4.2. Measured 5-tap RF signal filtering response at different optical wavelengths when the TTDL is operated on the spatial-diversity domain.

Second, in the wavelength-diversity experiment, we used an array of 4 lasers operating at optical wavelengths starting at 1540 nm with 1-nm and 2-nm carrier spacing to exploit the wavelength diversity regime. As representative cases, Fig. 4.3 shows the measured transfer functions of the 4-tap filters created in cores 1, 2 and 7 of the MCF for a carrier spacing of 1 nm (a) and 2 nm (b). Blue solid, red dashed and yellow dash-dotted lines represent the filter responses for cores 1, 2 and 7, respectively. In this case, the filter FSR depends inversely on the chromatic dispersion of the core (see Eq. (2.13)). The resulting FSRs are 14, 13.2 and 9.8 GHz for the 1-nm spacing case and 7, 6.5 and 4.8 GHz for the 2-nm spacing case, respectively for cores 1, 2 and 7. The filter FSR reconfigurability in this regime is given by the wavelength separation of the optical sources. As in the spatial-diversity case, we observe main-to-secondary sidelobe levels below -10 dB generally.

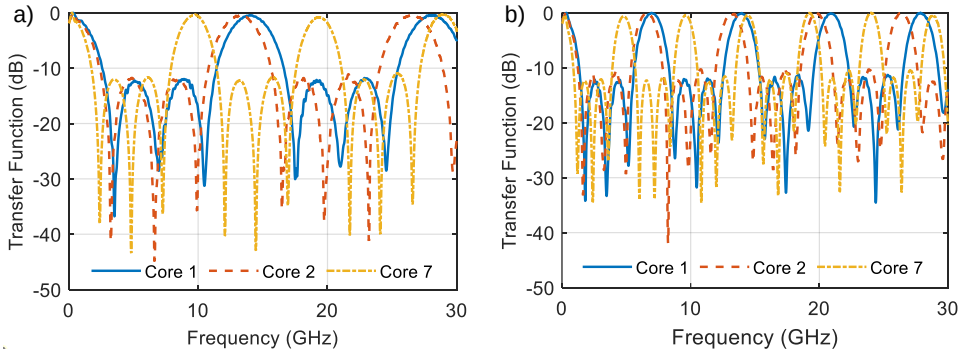

Fig. 4.3. Measured 4-tap RF signal filtering responses of cores 1, 2 and 7 when the TTDL is operated on the wavelength-diversity domain for two different carrier separations (a) 1 nm and (b) 2 nm.

4.3. Optical beamforming for phased array antennas

4.3.1. Introduction

For several years, optical beamforming for phased-array antennas has been a topic of research primarily for radar and electronic warfare purposes, but with rising importance for civilian communications and radio astronomy applications [13], [105]. A phased array antenna comprises an array of radiating elements that are fed coherently with different phase shifts, thus allowing the variation of the radiation pattern's beam-pointing direction at will [106]. The difficulty of electronically feeding thousands of elements and the narrowband operation of electronic phase shifters have prevented the utilization of large arrays [107]. Moreover, a phenomenon called beam squinting is produced when a broadband signal is applied to an electronic phased array as every frequency component experiences a different phase shift [13], [107]. Wideband operation is obtained when the phase shifter is replaced by an optical delay line (i.e., true-time delay line). Different technologies have been proposed for the implementation of optical true-time beamforming, including fiber-based architectures that comprise dispersive fibers [108], [109], fiber Bragg gratings [110] or parallel SMFs [111], as well as photonic integrated solutions [112].

Optical beamforming follows discrete-time signal processing schemes in the same way as MWP signal filtering, with the difference that the *N*-delayed samples are detected individually. Each of the *N* radiating elements that comprise the phased array antenna is fed by one of the *N* RF output signals. In the case of 1D architectures, the normalized angular far-field pattern of the radiated electric field, or antenna array factor *AF(θ)*, is given by the angular Fourier transform of the overall spatial electric field distribution at the output of the radiation elements [106]:

$$AF(\theta) = \frac{1}{N}\sum_{n=0}^{N-1} a_n e^{-j2\pi f_{RF} n\left(\Delta\tau - d\sin(\theta)/c\right)}, \tag{4.2}$$

where θ is the far field angular coordinate, N the number of samples, a_n the complex coefficient of sample n, $\Delta\tau$ the differential group delay between adjacent samples, f_{RF} the RF frequency of the modulated signal, d the spacing between radiating elements and c the light speed in the vacuum. From Eq. (4.2), we see that the angle for maximum radiating energy θ_0 occurs when $\Delta\tau = d\sin(\theta_0)/c$. This beam-pointing angle θ_0 can be tuned by changing the differential group delay between adjacent samples. The phase difference between elements is then given by $\Delta\phi = 360^\circ \cdot f_{RF} \cdot \Delta\tau$. To scan the whole sector in front of the antenna, the beamforming network must provide a $\Delta\phi$ ranging from 90º to –90º. Table 4.1 gathers the phase difference caused by 1-ps delay change and the delay that is required to scan the whole area in front of the antenna. High-frequency signals, thus, demand a more stable behavior than low-frequency ones.

Table 4.1. Impact of delay variation on the phase difference between antenna elements and the required delay to steer the beam in the whole area in front of the antenna at different RF frequency signals.

RF frequency (GHz)	1	10	26
RF phase difference per 1-ps delay change (°/ ps)	0.36	3.60	9.36
Required delay to scan from π to $-\pi$ (ps)	1000.00	100.00	38.46

Differing to the MWP filtering application, here each sample is detected individually and feed a different radiating element of the antenna. Either the space diversity or the wavelength diversity can be used to generate signal samples. However, the space diversity approach has the advantage of offering continuous delay tunability without any additional demultiplexing element. The latter is required in the wavelength diversity approach to demultiplex the wavelength-multiplexed samples. Therefore, we use the heterogeneous 7-core MCF TTDL in the spatial-diversity domain to act as an optical beamformer for an actual phased array antenna (PAA) that was designed and fabricated at iTEAM's facilities by the Antennas & Propagation Lab group. We measured the radiation pattern of the PAA in an anechoic chamber located in the same laboratory as well.

4.3.2. Experimental demonstration of 1D optical beamforming

Fig. 4.4 represents the experimental setup to measure the radiation pattern of the PAA. The optical signal coming from a tunable laser is modulated using a dual-drive EOM with the RF signal generated by a VNA. This signal is then amplified using an EDFA and launched into cores 3 to 7 of the MCF. VOAs are used in each core path to obtain uniform power distribution. The signal from each core is detected and amplified using independent photodiodes and RF amplifiers. The PAA along with the required optical and electrical devices were placed inside the anechoic chamber onto an antenna positioner. A horn antenna receives the signal radiated by the PAA, and this signal is then amplified by a low-noise amplifier (LNA). The power of this signal is measured at the VNA.

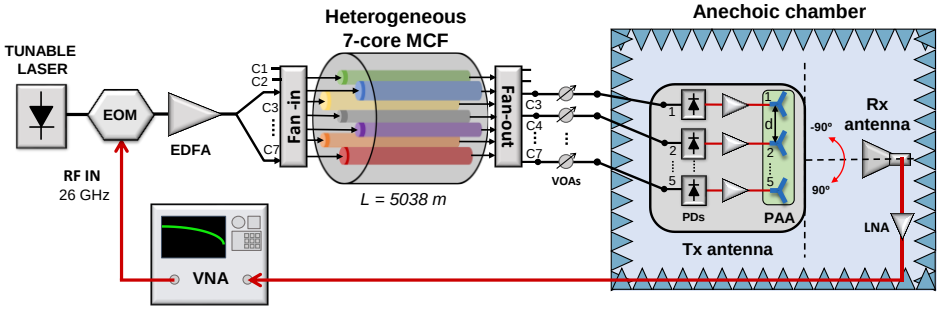

Fig. 4.4. Experimental setup of the optical beamforming network for the fabricated PAA along with the radiation pattern measurement infrastructure. EOM: electro-optic modulator. EDFA: Erbium-doped fiber amplifier. VNA: vector network analyzer. VOA: variable optical attenuator. PD: photodetector. PAA: phased array antenna. LNA: low-noise amplifier.

The PAA has eight radiating elements with an element spacing of d = 5.77 mm (0.5λ_0 at 26 GHz), ensuring single-lobe operation [106]. Because of the large electrical size of available RF connectors at this band, an extension of the input lines ending at a stepped substrate outline was conceived to accommodate the connectors. Microstrip lines were properly shaped to ensure identical time delays from each input to its corresponding radiating element. Fig. 4.5(a) shows a 3D representation of the radiation pattern at 26 GHz over the PAA, when all inputs are fed with a uniform amplitude and phase. As expected, a directive radiation pattern along the array axis is achieved, with a small ripple due to the finite dielectric. Fig. 4.5 (b) shows a picture of the fabricated antenna. The antenna was fabricated using a milling machine on a substrate Rogers RT5880 with a height of 0.381 mm and relative permittivity of 2.2. Fig. 4.5(c) represents the active *S*-parameters as a function of the RF frequency measured with a VNA. We can observe that signal reflection keeps mostly below the accepted threshold of -10 dB within the measured band. Finally, the far-field radiation pattern of a single element has been measured in the anechoic chamber at 26 GHz. Fig. 4.5(d) compares the measured embedded radiation pattern of one representative antenna element with the simulated one, where the typical rippled response along the non-directive plane is observed, with a -6-dB beamwidth of around 120º.

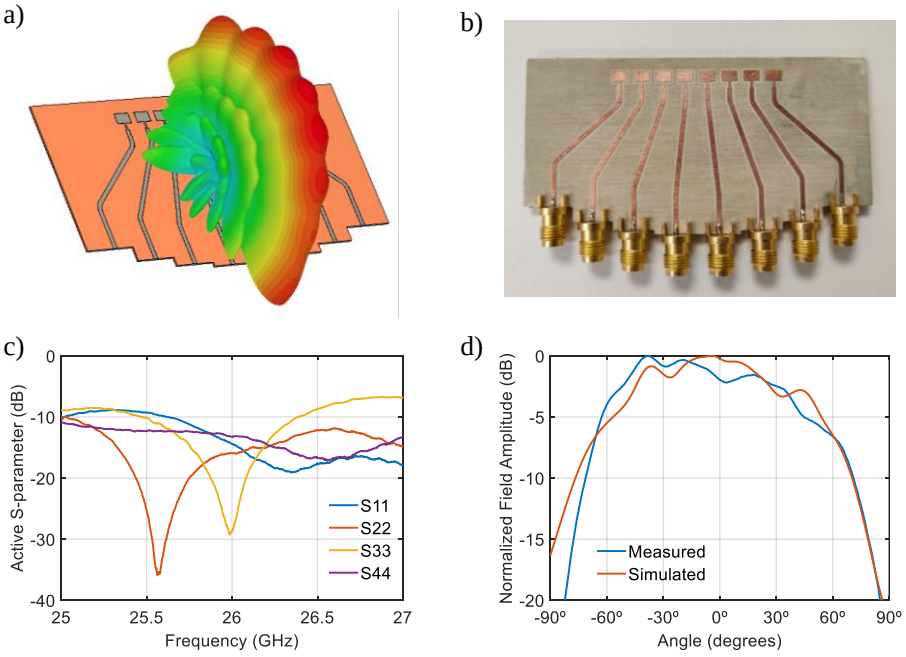

Fig. 4.5. (a) 3D representation of the PAA radiation pattern, (b) photograph of the PAA with the RF connectors, (c) measured active *S*-parameters as a function of the radiofrequency and (d) measured radiation pattern for a single antenna element compared with the simulated one.

Figure 4.6 shows the inside of the anechoic chamber, where we can appreciate in the left photograph the front side of the transmitter antenna and in the right photograph the receiver antenna, where the separation between both antennas is also indicated (3 m). The transmitter antenna (i.e., the PAA) is held in a positioner that allows a 180-degree azimuth rotation for the proper measurement of the radiation pattern. We must note that the MCF spool was placed outside the anechoic chamber because of the limited space inside the chamber. Five 10-m long SMF pigtails deliver the optical signals from the MCF output to photodetectors inside the chamber. As we can see in the photograph on the left, each output fiber is connected to an independent photodetector and RF amplifier. These elements were placed together on the antenna positioner, and feed the corresponding PAA elements by means of 1-meter RF cables. A total of 4 three-channel power supply sources feed the photodetector and amplification stage.

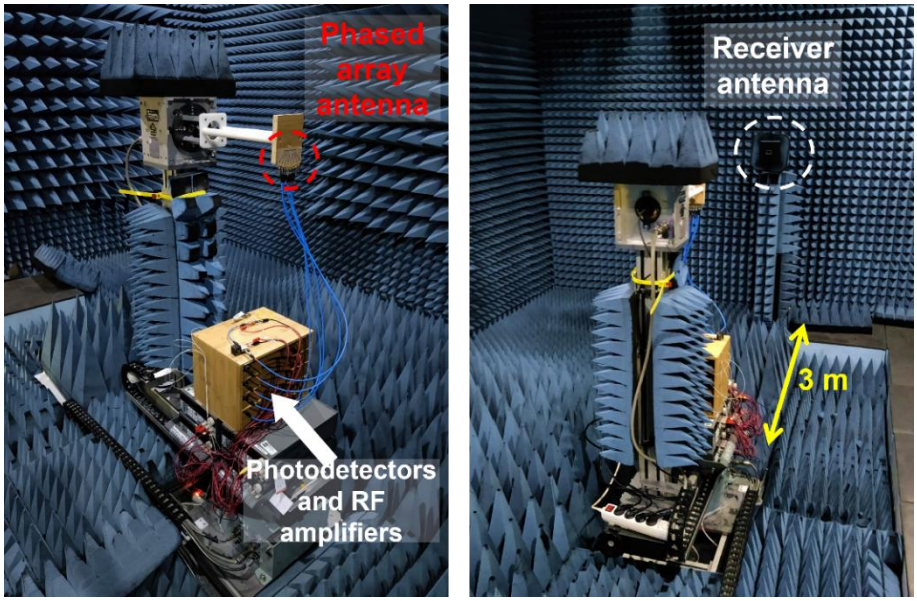

Fig. 4.6. Photographs of the inside of the anechoic chamber with identification of both antennas along with main devices at the transmitter side.

Beam steering in the optical beamforming network is achieved by sweeping the operation optical wavelength. Fig. 4.7(a) illustrates the evolution of the beam-pointing angle as a function of the optical wavelength. Different optical wavelength bands can be chosen to produce a beam steering of 180º in the typical EDFA optical wavelength range (i.e., 1530 – 1560 nm). As the single-element radiation pattern of Fig. 4.5(d) shows, for absolute angles greater than 45º, the received power drops considerably, which limits the maximum beamforming angle we can achieve. Thus, we choose the optical wavelength band ranging from 1542.50 up to 1548.28 nm, which produces the desired range of beam-pointing angles. We then measured the radiation pattern at different optical wavelengths ranging from 1542.50 to 1548.28 nm in steps of 0.96 nm. This translates into time delays provided by the TTDL going from 62.5 to 91.36 ps in steps of approximately 4.81 ps.

Figure 4.7(b) depicts the measured radiation pattern for the 7 different optical wavelengths. The resulting beam-pointing angle varies approximately from -43º up to 40º. Minor discrepancies in the basic differential delay between cores affect the radiation pattern, causing the main lobe to broaden at angles farther from the broadside direction and shifting the beam pointing angle slightly. The radiation pattern of the antenna elements also contributes to this phenomenon as it has substantial power variations, affecting the main lobe shape. In addition, slight mismatches between the theoretical and experimental beam-pointing direction for angles farther than the broadside can also be attributed to the antenna itself due to the higher attenuation for those angles, as the single element radiation pattern shows (black dashed line in Fig. 4.7(b)).

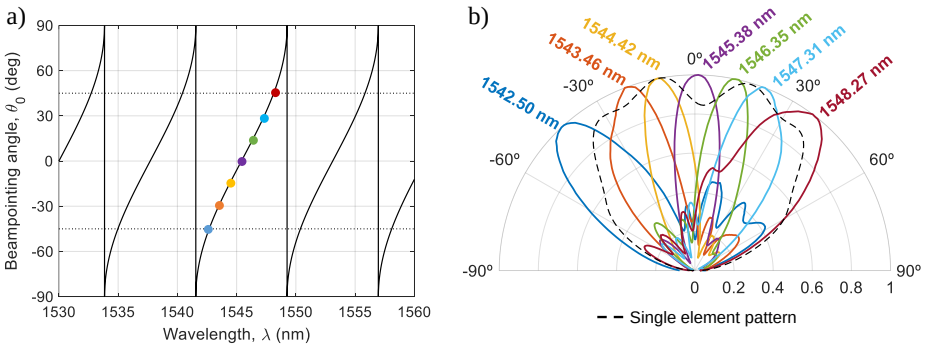

Fig. 4.7. (a) Simulation of the beam-pointing angle (in degrees) as a function of the optical wavelength. Filled circles indicate the chosen wavelengths for the experiment. (b) Measured radiation patterns of the whole PAA at different wavelengths (colored solid lines) together with that of a single radiating element of the PAA (black dashed line).

4.4. Arbitrary Waveform Generation (AWG)

4.4.1. Introduction to AWG and UWB

The generation of arbitrary RF waveforms is of great interest in applications such as radar systems, wireless communications and remote sensing [13], [113], [114]. Because of bandwidth limitations of electronic arbitrary waveform generation (AWG), photonic techniques have been attracting major attention due to their broadband nature, fiber distribution compatibility, reconfigurability, immunity to EMI, along with smaller size and weight [115]. A different number of fiber-based techniques have been demonstrated for optical AWG, such as frequency-to-time mapping [116], [117], phase-modulation-to-intensity-modulation conversion [118], and microwave signal filtering [119], [120].

Ultra-wideband (UWB) communications attract considerable interest for short-range high-throughput wireless communications and sensor networks due to their intrinsic properties. Compared to traditional narrow-band wireless systems, UWB brings immunity to multipath fading, short temporal duration, carrier-free transmission, low power consumption, wide bandwidth and low power spectral density [118]. However, due to their low power density, UWB systems can only operate within a few meters

range and are restricted mainly to indoor scenarios. Distribution over fiber (i.e., UWB-over-fiber) could extend the area of coverage of UWB systems, thus bringing the aforementioned advantages to current communications networks. We can distinguish two types of UWB communication systems: impulse radio and multi-band. The first type is generally preferred as it is carrier free (no frequency down-conversion). The selection of a given impulse type determines the performance of the system [118]. Gaussian pulses are the simplest waveforms that can be employed for UWB communications. However, more complex waveforms like higher-order derivatives of a Gaussian pulse (monocycle, doublet, triplet, etc.) and some other waveforms are highly desired because they are more power efficient and can be adapted to meet power spectral density regulations [119], [120].

Following, we demonstrate tunable optical arbitrary waveform generation implemented with the 7-core heterogenous MCF. We synthesize a variety of UWB pulses following a reconfigurable microwave photonic approach where the number of taps varies from 2 to 7 according to the number of cores exploited.

4.4.2. Experimental demonstration of Ultra-wideband Pulse Generation

Figure 4.8 shows the experimental setup implemented for the proposed AWG system. Its basic principle of operation consists of the propagation of an RF-modulated temporal pulse along the fiber cores to obtain 7 time-delayed replicas of the original pulse, therefore, it is based on exploiting the spatial-diversity regime of the fiber. Then, a set of VOAs controls the sample amplitudes, and a switching matrix sends each core output to the desired branch of the balanced photodetector to obtain both positive and negative samples. This provides positive and negative coefficients which in turn determine the shape of the generated waveform. Here we observe that the addition of an optical phase shifter to each tap can increase the flexibility of the generated waveform as the tap weight would become complex. This, however, would also increase the complexity of the setup by introducing up to 7 different optical components that need to be tuned manually and possibly introduce additional delays. We use an RF pulse generator with a 12.5-Gb/s bit rate to create an 80-ps temporal width pulse with a 5 ns repetition interval. A filtered BS is used as the optical carrier to avoid optical coherence in photodetection. Here we adjusted the optical filter bandwidth to 1 nm to increase the optical power at the photodetector (i.e., to improve signal-to-noise ratio (SNR)). After propagation, the electrical response of the generated waveform is measured at the output of the balanced PD in both time and frequency domains by using a digital phosphor oscilloscope (DPO) and a VNA, respectively. The measured temporal and frequency domain representations of the input and output signal when a signal sample is sent to the positive branch of the PD are depicted at the bottom of Fig. 4.8.

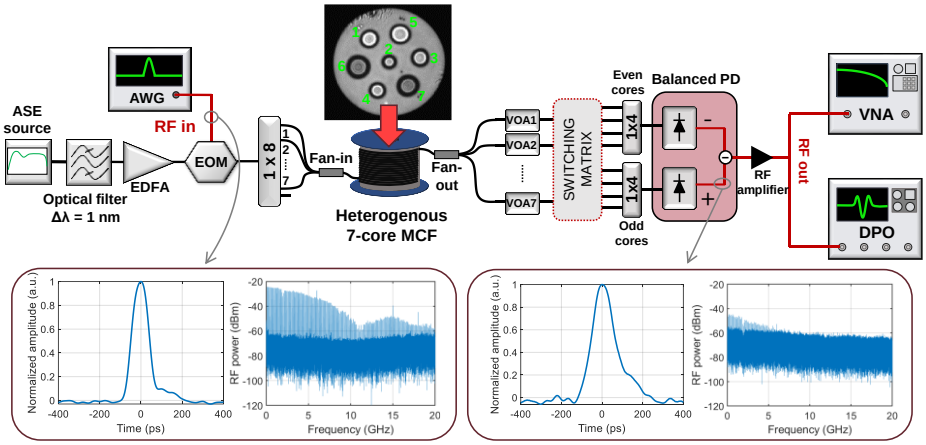

Fig. 4.8. Experimental setup for AWG based on a dispersion-diversity multicore fiber. PD: photodetector. EDFA: Erbium-doped fiber amplifier. EOM: electro-optic modulator. VOA: variable optical attenuator. BS: broadband source. VNA: vector network analyzer. DPO: digital phosphor oscilloscope.

Figure 4.9 gathers the measurement of different synthesized waveforms by choosing the appropriate combination of cores with a given tap weight at the optical wavelength of 1550 nm compared with the simulated ones. Fig. 4.9(a) and (b) represent a monocycle waveform (2 samples) with different polarities. The polarity of a given waveform can be inverted simply by changing the path of each core in the switching matrix. Fig. 4.9(c)-(f) show, respectively, the resulting waveforms for doublet (3-sample), triplet (4-sample), quadruplet (5-sample) and 7-sample combinations. The tap weights for each case are listed in Fig. 4.9 caption. The generated waveforms are in good agreement with the expected results, with slight mismatches that can be attributed to either the nonsymmetrical waveform of the input RF pulse or noise introduced by the BS. In the first case, and as we can see in Fig. 4.8, the baseband pulse presents a non-negligible tail at the right-hand side of its amplitude that can invade the temporal slot of the following samples and alter their amplitude and shape. This phenomenon especially affects higher-order waveforms where the pulses from several cores are combined. In the second place, the inevitable noisy response of the filtered BS (see the floor noise level on the pulse RF spectrums of Fig. 4.8) produces non-negligible power fluctuations that can affect the shape of the waveforms, especially those containing taps with low amplitudes. The combination of both effects can be clearly appreciated in the 7-sample waveform, where there are amplitude fluctuations at the beginning and end of the waveform.

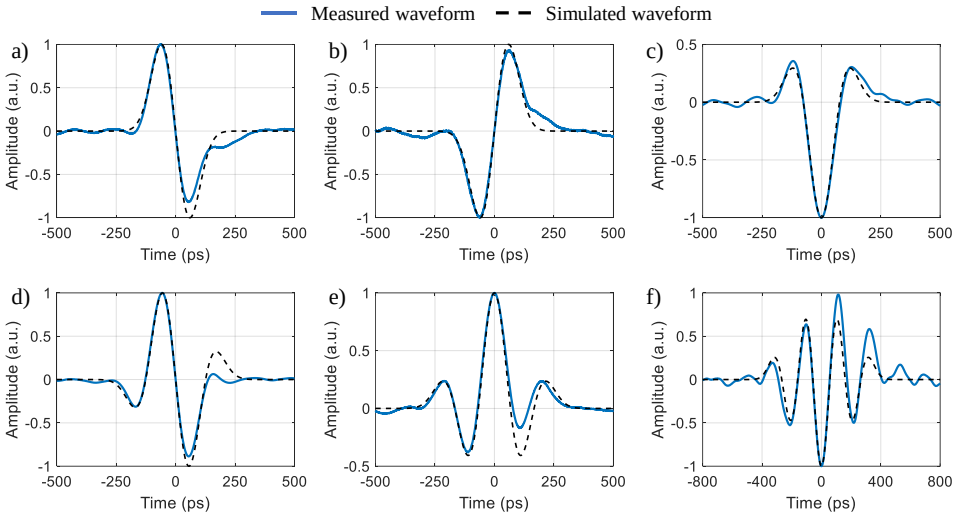

Fig. 4.9. (a) Monocycle waveform with weights [1, -1], (b) monocycle waveform with weights [-1, 1], (c) doublet waveform with weights [0.5, -1, 0.5], (d) triplet waveform with weights [-0.35, 1, -1, 0.35], (e) quadruplet waveform with weights [0.25, -0.5, 1, -0.5, 0.25] and (f) 7-sample waveform with weights [0.25, -0.5, 0.75, -1, 0.75, -0.5, 0.25].

One of the main advantages of this architecture relies on the tunability of the TTDL, which provides the capability to continuously tune the temporal pulse separation with the optical wavelength. This waveform tunability is useful for a system that needs to adapt to different regulations or to change the temporal and spectral properties of the generated waveform dynamically. Fig. 4.10(a) shows the measured waveforms of a monocycle at the optical wavelengths of 1550, 1555 and 1560 nm, which correspond to a pulse separation of 100, 125 and 150 ps, respectively. Fig. 4.10(b) represents the measured spectra along with the representation of the ideal 2-sample RF filter (black dashed line) for the previous waveforms, where we see how the interference pattern is adequately generated for the abovementioned time delays. As a second example, Fig. 4.10(c) and (d) represent, respectively, the measured temporal waveforms and RF spectra for the quadruplet configuration at the optical wavelengths of 1550, 1555 and 1560 nm. We see, again, satisfactory waveform tunability, although in this case both the temporal waveforms and their spectra experience some distortion due to amplitude mixing with adjacent samples and noise since we have increased the number of samples (as discussed in the previous paragraph).

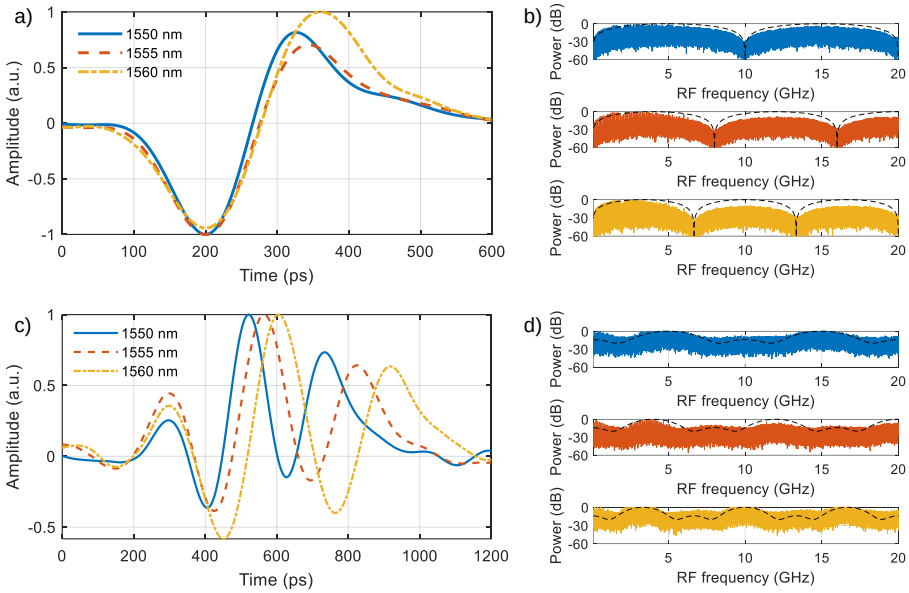

Fig. 4.10. Monocycle waveforms generated at different optical wavelengths (a) and their respective electrical spectrum (b). Five-sample waveforms generated at different optical wavelengths (c) and their respective electrical spectrum (d).

4.5. 5G signal transmission

4.5.1. Introduction

The introduction of the fifth-generation mobile networks has expanded the use cases and applications for mobile communications, ranging for instance from ultrahigh definition video, autonomous driving to virtual/augmented reality. Current sub-6 GHz bands cannot provide the required data rate, for that reason, mobile networks are transitioning to higher frequency bands, like the millimeter wave band [15], [16]. Unfortunately, the area of coverage decreases drastically at those frequencies which in turn requires the introduction of smaller cells. An enormous number of cells is then required to cover the same area and that increases the complexity of the radio access network. Then, MCFs are proposed to extent the capacity of the fronthaul network and add another degree of freedom for multiplexing, slicing or routing [7]. Here, MCFs provide better performance in terms of inter-core crosstalk and SNR, in uplink/downlink signaling, compared to other multiplexing technologies such as optical circulators or WDM.

Then, we consider the scenario in which the heterogeneous 7-core TTDL MCF is deployed, for instance, between a central office and a remote antenna unit. This fiber was designed for distributed microwave signal processing applications, but it can also be used to carry traditional data signals in cores and/or optical wavelengths not in use for TTDL operation. The primary concern is that inter-core crosstalk does not interfere with the transmitted signals. For that reason, we evaluate the possibility of distributing high-frequency 5G new radio signals with this fiber.

4.5.2. Experimental demonstration

Figure 4.11 represents the setup used to transmit 5G signals through the heterogeneous 7-core MCF. A laser source generates an optical carrier at 1550 nm, which is then modulated by a 26-GHz 5G New Radio signal generated with a Vector Signal Generator (VSG). The resulting signal is then amplified via an EDFA to compensate for the loss introduced by the different components (modulator, coupler and fan-in/fan-out devices) and fiber propagation losses. At this point, VOAs are used to control the optical power in each core. The signal is then coupled to the different cores of the fiber through the fan-in device. After propagation, a fan-out device extracts the optical signal from all cores. The signal from one of the cores is connected to the photodetector at a time, and then analyzed by the Signal and Spectrum Analyzer (SSA). Different parameters of the 5G signal can be tuned as well, such as the modulation (QPSK, 16QAM, 64QAM and 256QAM), subcarrier spacing, cyclic prefix, number of subcarriers (bandwidth) and sequence length. The SSA demodulates the 5G signal and obtains signal statistics for a different number of parameters including error vector magnitude (EVM), RF power, frequency error, etc. It also represents the demodulated signal in the form of in-phase/quadrature (IQ) diagrams and RF spectrum.

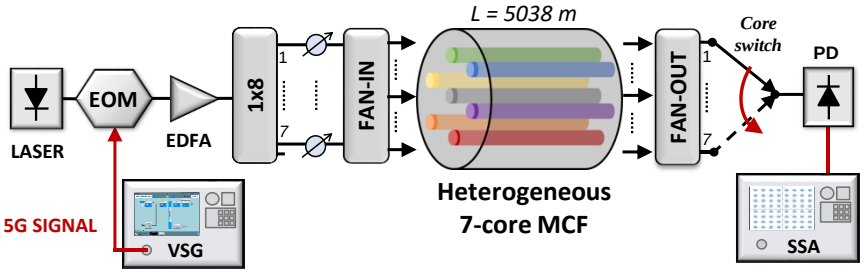

Fig. 4.11. Experimental setup where 5G signals are transmitted through the 7-core heterogeneous MCF. VSG: Vector Signal Generator. SSA: Signal and Spectrum Analyzer. PD: photodetector. EDFA: Erbium-doped fiber amplifier. EOM: Electro-optic modulator.

The EVM is a measure of the error between received symbols and ideal symbols and can be utilized as a signal quality indicator. As a representative case, Fig. 4.12 shows the EVM results obtained for core 2 when delivering a 256QAM 200-MHz signal. The received optical signal is varied by tuning the VOA of that path. We represent as well the RF power measured by the SSA. As we observe, the EVM depends linearly on the received power as the SNR increases.

Table 4.2 gathers the measured EVM when the 5G signal is generated with a different modulation. The first row represents the case when the VSG is connected directly to the SSA and the second row when the same signal is transmitted through the central core (#2). The results show that the error depends mainly on the received power. The limit EVM from the 3GPP standard specification [121] is displayed in Table 4.2 for comparison.

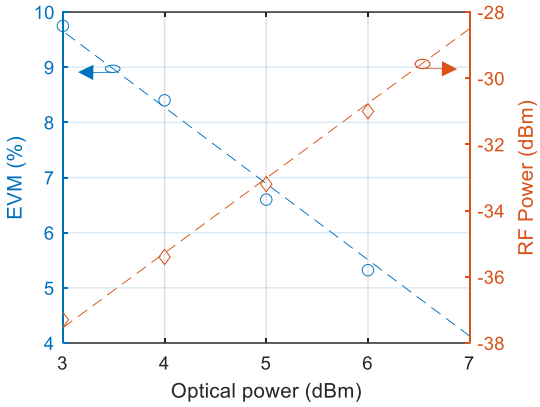

Fig. 4.12. Measured EVM dependence with the optical power (blue markers). The RF power detected in each case is also represented (orange markers). A linear fit of the results is plotted for clarity in each case.

Table 4.2. Measured and 3GPP required EVM for different modulation options and transmission through the central core.

Modulation	QPSK	16QAM	64QAM	256QAM
EVM (b2b) (%)	1.01	1.05	1.06	1.02
EVM (after propagation through core 2) (%)	2.32	2.36	2.56	2.35
Required EVM [121] (%)	18.50	13.50	9.00	4.50

Figure 4.13 represents the IQ diagram of the 64QAM signal, where we can see that the diagram is undistorted when we use only core 2 (a), while is distorted when all the cores are lightened up (b). We observe that inter-core crosstalk introduces distortion on higher-amplitude symbols, which degrades the SNR for those symbols in particular.

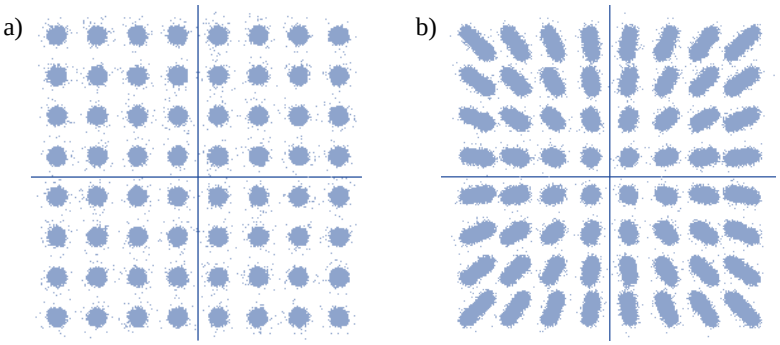

Fig. 4.13. IQ diagram of a 64QAM-modulated 5G NR signal after propagating through core 2 when the other cores are not used (a) and when they carry a signal with similar power (b).

Then we investigated the maximum capacity this fiber can support in terms of both bandwidth and modulation. For that reason, the 5G signal was configured with a different modulation and RF bandwidth. In each measurement, the same optical signal was propagated through all the fiber cores, but only one core is analyzed at each time. We adjusted the optical power level before the photodetector to be nearly the same for each core, so we can study the effect of crosstalk properly.

Figure 4.14 represents the average EVM obtained at each core (circle markers) for the combination of two different bandwidths (200 and 400 MHz) and modulations (64QAM and 256QAM). EVM metrics are obtained after analyzing 100 frames for each core. The error bar indicates the maximum and minimum EVM values obtained during the measurement period. Red dashed line (or a red arrow) indicates the maximum EVM for each modulation. As we see in Fig. 4.14(a) and (c), the EVM is below the error limit for the 64QAM modulation in every core (< 9%). For the 256QAM modulation, the EVM in the outer core is below the limit in the 200-MHz case (Fig. 4.14(b)). In the 400-MHz case (Fig. 4.14(d)), the EVM limit is crossed in every core. Therefore, we perceive that a higher signal bandwidth is more sensitive to detrimental effects in the fiber. The EVM for the central core (core 2) hits a maximum of 7.8% for the 400-MHz-256QAM case (Fig. 4.14(d)). Core 2 has the highest average EVM in all cases and also the highest variation. Cores 1, 3 and 4 also present some fluctuations though they are less significant. The rest of the cores, cores 5-7, show negligible EVM fluctuations, as their inter-core crosstalk level is the lowest. Therefore, we conclude that inter-core crosstalk variations with time directly influence the EVM [122].

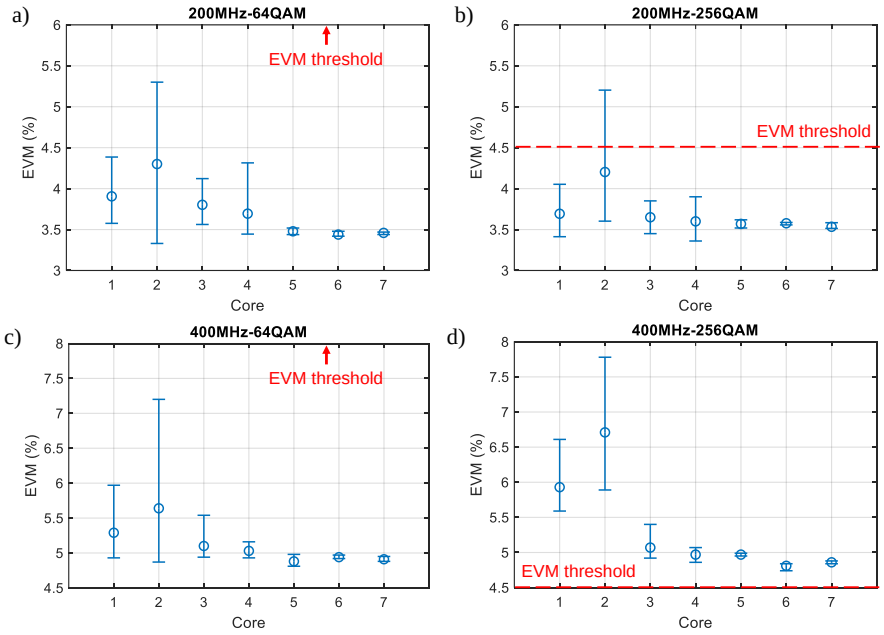

Fig. 4.14. EVM results per core for a 5G signal with the following bandwidth-modulation pair values: (a) 200 MHz-64QAM, (b) 200 MHz-256QAM, (c) 400 MHz-64QAM, and (d) 400 MHz-256QAM.

4.6. Conclusions

We have successfully demonstrated several tunable distributed signal processing functionalities built upon a dispersion-diversity heterogeneous 7-core MCF. First, we evaluate tunable signal filtering capabilities by exploiting the space and wavelength diversities of the fiber. In the first case, the FSR of the implemented 5-tap filter was tuned from 6.7 up to 20.0 GHz by varying the optical wavelength from 1540 up to 1560 nm. This corresponds to a delay variation from 50 up to 150 ps. In the second case, a 4-tap filter was implemented in each core. The carrier separation was 1 nm and 2 nm, which provides an FSR variation from 14.0 down to 9.8 GHz and from 7.0 down to 4.8 GHz, respectively. Then, we realized optical beamforming for PAA by utilizing cores 3-7 in a high-frequency antenna fabricated in purpose for this experiment. The radiation pattern was steered from -40º to 43º by tuning the optical wavelengths from 1542.50 to 1548.28 nm. Lastly, optical arbitrary waveform generation was demonstrated by implementing a balanced differential photodetection setup in the space-diversity domain of the fiber. Up to 7-tap UWB pulses were shaped using a different combination of cores in each case. The optical wavelength was tuned to change the shape of the waveforms.

In addition, we also proved that 5G signals can be transmitted with negligible effects over most of the cores. The results show signal bandwidth is the main factor in determining the error introduced by the propagation through this fiber for the same received electric power. Cores with high crosstalk, especially 1 and 2, present higher error levels than the rest of the cores. In particular, this may limit maximum-order modulation in the case of the central core (core 2).

Chapter 5
Heterogeneous 19-core MCF-based TTDL

5.1. Introduction

This chapter describes the complete design and fabrication of a dispersion-engineered heterogeneous 19-core MCF that behaves as a tunable sampled TTDL. In this design, we employ three different fiber preforms that are scaled down to realize all the cores. This is done primarily to reduce the costs of fabricating a dispersion-diversity fiber with a high number of cores. To obtain the span of necessary chromatic dispersions, each preform has a unique refractive index profile, including a trench-assisted step-index, a ring-assisted graded-index, or a trench-assisted triangular-index structure.

The final design is accomplished after adjusting a preliminary design with the data extracted during the characterization of the core preforms fabricated for it. It can provide simultaneously 15 samples in the spatial diversity regime with 4 additional backup samples. The chromatic dispersion ranges from 7.5 to 21.5 ps/km/nm at 1550 nm. The fiber was fabricated in collaboration with Dr. Michael Frosz at the Max Planck Institute for the Science of Light (MPL) in Erlangen (Germany). I was able to assist in the fabrication of the fiber during my stay there. At the time of writing, the fiber has been evaluated initially and a couple of fan-in/fan-out devices have been fabricated by the company *Chiral Photonics* for this specific fiber.

Achieving a TTDL with more samples in the spatial diversity domain would improve the properties of the implemented functionalities, which depend crucially on the number of time-delayed samples. As such, a TTDL with more samples could provide, for instance, a narrower and more concentrated beam in the optical beamforming for phased-array antennas functionality, as well as enable multiple functionalities to be built over the same fiber link.

5.2. Preliminary design

As a starting point, we consider a heterogeneous MCF design with 19 cores that acts as a tunable TTDL. Accordingly, each core must have specific propagation characteristics in terms of chromatic dispersion and group delay. The designed MCF must also have a low inter-core crosstalk, including the corresponding crosstalk sensitivity against fiber curvatures in heterogeneous MCFs. In addition, the design must meet two more goals: reduced fabrication cost and resilience against fabrication errors. First, regarding fabrication cost, we observe that fabricating 19 different preforms, as in the case of the 7-core MCF from the previous chapters, is not feasible because the cost would probably scale linearly with the number of cores. For that reason, we employ a preform-scaling technique where the different cores are obtained by scaling down the preform with a different ratio (i.e., the scaling factor). This allows to obtain the particular chromatic dispersion values that we need for TTDL operation.

Second, the design must be resistant against small core dopant concentration and radius deviations produced during fiber manufacturing (due to fabrication tolerances). Here, we must note that this is related to the number of cores N and the range of chromatic dispersions that can be obtained for a given core refractive index profile. As cores must have a given dispersion difference (ΔD) for TTDL operation, we observe a large ΔD diminishes N but increases fabrication reliability, and vice versa. In line with previously fabricated MCF-based TTDLs, we aim at a dispersion difference ΔD of at least 1 ps/km/nm in this design. However, as step-index profiles are limited to a 14-20 ps/km/nm D range, to achieve such ΔD we need to look for other types of refractive index profiles that can expand the range of chromatic dispersions. In that sense, the selection of a particular refractive index profile has a direct impact on the chromatic dispersion [123]. Therefore, we consider three different preforms, each with a trench-assisted step-index (TA-SI), a ring-assisted graded-index (RA-GI) and a trench-assisted triangular-index (TA-TI) refractive index profiles (represented in Fig. 5.1(a, c, e)). Moreover, to enhance the resilience against fabrication inaccuracies, the largest cores in the second and third preforms are designed with the same chromatic dispersion as the smallest ones in the first and second preforms.

Figure 5.1(b, d, f) represents the filled contour plot of the chromatic dispersion change per scale factor variation (dD/d$Factor$) as a function of core radius a_1 and GeO_2 core dopant proportion for the three different refractive index profiles considered. Layer proportions are equal in the three cases such that $a_3 = a_2 = a_1$. We use *Photon Design Fimmwave* software to solve the modes of the core structure and to calculate the required optical propagation characteristics (D, n_{eff}, n_g, etc.). Dash-dotted lines are the contour surfaces enclosing the different dispersion values that can be reached. We see that the core radius and dopant concentration parameters have significant impact on the chromatic dispersion (especially the core radius a_1). The dD/d$Factor$ represents the derivative of the chromatic dispersion with the scaling factor; more specifically, it represents the variation on the chromatic dispersion for an equivalent scaling factor change of 0.1 μm in the core radius. We appreciate here that the core size relates to the variability during the fabrication process as small core

radius variations affect more the smaller cores than the larger ones. The different refractive index profiles provide the required chromatic dispersions where the d*D*/d*Factor* is minimized. From Fig. 5.1(b, d, e) we also see that choosing the adequate dopant concentration in the core establishes the radius difference that must be accomplished to obtain cores with a different dispersion.

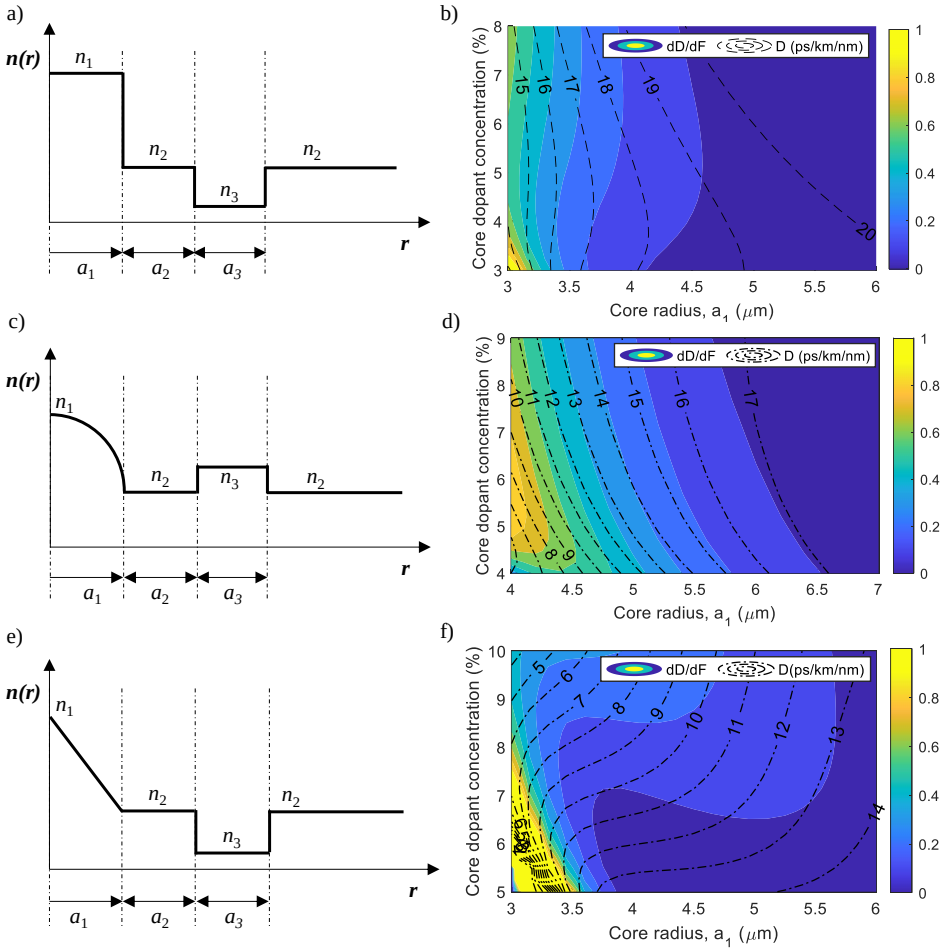

Fig. 5.1. (a, c, e) Refractive index profile of the considered preforms, (a: TA-SI, c: RA-GI, e: TA-TI). a_1: core radius; a_2: inner cladding radius; a_3: trench width, n: refractive index of each layer (core, cladding, trench/ring). (b, d, f) Chromatic dispersion variability contour plot as a function of core radius a_1 and core dopant (right) for the different types of refractive index profiles (b: TA-SI, d: RA-GI, f: TA-TI). Core layer parameters in each case: $a_3 = a_2 = a_1$. Where the trench layer is 1% F-doped and 1% GeO_2-doped in the case of the ring.

A drawback of the scaling preform technique is that we only control one design parameter, the scaling factor. Because of this, we can only fulfill the chromatic dispersion parameter requirements. We can, however, minimize the group index at λ_0 and the dispersion slope by choosing the appropriate core parameters in each preform. The rest of the structural parameters (a_2, a_3 and n_3) are optimized to reduce dispersion

variability during fabrication. Table 5.1 gathers the core design parameters of the preforms considered. These preforms are then scaled with different ratios to obtain the corresponding individual cores of the MCF. Fig. 5.2 represents the simulated chromatic dispersion at 1530 nm as a function of the scaling factor for each preform and for a base core radius a_1 = 3 μm. We see here the previously stated consideration on the core overlapping between preforms, where the first core of preform 2 has the same dispersion as the last one from preform 1, likewise for the last two cores of preform 2 and the first two cores of preform 3. From that, we select a set of cores that satisfy a dispersion difference ΔD = 1 ps/km/nm. As indicated in Fig. 5.2, cores 1-5, 6-12 and 13-19 come from TA-SI, RA-GI and TA-TI preforms, respectively.

Table 5.1. Design parameters of the different preforms considered in this design.

Preform	a_2/a_1	a_3/a_1	n_1 dopant (GeO_2 mol. %)	n_3 dopant
TA-SI	0.62	0.87	4.70	1.00% F
RA-GI	0.28	0.31	5.20	2.60% GeO_2
TA-TI	1.36	0.39	7.50	1.00% F

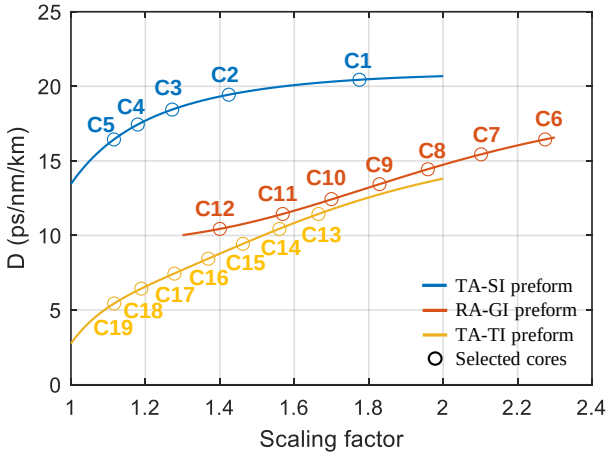

Fig. 5.2. Simulated chromatic dispersion D (at 1530 nm) dependence on the scaling factor of the different preforms in this design. A base core radius of a_1 = 3 μm is considered. The selected cores for the design are indicated in each case.

Table 5.2 lists the main design parameters and optical properties of each core. This fiber design provides a range of chromatic dispersion from 20.44 to 5.44 ps/km/nm at 1530 nm with a dispersion difference ΔD = 1 ps/km/nm. We observe some cores have the same chromatic dispersion, i.e., the smallest cores in the first and second preform (cores 5, 11 and 12) have an overlapping counterpart in the following preform (cores 6, 13 and 14). This safeguards TTDL functionality in case the smallest cores in the first and second preform are impacted by fabrication errors, which, as we see in Fig. 5.1, have more probability of dispersion variations during fabrication.

Keeping the same Δ*D* between cores of different preforms is critical for spatial diversity operation, since a small deviation there could divide the whole TTDL into three different ones. As a result, 16 out of the 19 cores can be used simultaneously for spatial diversity operation.

Table 5.2. Design parameters and optical propagation properties (at λ_0 = 1530 nm) of each core in the preliminary design. Color coding indicates cores with an overlapping counterpart sample.

Core	*Preform*	a_1 (μm)	a_2 (μm)	a_3 (μm)	n_1 *dopant*	n_3 *dopant*	*D* (ps/km /nm)	*S* (ps/km /nm^2)	n_{eff}
1	TA-SI	5.33	3.30	4.63	4.7% GeO_2	1% F	20.44	0.065	1.4490
2		4.27	2.65	3.72			19.44	0.063	1.4481
3		3.82	2.37	3.32			18.44	0.061	1.4476
4		3.54	2.19	3.08			17.44	0.059	1.4472
5		3.35	2.08	2.91			16.44	0.056	1.4469
6	RA-GI	6.82	1.91	2.12	5.2% GeO_2	2.6% GeO_2	16.44	0.062	1.4486
7		6.31	1.77	1.96			15.44	0.061	1.4483
8		5.88	1.65	1.82			14.44	0.061	1.4481
9		5.49	1.54	1.70			13.44	0.062	1.4478
10		5.11	1.43	1.58			12.44	0.064	1.4476
11		4.71	1.32	1.46			11.44	0.066	1.4473
12		4.20	1.18	1.30			10.44	0.069	1.4469
13	TA-TI	5.00	6.79	1.97	7.5% GeO_2	1% F	11.44	0.064	1.4475
14		4.68	6.36	1.84			10.44	0.064	1.4472
15		4.39	5.97	1.73			9.44	0.065	1.4469
16		4.11	5.59	1.62			8.44	0.066	1.4466
17		3.83	5.21	1.51			7.44	0.067	1.4462
18		5.57	4.85	1.41			6.44	0.068	1.4459
19		3.35	4.55	1.32			5.44	0.066	1.4456

Then, we evaluate the performance of the MCF regarding TTDL operation. Here we focus mainly on the chromatic dispersion *D* and its slope *S* (indicated in Table 5.2 as well), and in spatial diversity operation. As some cores have the same chromatic dispersion, we focus on the dispersion slope to determine the best option in terms of delay variability with the optical wavelength. For instance, cores 5 and 6 have a |Δ*S*| of 0.005 and 0.001 ps/km/nm^2 with respect to core 7, respectively. As such, core 6 introduces less error in terms of differential group delay.

Figure 5.3(a) represents the chromatic dispersion of each core between 1530 to 1560 nm. Solid lines denote the dispersion of the cores with less dispersion slope difference (Δ*S*), while dashed lines represent the dispersion of the overlapping cores (cores with the same dispersion). Fig. 5.3(b) shows the differential group delay between core 1

and the remaining cores after adjusting the differential group delay mismatch at λ_0 = 1530 nm. As before, solid lines and dashed lines indicate, respectively, the best and worst option in the case where two cores have the same *D*. We observe the DGD increase progressively with the optical wavelength. In the case of overlapping samples, we see slight variations on the DGD because of the different ΔS.

Then, we investigate the differential delay between adjacent samples or basic delay $\Delta\tau$, depicted in Fig. 5.3(c). Dashed-dotted line indicates the average basic delay $\Delta\tau$ (differential delay between adjacent samples), whilst the light blue shaded area shows the range of the maximum extent of $\Delta\tau$ (maximum and minimum variation). The performance of the implemented functionality depends on how this delay deviates. The basic delay $\Delta\tau$ can be tuned from 0 up to 30 ps/km on average by changing the optical wavelength in a 30-nm span from 1530 nm. At 1560 nm, a maximum delay variability of about +- 2.5 ps/km is obtained. Lastly, Fig. 5.3(d) gathers the spatial delay relative error (computed with Eq. (2.12)) as a function of the optical wavelength. Likewise, solid and dashed lines represent, respectively, the best and worst core combinations to obtain the same time-delayed sample (indicated by a matching-colored line). As we see, the error increases with the optical wavelength. At 1560 nm, the relative error goes from 5 to 9% in the best and worst case, respectively. Therefore, in the best case we can obtain a 30-nm operability range with a 5% relative error.

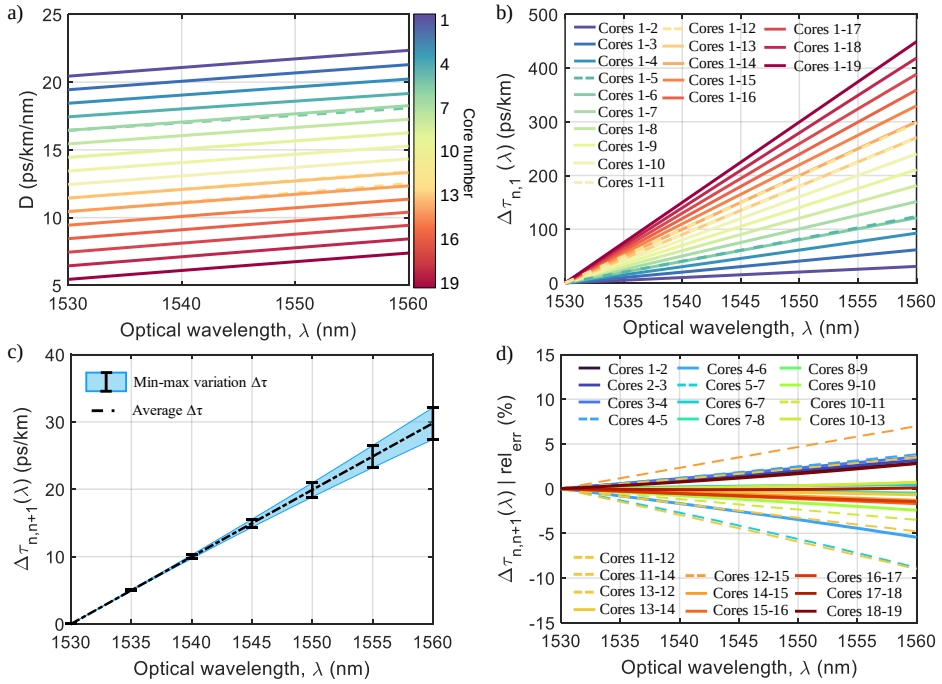

Fig. 5.3. Simulated TTDL performance of the preliminary design as a function of optical wavelength: (a) chromatic dispersion *D*, (b) DGD with respect to core 1, (c) DGD between adjacent cores and (d) spatial differential delay relative error. In (a,b,d) solid lines represent the best case and dashed lines the alternative cores/samples in each case. In (d) equal colors represent the same sample.

5.3. Final design

5.3.1. Characterization of the fabricated preforms

After obtaining the preliminary design, we looked for providers to fabricate the core preforms. The preforms were fabricated by the company *Prysmian*. Fig. 5.4 represents the comparison between the refractive index profiles for the designed and fabricated preforms. In total, 5 preform pieces were fabricated, distributed in (a) 2 TA-SI pieces (labelled as #1 and #2), (b) 1 RA-GI piece and (c) 2 TA-TI pieces (labelled as #1 and #2). We require a minimum length of 1 m long to have enough material for at least 3 MCF fabrication attempts. In some cases, due to the inherent fabrication complexity, the preform was divided into 2 shorter pieces (> 50 cm each). We calculate the dopant concentration of the fabricated preforms from the measured refractive index profile at 633 nm. Generally, the profile of the fabricated preforms matches well the design one. However, we observe a considerable discrepancy between the design and the fabricated preform for the TA-TI, as it was fabricated with a different inner cladding width (a_2). The RA-GI preform core presents a slightly different shape as well. Additionally, each preform piece has slightly different radial dimensions and dopant concentrations (most notably for the TA-TI preform). Nonetheless, the rest of structural design parameters match well the design targets. Table 5.3 gathers the estimated layer dimensions and the length of each fabricated preform piece.

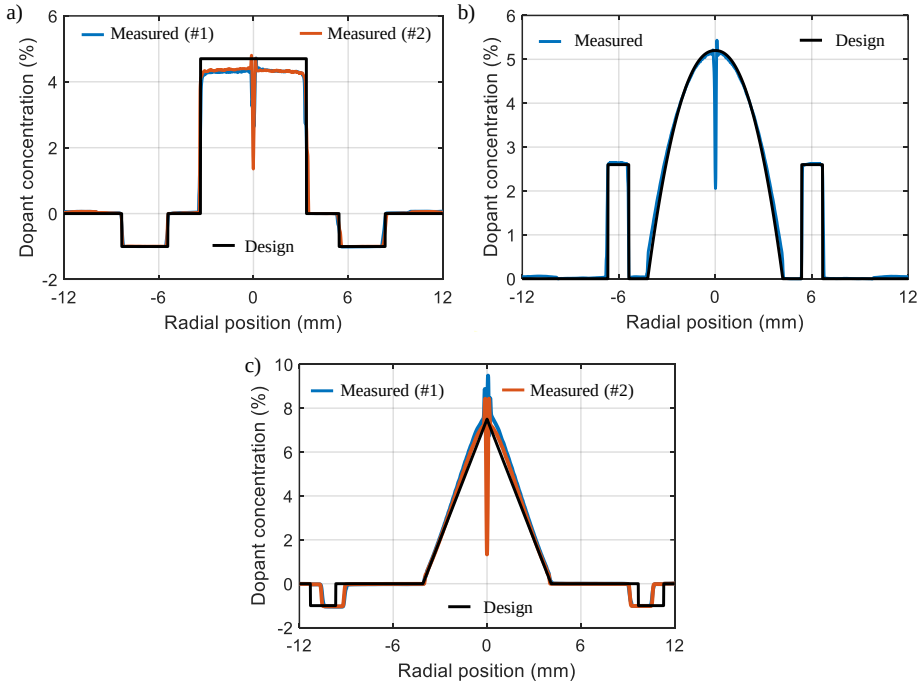

Fig. 5.4. Calculated dopant concentration from the design (black solid line) and the measured refractive index profile of the fabricated preforms (blue and orange solid lines) for preforms: (a) TA-SI, (b) RA-GI and (c) TA-TI.

Table 5.3. Estimated structural parameters of the different preforms pieces after fabrication.

Preform	Piece ID	*OD (mm)*	a_1 (mm)	a_2/a_1	a_3/a_1	n_1 *dopant* (GeO_2 *mol. %)*	n_3 *dopant*	Length (m)
TA-SI	#1	24.90	3.35	0.62	0.87	4.30	1.00% F	0.55
	#2	24.94	3.40	0.61	0.86	4.30	1.00% F	0.57
RA-GI	-	25.20	4.20	0.30	0.32	5.15	2.60% GeO_2	1.00
TA-TI	#1	29.51	4.10	1.20	0.39	8.50	1.00% F	0.70
	#2	29.45	4.05	1.20	0.39	8.00	1.00% F	0.70

5.3.2. Single-core test fibers

Then, we needed to check if the fabricated preforms can realize the expected chromatic dispersion as in the preliminary design. To do that, single-core test fibers were drawn at MPL from each preform with a different scaling factor to obtain a set of test fibers with different core dimensions. Specifically, we looked for fibers with a core radius of 3.5, 4.5 and 5 μm for preforms 1 and 3, and of 4.2, 4.5 and 5 μm for preform 2. The fabrication of the test fibers consists in two steps. First, an intermediate cane is fabricated by drawing a small part of each core preform. Fig. 5.5(a-c) gathers the measured cross-section view of each cane, where we can readily observe the different radial dimensions in each preform. The scaling factor from preform to cane is listed in Table 5.4. Second, single-core fibers are drawn from those intermediate canes. As a result of the fabrication, 10 test fibers were drawn from preform 1, and 6 from preforms 2 and 3. Table 5.4 gathers some details of the fabrication process (draw speed, scaling factor, preform used, etc.), as well as the target core radius. As a result of the fabrication, 10 test fibers were drawn from preform 1, and 6 from preforms 2 and 3, respectively. Here, the draw speed determines the total scaling factor. A higher draw speed realizes a smaller fiber size. A preform feed speed of 5 m/min was used in all cases for this fabrication process.

After fabrication, the refractive index profile of the test fibers was measured at the University of Lille (France) by an IFA-100 system at an optical wavelength of 550 nm (represented in Fig. 5.5(d, f, h)). Measuring the refractive index profile at that optical wavelength provides a resolution of 0.3 μm. This scarce resolution probably causes the index profile to soften, as that explains the clear difference with the preform refractive index (see Fig. 5.4). Solid and dashed lines represent scaling methods A and B, respectively. These scaling methods correspond to two different intermediate scaling factors, one based on the expected core radius after scaling down the preform (A) and the other based on the measured core radius (B). Fig. 5.5(e, g, i) stand for the microscope images of one of the fabricated test fibers for each preform and were measured at MPL after fabrication. The last two columns of Table 5.4 list the target radius and the estimated core radius from the microscope pictures of each test fiber. Scaling A is generally more accurate than B, except for the TA-SI preform fibers where additional fibers were required to match the target radius.

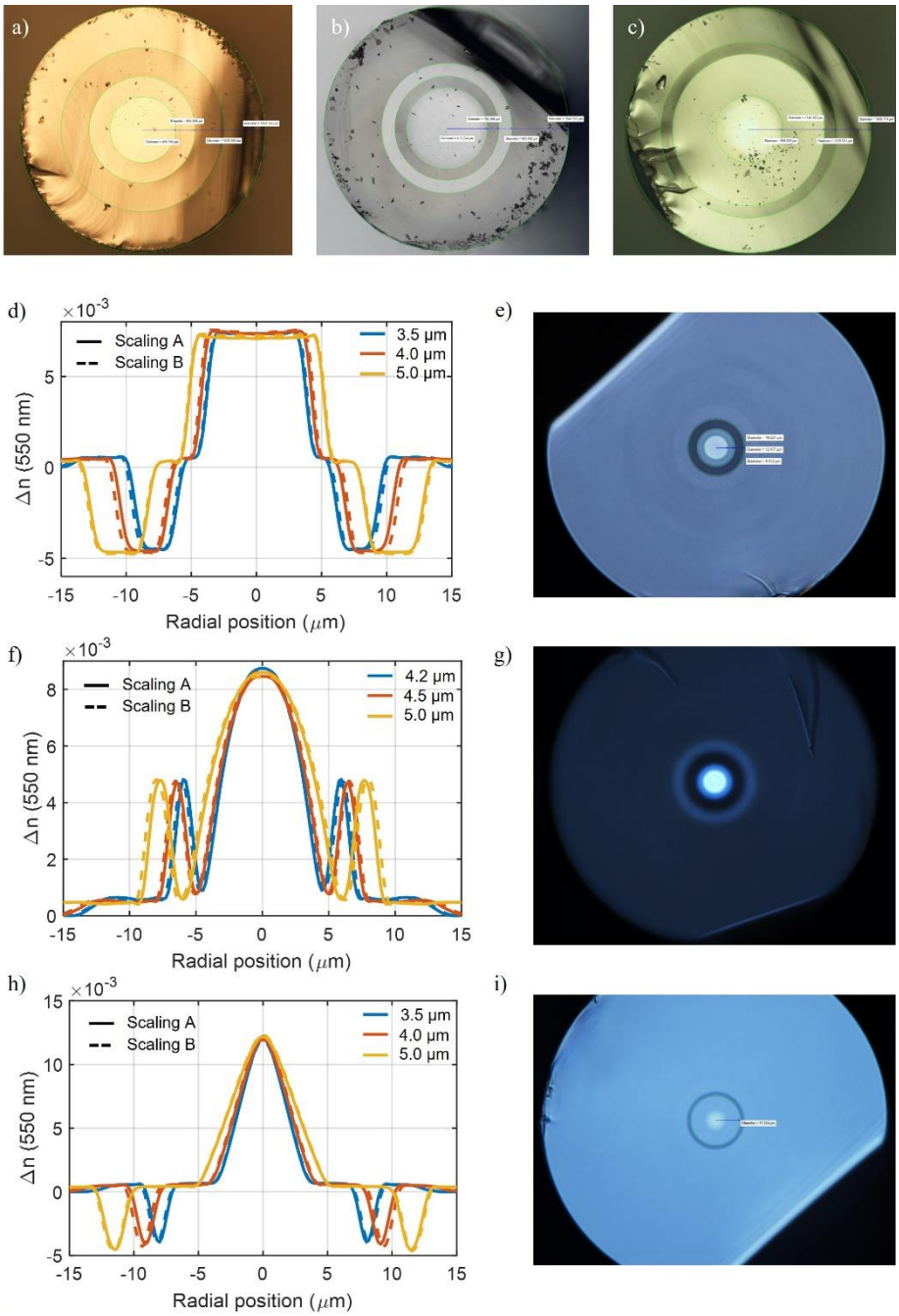

Fig. 5.5. (a-c) Cross-sectional view of the intermediate canes, (d, f, h) measured refractive index profile at 550 nm and (e, g, i) cross-section photograph of the fabricated test fibers for each preform type: TA-SI (a, d, e), RA-GI (b, f, g) and TA-TI (c, h, i).

Table 5.4. Drawing parameters of the single-core test fibers.

Fiber	Preform	Preform to cane scaling	Draw speed (mm/min)	Scaling cane to fiber	Total scaling factor	Scaling method [1]	Measured core radius (μm)	Target core radius (μm)
1	TA-SI (#1)	13.5	27.2	73.8	994.2	A	4.1	3.5
2			25.4	71.3	960.2	B	4.0	3.5
3			20.9	64.6	870.0	A	4.1	4.0
4			19.5	62.4	840.1	B	4.4	4.0
5			13.4	51.7	696.0	A	5.2	5.0
6			12.5	49.9	672.1	B	5.4	5.0
7			14.2	53.3	717.8	*	5.1	5.0
8			28.0	74.8	1008.0	*	3.6	3.5
9			29.0	76.2	1025.8	*	3.6	3.5
10			30.0	77.5	1043.4	*	3.4	3.5
11	RA-GI	13.6	28.6	75.6	1030.7	A	4.2	4.2
12			26.8	73.2	997.7	B	4.1	4.2
13			24.9	70.6	961.7	A	4.1	4.5
14			23.4	68.4	932.3	B	4.4	4.5
15			20.2	63.6	866.2	A	4.9	5.0
16			18.9	61.5	837.9	B	5.2	5.0
17	TA-TI (#1)	15.9	28.6	75.6	1203.8	A	3.4	3.5
18			30.1	77.6	1234.9	B	3.3	3.5
19			21.9	66.2	1053.4	A	3.9	4.0
20			23.0	67.8	1079.5	B	3.8	4.0
21			14.0	52.9	842.2	A	4.8	5.0
22			14.7	54.2	863.0	B	4.8	5.0

Then, we measured the chromatic dispersion of the test fibers using while light source interferometry (WLS), [124]. Simultaneously, the measured refractive index profile of the test fibers was processed and simulated in *Fimmwave* to compare with the measured results (see Fig. 5.6). Both results match well generally but they are far from the designed values (see Table 5.5), especially for the graded-index preform. In that case, the small step at the bottom of the core (see Fig. 5.4(b)) produces an increment on the chromatic dispersion of those cores. This has a big impact on the chromatic dispersion, especially in those cores with a small radius. Also, as mentioned earlier, the triangular preform has a different inner cladding width a_2, which also alters the final chromatic dispersion. We estimate again the core size using the refractive index profile from the test fibers.

Overall, the data obtained with the test fibers is not accurate enough to approximate the chromatic dispersion dependence with the scaling factor. As such, we resort to the modeling of the preform refractive index profiles to redesign the MCF design.

[1] Additional test fibers were drawn with other scaling factors.

Table 5.5. Test fibers characterization results: core radius estimation from index profile (and the corresponding scaling factors), and the expected, simulated and measured chromatic dispersion.

Fiber	Preform	Core radius, a_1 (μm)		Total scaling factor	D (ps/km/nm) @1550 nm		
		Target	Estimated		Target	Simulated	Measured (WLS)
1	TA-SI (#1)	3.5	3.8	994.2	17.3	18.7	18.9
2		3.5	3.9	960.2	17.3	18.9	19.3
3		4.0	4.2	870.0	18.9	19.6	19.6
4		4.0	4.4	840.1	18.9	19.8	-
5		5.0	5.2	696.0	20.2	20.5	-
6		5.0	5.5	672.1	20.2	20.6	-
7		5.0	5.2	717.8	20.2	20.4	-
8		3.5	3.7	1008.0	17.3	18.3	18.3
9		3.5	3.6	1025.8	17.3	18.0	17.7
10		3.5	3.5	1043.4	17.3	17.7	17.6
11	RA-GI	4.2	4.0	1028.5	10.4	11.5	-
12		4.2	4.1	1004.8	10.4	11.8	-
13		4.5	4.4	945.3	11.0	12.3	12.4
14		4.5	4.5	926.3	11.0	12.3	12.8
15		5.0	5.3	786.7	12.2	14.0	14.5
16		5.0	5.5	760.8	12.2	14.4	14.7
17	TA-TI (#1)	3.5	3.4	1198.8	6.1	5.9	6.7
18		3.5	3.4	1216.6	6.1	5.5	5.8
19		4.0	3.9	1045.9	8.3	7.8	7.0
20		4.0	3.8	1078.9	8.3	7.6	6.0
21		5.0	4.9	842.2	11.6	10.3	11.1
22		5.0	4.8	863.0	11.6	10.2	10.8

5.3.3. Preform modelling

Figure 5.6 gathers the refractive index profile of the preform and the simplified model that matches the preform refractive index profile (a,c,e), and the comparison between the chromatic dispersion for this model and for the scaled preform simulation as a function of the scaling factor (b,d,f). Solid and dashed lines arise from the refractive index profile simulation in *Fimmwave* for the simplified model and the scaled preform measurement. The gray vertical dashed line represents the point where the core starts to propagate more than one mode ("multimode region"). The WLS-measured and *Fimmwave*-simulated dispersion values from the test fibers are indicated as black crosses markers and orange circles, respectively. Orange dash-dotted line represents the second-order polynomial fit of the test fibers dispersion simulation. We see that the dispersion from the model and the preform has a similar trend in each preform. On the other hand, the difference observed between the model and the test fibers simulation fit is probably caused by the scarce resolution obtained in those measurements (0.3 μm). Therefore, we use the simplified preform model

(colored solid line) to select the new scaling factors for each core. From that model, we select the scaling factors that produce cores with a dispersion difference ΔD = 1 ps/km/nm. Because the dispersion range provided by the RA-GI preform is different than expected in the preliminary design, one core is transferred from the RA-GI preform to the TA-SI one. Table 5.6 lists the total scaling factor and the main propagation characteristics for each core at 1550 nm. The chromatic dispersion ranges from 7.5 to 21.5 ps/km/nm at that wavelength.

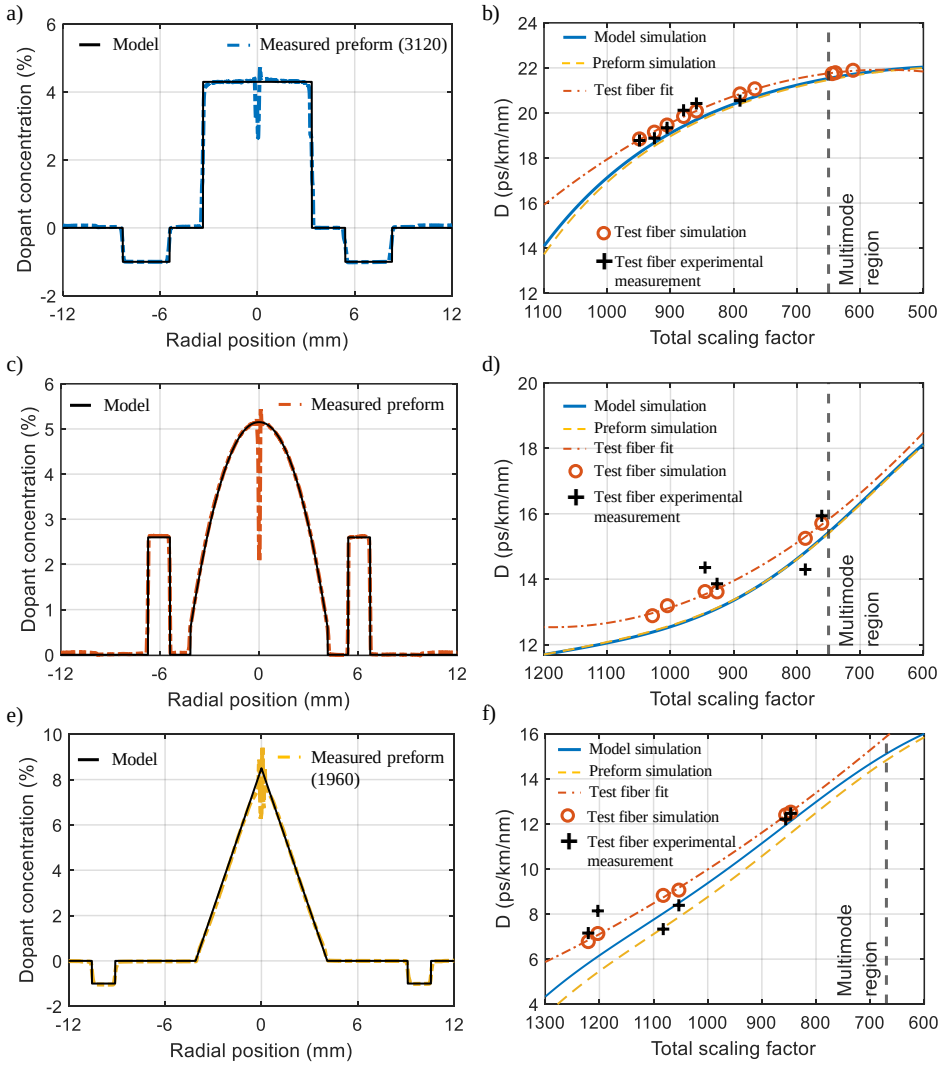

Fig. 5.6. (a, c, e) Measured preform refractive index profile (dash-dotted lines) and simplified preform model for each preform (black solid lines), (a: TA-SI, c: RA-GI, e: TA-TI). (b, d, f) Chromatic dispersion comparison of the refractive index profile simulation for the simplified model (blue solid lines), measured scaled preform (yellow dashed lines) test fibers simulation (red circles markers and dash-dotted line), and measured test fibers dispersion (black cross markers) at 1550 nm, (b: TA-SI, d: RA-GI, f: TA-TI).

Table 5.6. Optical propagation properties of each core in the final 19-core MCF design at 1550 nm.

Core	Preform	Total scaling factor	D (ps/km/nm)	S (ps/km/nm^2)	n_{eff}
1	TA-SI	655	21.50	0.063	1.4480
2		789	20.50	0.061	1.4473
3		873	19.50	0.059	1.4469
4		935	18.50	0.056	1.4465
5		984	17.50	0.054	1.4463
6		1025	16.50	0.051	1.4461
7	RA-GI	636	17.50	0.060	1.4482
8		690	16.50	0.060	1.4480
9		746	15.50	0.061	1.4477
10		808	14.50	0.062	1.4474
11		886	13.50	0.065	1.4471
12		1007	12.50	0.068	1.4466
13	TA-TI	770	13.50	0.062	1.4459
14		826	12.50	0.062	1.4483
15		880	11.50	0.062	1.4480
16		935	10.50	0.063	1.4476
17		992	9.50	0.063	1.4473
18		1051	8.50	0.064	1.4470
19		1113	7.50	0.064	1.4466

5.3.4. Simulated TTDL performance

Similarly to the preliminary design (shown in Fig. 5.3), Fig. 5.7 gathers the calculated TTDL performance of the final design from 1530 to 1560 nm by means of (a) the dispersion of each core, (b) the differential group delay between core 1 and the remaining cores, (c) the basic delay $\Delta\tau$ variability and (d) the spatial delay relative error (computed with Eq. (2.12)). The basic differential delay can be tuned up to 30 ps/km on average by changing the optical wavelength in a 30-nm range. At 1560 nm, the delay variability increases to +- 5 ps/km because of the higher ΔS variability in the final design (up to 0.01 ps/km/nm^2). The maximum spatial diversity relative error is around 15.8% for cores 6 and 9. Compared to the preliminary design, we obtain worse differential delay when accounting for all alternative samples, but a more accurate delay is achieved in the best case as the spatial error diminishes to 4%.

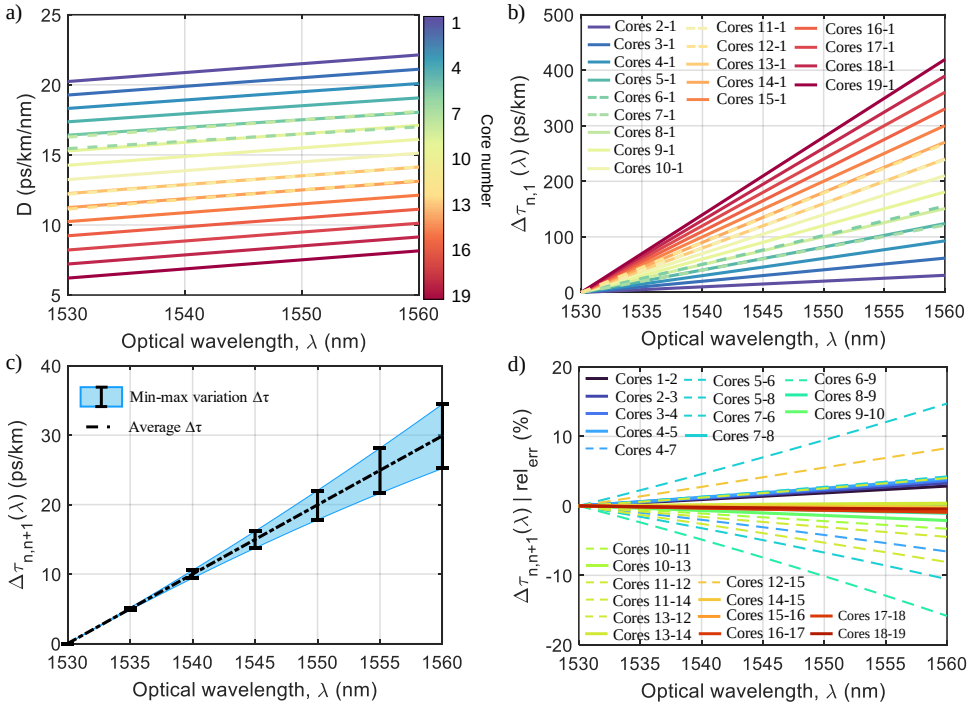

Fig. 5.7. Simulated TTDL performance as a function of optical wavelength of the final design: (a) core chromatic dispersion, (b) DGD with respect to core 1, (c) DGD between adjacent pairs of cores and (d) Spatial differential delay relative error. Solid lines represent the best case and dashed lines the alternative samples provided by the overlapping cores.

5.3.5. Core arrangement and inter-core crosstalk

After obtaining the scaling factors of every core, we arrange them taking into account the effective index n_{eff} of each core and the core refractive index profile. As a result, cores with the same refractive index profile don't neighbor themselves. Fig. 5.8(a) represents the core arrangement for this MCF design and the simulated inter-core crosstalk behavior with the bending radius (b-d). The core pitch Λ is 40.6 µm and the cladding diameter is 278 µm. These two parameters are determined by fabrication specification. The minimum effective index difference $\Delta n_{eff} = 2 \cdot 10^{-4}$, is obtained from cores 3 and 12. This results in a theoretical critical bending radius R_{pk} = 260 mm for this fiber, as we see in Fig. 5.8(b), where we calculate the maximum and average crosstalk for each bending radius. There, we also observe the crosstalk peaks arising from the phase matching between certain core pairs. Inter-core crosstalk is calculated by CPT using Eqs. (2.6)-(2.8) and by computing numerically the MCC between adjacent cores (detailed in Annex I). Then, Fig. 5.8(c-d) show the statistical crosstalk distribution of each core with the adjacent cores for a bending radius of 70 mm and 140 mm, respectively. The crosstalk distribution at 140 mm shifts towards smaller values than in the 70-mm case, which relates to the average crosstalk in Fig. 5.8(b). However, the proximity to a phase-matching peak worsens crosstalk for some particular core pairs.

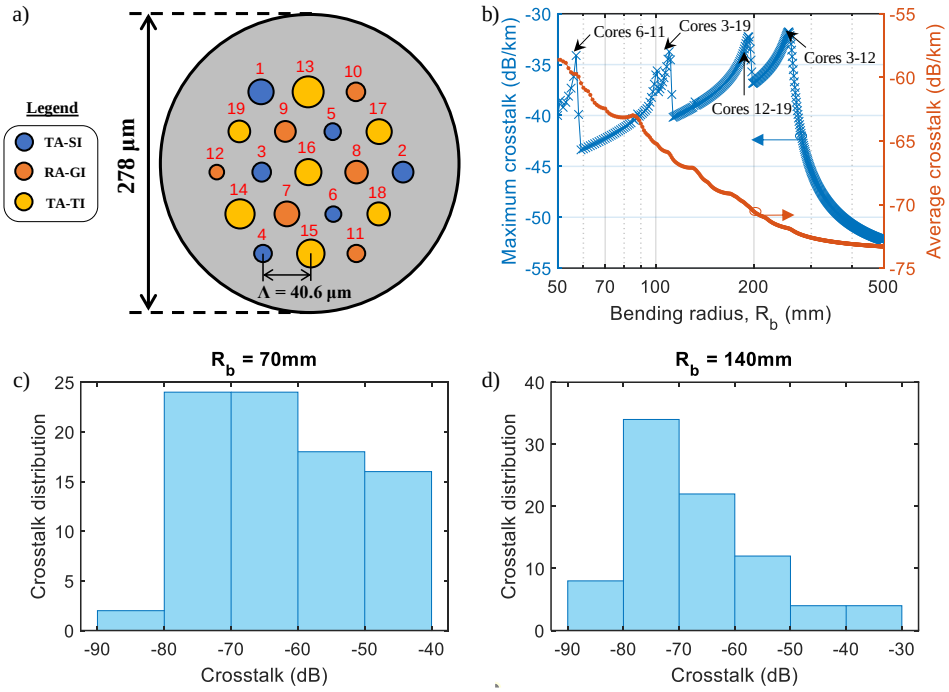

Fig. 5.8. (a) Core arrangement within the fiber (b) Maximum (blue) and average (orange) inter-core crosstalk behavior with the bending radius. Crosstalk distribution at bending radius (c) R_b = 70 mm and (d) R_b = 140 mm.

5.4. Multicore fiber fabrication

This section details the fabrication of the MCF during my stay at MPL, where I was able to assist in some of the fabrication steps. The MCF was fabricated with the stack-and-draw technique. In this technique, the different elements of the fiber (core rods, supporting rods, jacketing tubes, etc.) are placed in a structure, which is called the stack. Then the stack is driven into a jacketing tube, that then becomes the outer cladding layer of the final fiber, and this structure forms the MCF preform which is drawn finally at a fiber tower to obtain the fiber. Following, we describe the specific steps for the fabrication of the fiber. This includes the preparation of the different fiber elements involved in the stacking, preform stacking and fiber drawing.

5.4.1. Stacking elements preparation

First, the different capillaries that compose the stack need to be fabricated. This includes core canes (drawn from the core preforms), core jacketing tubes and supporting rods (also called supports), which are drawn from a pure silica preform rod (as depicted in Fig. 5.9(a). Core size is determined in this step by drawing at a different speed (as in the case of the test fibers). Several samples from the core preforms were collected at the cane tower (Fig. 5.9(b)). Supports were drawn in two different sizes (see Fig. 5.10(c)).

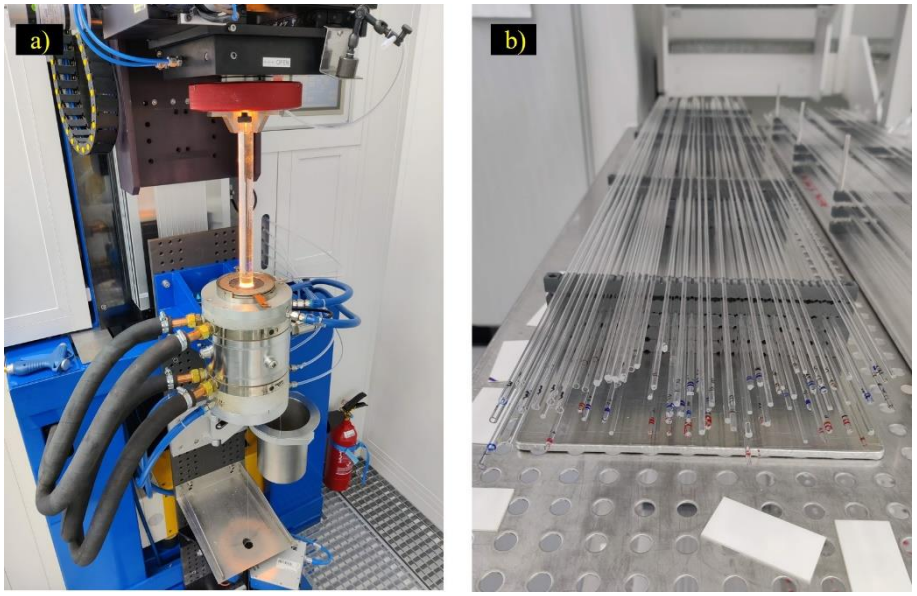

Fig. 5.9. (a) Top of the "cane tower" where the furnace is located. (b) Bottom of the tower, where drawn capillaries are collected and stored.

5.4.2. Stacking

After preparing the elements, we proceed to stack them to form the structure that is the MCF preform. The stacking is done in a clean room to prevent particle contamination. Fig. 5.10 gathers some of the stacking procedure steps inside the clean room. First, most core canes are inserted into jacketing tubes with the same outer diameter but a different inner-to-outer diameter ratio. The outer diameter is 3.654 mm, which after fiber drawing results in a core pitch of 40.6 μm. In contrast, cores 7 and 13 (the largest ones of preforms RA-GI and TA-TI) are stacked directly without a jacketing tube. This is done to provide uniformity to the structure, as each core capillary has a different size. Fig. 5.10(a) and (b) depict the final result of stacking the capillaries following the core arrangement depicted in Fig. 5.8(a). Then, supports are used to ensure the structure is maintained and that the fiber has a circular shape (Fig. 5.10(c)). Lastly, the stack is introduced into the final jacketing tube (Fig. 5.10(d)). The tube has an inner and outer diameter of 19 and 25 mm, respectively. Like the core pitch, the expected cladding diameter is 278 μm after fiber drawing. After this process, the MCF preform is almost ready for fiber drawing.

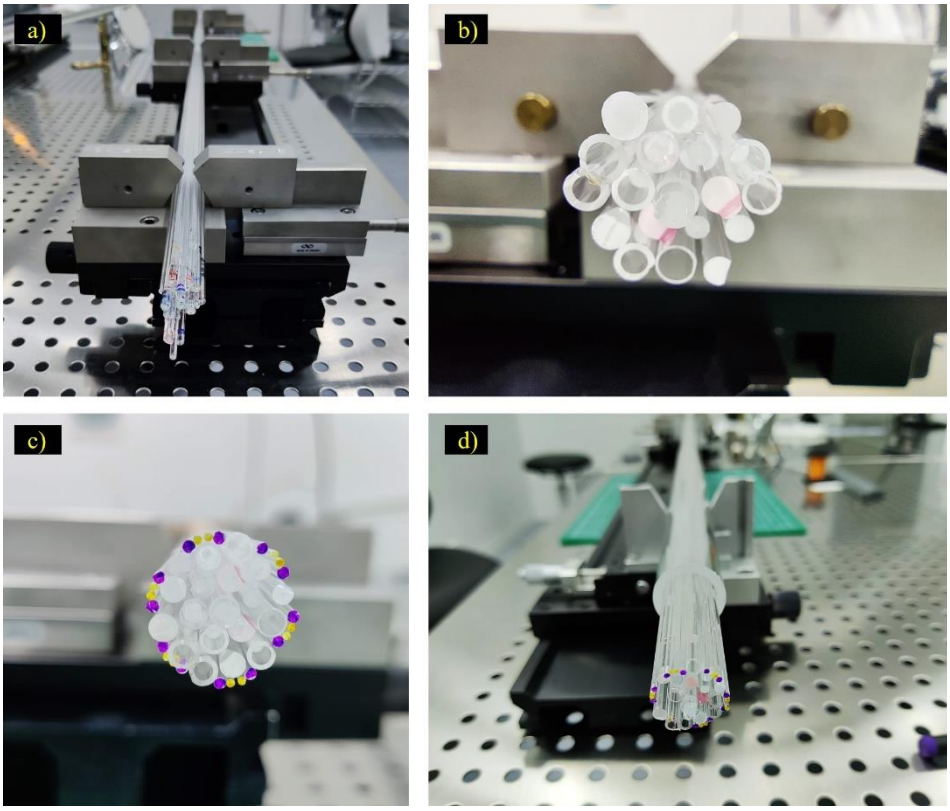

Fig. 5.10. Stacking procedure in the clean room. (a) Stacked capillaries on the mounting rack. (b) Close view of the stacked capillaries (where canes and jackets can be spotted). (c) The stack after placing the supporting rods. (d) The stack after being introduced into the outer jacketing tube.

Still, we realized an additional step before drawing where we tapered the stack on one end to create a grip. This prevents the stack from sliding out of the jacketing tube when placed in vertical position. The taper is formed with a high-temperature blowtorch (Fig. 5.11(a)). In Fig. 5.11(b), we see the taper created on one end of the stacked preform. Then, the MCF preform is brought to the cane tower to collapse the other end in the furnace. As a consequence, the tube is now sealed, and this allows vacuum to be applied during fiber drawing. The piece of glass at the beginning of the preform, known as the drop-off, is depicted on the right-hand side of Fig. 5.11(c), where we compare its cross-section view with the designed MCF. There, we see the different elements inside the stacked preform, including core capillaries, jacketing tubes and supports, before the fiber is drawn. Core dimensions seem to match well the design at this point.

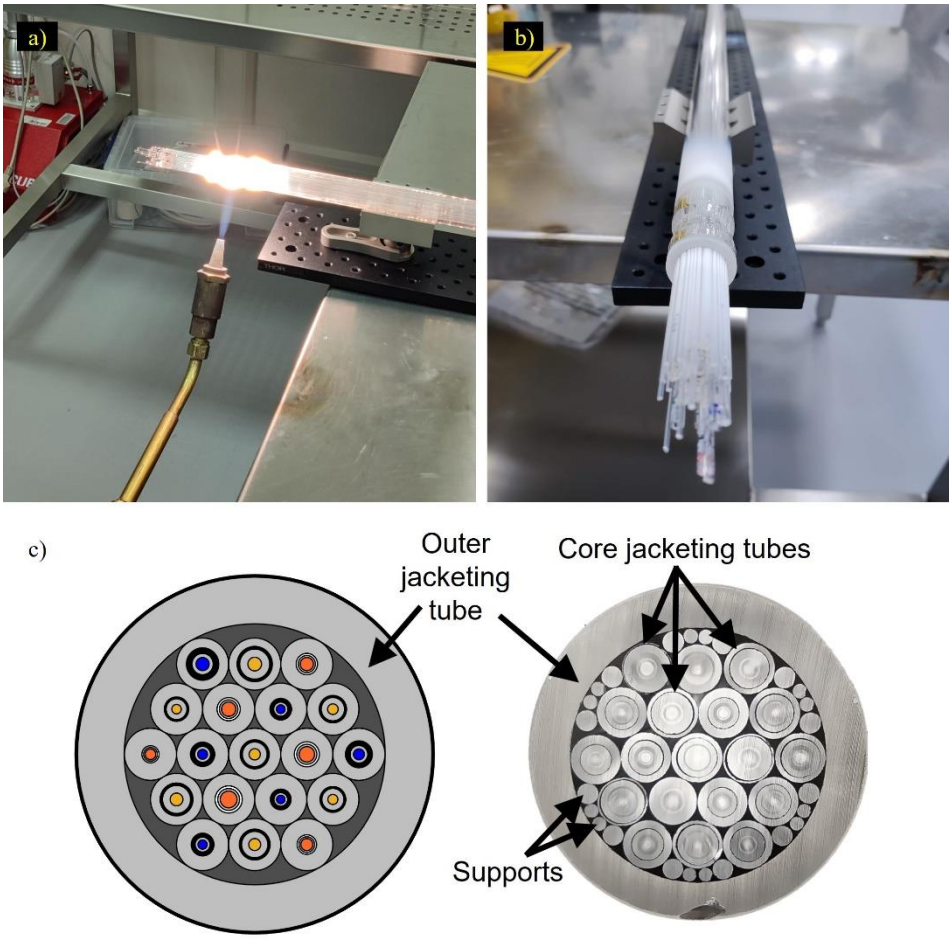

Fig. 5.11. (a) Blowtorch being applied to the outer tube of the preform to collapse the structure at that point. (b) End result of the process. (c) Cross-section view of the design sketch (left) and the preform drop-off (right).

5.4.3. Fiber drawing

After the previous step, the fiber is now ready for drawing. As represented in Fig. 5.12, the fiber tower comprises three floors. Top left photograph shows the furnace located at the top, the MCF preform is already loaded onto it and is being heated up by the furnace. The preform is held at the top by a feed screw. Air blowers cool the top part of the preform to prevent it from loosening due to heat. Top right photograph displays the second floor of the tower, where the fiber diameter is monitored during the draw. Middle photograph shows the first floor of the fiber tower. At this stage, tension is applied to the fiber with tractor wheels, which apply a pulling force (bottom photograph). We identify some elements such as the control instruments and the fiber coating stage. The drawn fiber is collected onto a drum (white spool in Fig. 5.12). Several fiber samples are collected during the drawing process to adjust the drawing process parameters.

Fig. 5.12. (Top) From left to right, third and second floor of the fiber tower, respectively. The furnace locates at the third floor. (Middle) First floor of the fiber tower. (Bottom) Tractor system and spooling wheel.

5.4.4. First fabrication round

The previous describe the process of fabricating a multicore fiber via the stack-and-draw technique. After that, a first fiber fabrication attempt was realized during my stay at MPL. Unfortunately, the drawing process was more complex than expected, and interstitial spaces were observed in consecutive fiber samples. The suspected reason is the doped areas of the MCF contract at a different rate than the expected one. Finally, the fiber was successfully drawn in a second trial, where these issues were solved by adjusting the drawing parameters (furnace temperature, draw speed, feed speed, pressure, etc.) and by adding additional supports between core capillaries. The fabricated fiber is smaller than expected initially, as it has a cladding diameter of 268 μm, a core pitch of 39 μm and a 470-μm coating diameter. The fiber is coiled in a 7.5-cm spool and is 4.2-km long. Again, the doped areas seem to have shrunken more than expected, which means the MCF preform was scaled down in a different ratio to follow the designed core sizes. Unfortunately, this translates into a smaller core separation, which could affect crosstalk performance.

5.4.4.1. Initial characterization

Figure 5.13 depicts the measured cross-section view photographs of the fiber beginning (a) and the fiber end (b) taken by an optical microscope. We observe cores in both pictures present similar dimensions and their location matches well the design. We see, though, that some cores present an elliptical shape. Thus, we estimate the cores radii from Fig. 5.13(b) using the scale in it. Table 5.7 contains the estimated core radius, as well as the calculated ellipticity and difference with the design. Vertical and horizontal axes are measured in each core to calculate the ellipticity. A maximum deviation of 9.6% is observed for core 12, which is also the most elliptical one. Overall, the size of the cores in the fabricated MCF is similar to the design, but the high degree of ellipticity in some cores could introduce undesired effects on the fiber performance as a TTDL, such as losses or PMD.

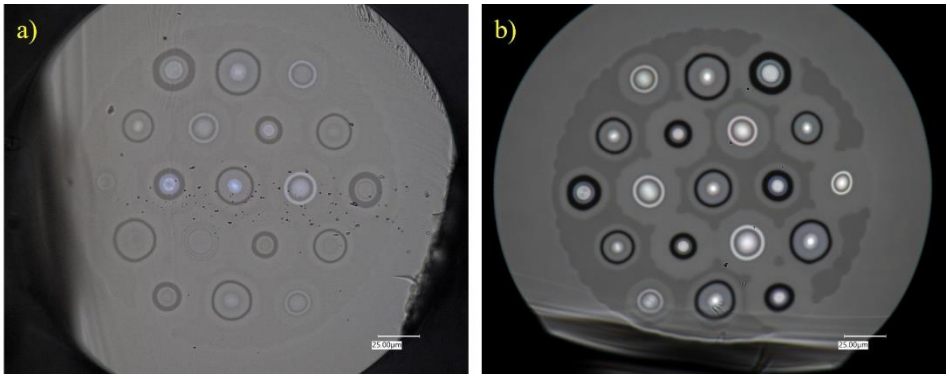

Fig. 5.13. Optical microscope photographs of the fabricated 19-core MCF at the: (a) fiber beginning and (b) fiber end.

Table 5.7. Estimated core radius from Fig. 5.13(b), calculated ellipticity and difference in core radius size with the design.

Core	Core radius (µm)		Ellipticity	Core radius difference with the design			
	Horizontal axis	Vertical axis		Horizontal axis (µm)	Vertical axis (µm)	Horizontal axis (%)	Vertical axis (%)
1	5.22	5.10	0.02	0.11	-0.02	2.10	-0.40
2	3.97	4.36	0.09	-0.27	0.12	-6.40	2.80
3	3.98	3.90	0.02	0.14	0.06	3.70	1.50
4	3.35	3.58	0.07	-0.23	0.00	-6.50	0.00
5	3.51	3.43	0.02	0.10	0.02	3.00	0.70
6	3.12	3.19	0.02	-0.15	-0.07	-4.70	-2.30
7	6.78	7.01	0.03	0.25	0.49	3.90	7.50
8	6.00	5.92	0.01	-0.02	-0.09	-0.30	-1.60
9	5.45	5.69	0.04	-0.11	0.12	-2.00	2.20
10	5.30	5.45	0.03	0.16	0.32	3.10	6.20
11	4.78	4.86	0.02	0.09	0.18	2.00	3.80
12	3.90	4.52	0.14	-0.23	0.40	-5.50	9.60
13	5.26	5.22	0.01	-0.07	-0.10	-1.20	-2.00
14	5.22	4.60	0.12	0.26	-0.37	5.20	-7.40
15	4.67	4.91	0.05	0.02	0.25	0.30	5.30
16	4.28	4.36	0.02	-0.10	-0.02	-2.30	-0.50
17	4.28	4.05	0.05	0.15	-0.08	3.70	-2.00
18	3.97	3.98	0.00	0.07	0.08	1.90	2.00
19	3.58	3.63	0.01	-0.10	-0.05	-2.70	-1.40

To test the fabricated fiber, a couple of fan-in/fan-out devices were fabricated by the company *Chiral Photonics*. They feature a maximum insertion losses of 2.2 dB for the whole fan-in + 15-m long MCF + fan-out structure. The level of inter-core crosstalk is below -40 dB in most cases. After splicing them to the 4.2-km long fiber, we measured the optical power at the output of the cores with an optical power meter and a laser source centered at 1550 nm, but we were not able to measure any power. Thus, we used an OTDR to identify if there was any defect in the fiber. Thanks to this, we were able to locate two different defects, one in each fiber end, at 1.243 and 1.725 km, respectively. Fig. 5.14 plots the OTDR traces of each core when coupling light from fiber beginning (a) and fiber end (b). From the traces, we see that most cores exhibit propagation losses that range from 0.6 up to 9 dB/km. High propagation losses could be attributed to core ellipticity, core deformation and higher material absorption. Waveguide imperfections are also attributed to higher losses [123].

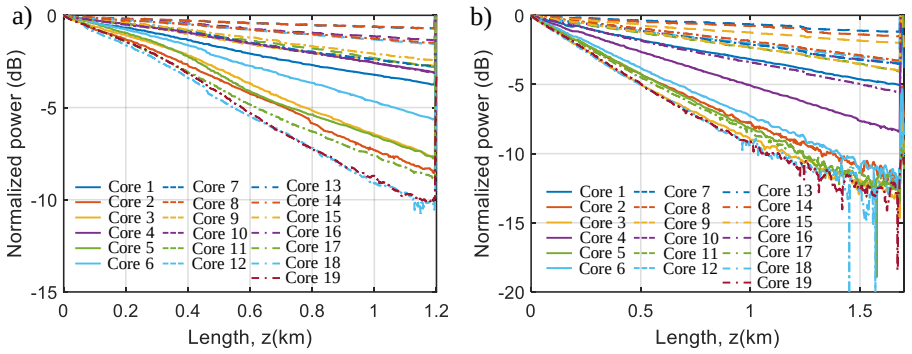

Fig. 5.14. OTDR traces at 1550 nm of the 19 cores in the MCF coupling from: (a) fiber beginning and (b) fiber end.

5.5. Future work

As we saw in the previous section, a 4.2-km long MCF was fabricated with similar core dimensions to the design. Unfortunately, at the time of writing this PhD Thesis, a couple of fiber defects (one in each end) impede the full fiber characterization. In addition, the fiber has excessively high propagation losses in most cores (as depicted in Fig. 5.14). Therefore, we require a second fabrication trial to optimize the drawing process and overcome these obstacles. All in all, it would be better to first characterize this first fiber sample in terms of chromatic dispersion and DGD. To do that, the following step would be to remove the defects in the fiber and complete the characterization with the remaining fiber length. After that, we would obtain information about the chromatic dispersion of each core in the MCF. Depending on the outcome of that characterization, a second design readjustment might be necessary to provide the required propagation characteristics for TTDL operation. Apart from that, the fabrication process calls for further improvement to reduce propagation losses.

5.6. Conclusions

In this chapter, we describe the process of designing and fabricating a heterogeneous 19-core MCF that acts as a tunable 15-sample TTDL. Instead of obtaining each core with an individual preform, this MCF design resorts to the scaling of three different-index profile preforms. That way, fabrication costs can be saved, making high-core-count/high-sample-number tunable TTDLs more feasible to produce. The preforms have, respectively, a trench-assisted step-index, a ring-assisted graded-index and a trench-assisted triangular-index refractive index profile. We obtained a preliminary MCF design, with a spatial diversity operation of 16 samples (3 overlapping samples). To fabricate the fiber, a total of 5 preforms pieces were fabricated by the company *Prysmian*. After characterizing each preform piece individually, we adjusted the first design to account for the variations observed in the refractive index of the preforms. The final design features a chromatic dispersion that ranges from 7.5

to 21.5 ps/km/nm at 1550 nm. The designed fiber has a core pitch of 40.6 μm and a cladding diameter of 278 μm.

The fiber was fabricated at MPL facilities using the stack-and-draw technique. A first fabrication attempt was undertaken during my stay at MPL, where I was able to assist in the fabrication process. A preform stack was built in a clean room following the core arrangement from the design. After inserting it into a 25-mm outer-diameter tube, the preform stack was brought to the furnace in the fiber tower. As a result, a 4.2-km long fiber was fabricated, though it has a core pitch of 39 μm and a cladding diameter of 268 μm. The drawn core sizes match well the design figures, though we observe some degree of ellipticity in a few cores, which could introduce losses and/or delay changes. A couple of fan-in/fan-out devices were custom fabricated by the company *Chiral Photonics* for this specific fiber. Unfortunately, we have not been able to fully characterize the fabricated fiber because fiber defects block the light inside the fiber. As we cannot deal with the removal of the defects in our facilities, this, and the characterization of the fiber in terms of chromatic dispersion and differential group delay are left as future lines of work. In addition, a second fiber fabrication trial is necessary to solve the high propagation losses that we observed in some cores. And depending on the outcome of the characterization, it could also include a possible design readjustment.

Chapter 6
Novel applications of heterogeneous MCFs

6.1. Introduction

This chapter proposes specialized applications that require a particular MCF design. First, we center on QKD, where MCFs are viewed as a way to increase key-rate capacity. The feasibility of coexisting traditional data with QKD channels in the same fiber is investigated by using the model derived in [125] for different types of MCFs. We modeled the crosstalk characteristics of two commercial homogeneous MCFs and obtained a customized ultra-low crosstalk heterogeneous MCF design. Then, we propose the concept of a dispersion compensation MCF to counteract (or at least alleviate) the effect of chromatic dispersion on potential MCF transmission networks. We design a four-core fiber with the standard cladding diameter for SMF. Two alternative designs are provided, a homogeneous design and a heterogeneous one. Lastly, we introduce the concept of parallel temporal Talbot effect. We design an MCF in which each core provides pulse repetition rate multiplication (PRRM) with a multiplication factor ranging from 2 to 64.

6.2. Quantum Key Distribution (QKD)

6.2.1. Introduction

In Chapter 2 we reviewed the implementation of QKD from pure laboratory tests to actual QKD fiber network demonstrations. Here, we evaluate the integration of QKD channels into SDM optical fiber transmission by using the system model developed in [125]. This model takes into account the transmission of both classical and quantum channels in order to assess the impact of each relevant physical parameter on the final performance of each channel and the feasibility of the design under consideration. We consider homogeneous and heterogeneous MCFs for the transmission media, as well as the possibility of arbitrarily choosing the number of classical and quantum channels transmitted over the SDM medium. The system

model takes into account the impact of intercore crosstalk, which requires the knowledge of the inter-core crosstalk coefficients for MCFs.

For the final simulations we consider two different practical cases. One when the SDM fiber only transmits quantum channels and the second one when both classical (high power) and quantum channels coexist. In both cases, the determination of the QBER parameter per QKD channel requires the solution of N coupled implicit equations, where N is the number of cores transmitting quantum keys. From these QBER values, one can obtain the optimized number of photons per pulse for decoy state operation and, ultimately, the net key rate for each QKD channel.

6.2.2. MCF design

6.2.2.1. Homogeneous multicore fibers

Different levels of intercore crosstalk are considered by evaluating two representative homogeneous MCFs that are characterized by different PCCs. The first one (MCF #1) is a 7-core fiber analyzed by Cartaxo and Alves in [126], which is characterized by a core pitch of 30 μm, a cladding diameter of 125 μm, a core radius of 4 μm and a relative refractive index difference between core and cladding of 0.5%. The second MCF (MCF #2) is a commercially available 7-core fiber provided by *Fibercore* (SM-7C1500), [127]. It has a core pitch Λ of 35 μm, a cladding diameter of 125 μm, an estimated core radius of 3 μm and an estimated relative core-cladding index difference of 0.96% (estimated from the parameters given in its specifications: numerical aperture in the range 0.20-0.22 and mode field diameter in the range 5.7-6.5 μm at an optical wavelength of 1550 nm).

Figure 6.1 shows the dependence of the average PCC with the bending radius, which was calculated using Eq. (2.8), for both homogeneous MCFs, considering a correlation length d = 50 mm [44], [128]. As expected, the PCC increases linearly with the bending radius due to the reduction in the index difference between the cores, reaching its theoretical maximum value if the fiber were totally straight. Actually, in the particular case of homogeneous MCFs, the average PCC is simplified as:

$$\bar{h}_{mn} = \frac{2K_{mn}^{\ 2} d}{\sqrt{1+\left(\frac{\beta_m \Lambda_{mn} d}{R_b}\right)^2}} \ . \tag{6.1}$$

When the bending radius is small ($R_b << \beta_m \Lambda_{mn} d$), being Λ_{mn} the distance between two adjacent cores, then

$$\bar{h}_{mn} = \frac{2K_{mn}^{\ 2} R_b}{\beta_m \Lambda_{mn}} , \tag{6.2}$$

And the average PCC is independent of the correlation length d and depends linearly on R_b, as given as well by the mean crosstalk derived from the coupled mode theory, [22] [6]. For both homogeneous MCFs evaluated here, the factor $\beta_m \Lambda_{mn} d$ is in the order of 8 m, so we consider that the practical fiber deployment scenarios are within

the regime of small bending radii. The significant difference between both PCC responses arises from the fact that the *Fibercore* fiber has a higher core pitch and better mode confinement.

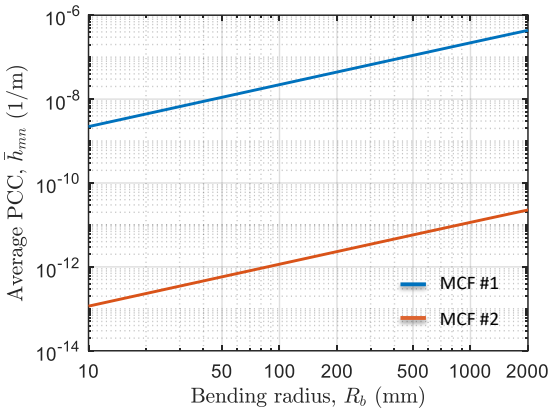

Fig. 6.1. Average PCC dependence on the bending radius for the evaluated homogeneous MCFs (#1: [126], #2: [127]).

6.2.2.2. Heterogeneous multicore fiber

Even though the previously evaluated second homogeneous MCF provided a good crosstalk performance for classical data transmission, the range of computed average PCC values still needs to be lowered for specific scenarios of combined QKD and classical channel transmission scenarios. Intending to further reduce the intercore crosstalk, we designed a particular ultralow-crosstalk 7-core MCF built upon trench-assisted heterogeneous cores. The design is based on three different types of cores, each with a different radius and dopant concentration. One type is used as the central core and the other two as the outer cores, so neighboring cores are dissimilar. Fig. 6.2 (a) depicts the cross-section of the designed fiber with its three types of cores (type A: blue color, type B: yellow color and type C: orange color) and Fig. 6.2(b) shows the refractive index profile of a trench-assisted core.

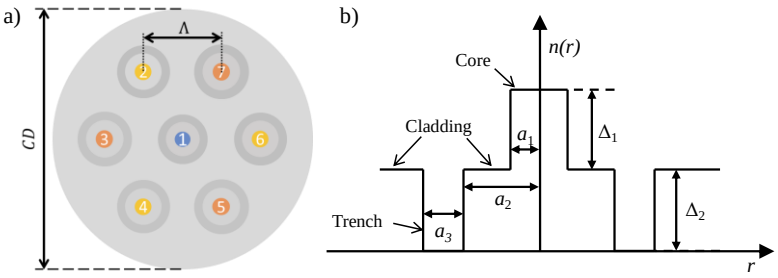

Fig. 6.2. (a) Cross-section of the designed heterogeneous trench-assisted MCF (each color illustrates a different type of core); (b) Core refractive index profile, being a_1: core radius; a_2: inner cladding radius; a_3: trench width; Δ_1: core-to-cladding relative index difference; Δ_2: cladding-to-trench relative index difference.

The design strategy we followed supports three main goals. First, the average PCC should be at least as low as 10^{-14}, to allow pure quantum and hybrid quantum/classic transmission without significant penalties. Second, as agreed in [128], we must ensure a critical bending radius lower than 10 cm to avoid an undesired crosstalk increase due to phase matching between cores when the fiber is bent. And third, the cores must remain in the single-mode operation regime to avoid intermodal crosstalk.

The parameters of the heterogeneous MCF design and the propagation characteristics (effective index n_{eff} and effective area A_{eff}) computed with *Photon Design Fimmwave* software are gathered in Table 6.1. To further reduce the average crosstalk, we set the core pitch to 45 μm and the cladding diameter to 150 μm.

Table 6.1. Core parameters of the designed heterogeneous MCF.

Parameter	Core A	Core B	Core C
a_1 (μm)	4.2	4.5	4.7
a_2/a_1		2.0	
a_3/a_1		1.0	
Δ_1	0.58%	0.48%	0.38%
Δ_2		-0.63%	
n_{cl}		1.444	
n_{eff}	1.449	1.448	1.447
A_{eff} (μm^2)	60.31	70.55	80.91
CD (μm)		150	
Λ (μm)		45	

Fig. 6.3 shows the average PCC $\overline{h_{mn}}$ for any possible core pair combination considering a correlation length d = 50 mm, [22], [44], [128]. As characteristic of heterogeneous MCFs, we observe a peak in the magnitude of PCC caused by forced phase matching between cores for a specific value of the bending radius that is called the critical bending radius. Although this particular design aimed to reduce the magnitude of this crosstalk peak as much as possible, we must bear in mind that the optimum working zone is the one corresponding to bending radii above this critical value. Nevertheless, we must take into account that, in practice, the fiber link is not uniformly bent at this critical bending radius (which corresponds to the worst-case scenario). Instead, depending on the link deployment, the heterogeneous MCF will experience different curvatures and twists, being the total crosstalk, an accumulation of the different crosstalk sources experienced along the link. For the core combinations represented here, one critical bending radius is located at 33 mm while the other two at 65 mm (worst case). Total crosstalk can be calculated using Eqs. (2.6)-(2.8) for a given fiber length. For example, an average PCC value of 10^{-14} results in an accumulated crosstalk level of -110 dB/km.

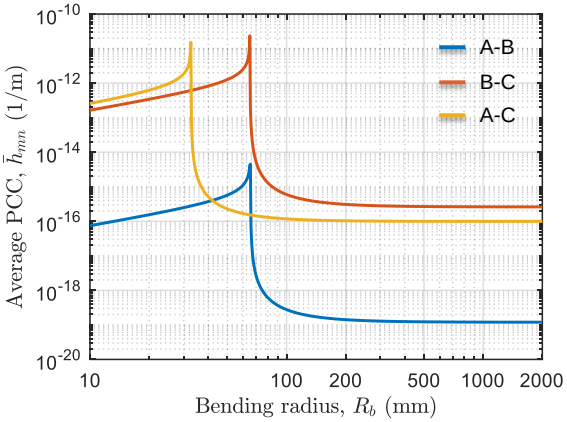

Fig. 6.3. Average PCC dependence on the bending radius for different core pair combinations of the designed heterogeneous MCF. The blue solid line is the average PCC between type A and B cores, red dotted line is the average PCC between type B and C cores and yellow dashed line is the average PCC between type A and C cores.

6.2.3. Results and discussion

We proceed now to analyze the possibility of multiple channel QKD transmission using MCFs. For this purpose, we employ the model developed in [125] together with the relevant parameters of representative MCFs given in section 6.2.2. In addition, we consider typical values for the parameters characterizing the pulse sources and photon counters given in Table 6.2. We will assume that these parameters are the same for these devices regardless the core number, that is: $d_{B,n} = d_B$, $\rho_n = \rho$, $V_n = V$, $T_{nn} = T$.

Table 6.2. Faint pulse/Classical laser source, photon counter and fiber loss typical parameter values employed in the simulations.

Simulation parameter	Physical concept	Value/Range
d_B	Photon counter dark count rate	0.98×10^{-6}
ρ	Photon counter responsivity	0.1 (A/W)
V	Receiver visibility	0.98
λ	Source wavelength	1550 nm
μ_c	Equivalent number of photons per pulse in the classical channels	106
$P = \mu_c (hc / \lambda)$	Laser power for classical channels at 1550 nm	1 mW
μ_{opt}	Optimum number of photons per pulse in quantum channels	0.1-0.5 as given by the application of Eqs. (12)-(13) in [125]
$T = 10^{-\frac{\alpha}{10}L}$ $\alpha = 0.2$ dB/km	Transmission factor core n, length L	Depending on the link length

6.2.3.1. Quantum channel transmission only

We consider in first place the case where only quantum channels are transmitted through the SDM optical fiber. For practical reasons, we consider a 7-core homogeneous MCF as it is the most straightforward commercially available solution. We consider two cases of MCFs representative of moderate and low inter-core crosstalk levels that have been described in section 6.2.2. In the first case, the maximum values of the inter-core coupling coefficient are around $h = 10^{-7}$ m^{-1}, in the second they are around $h = 10^{-11}$ m^{-1}. Fig. 6.4 shows the obtained results for the capacity and optimum average photon number as a function of the MCF link length after solving Eqs. (10)-(12) in [125]. Fig. 6.4(a) and (b) represent the results for the moderate intercore crosstalk MCF. As it can be observed, the outer peripheral cores show an identical performance as expected as each one is subject mainly to the crosstalk of three closest neighboring cores. The central core displays worse results as it is subject to the crosstalk of 6 closest neighboring cores, hence the capacity is $R_{net,central\_core} + 6R_{net,i}$, where i stands for any peripheral core. If, however, the inter-core crosstalk is low, then its effect is almost negligible, as shown in Fig. 6.4(c) and (d), where it is clear that all cores feature an identical performance in terms of net capacity and present equal values for the optimum number of photons per bit. Note as well that in this second case the net rate is $7R_{net,i}$, and i stands for any core.

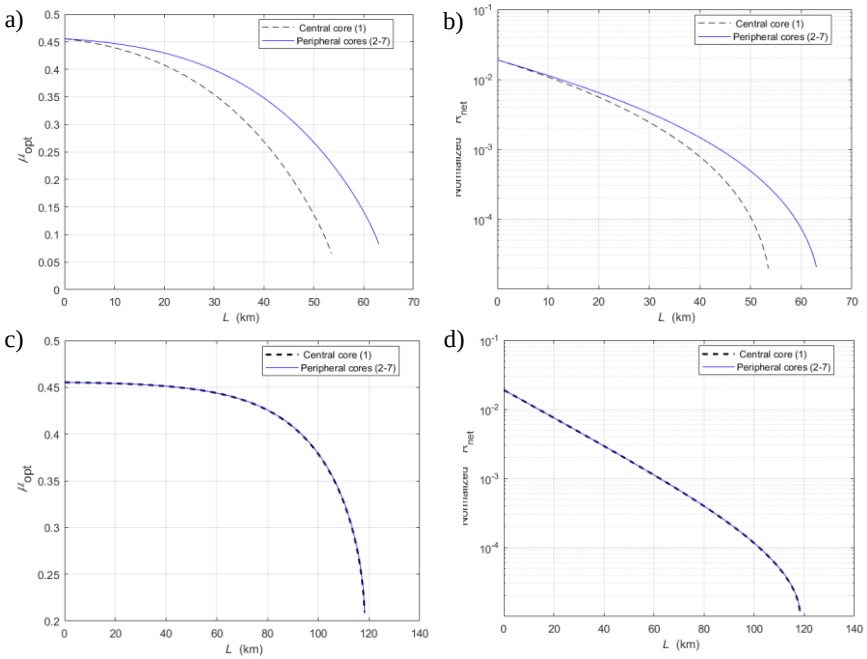

Fig. 6.4. (a) Optimum number of photons per bit vs link distance L in km. (b) Net Normalized key rate (to the pulse repetition rate f_{rep}) per core vs link distance L in km for a moderate intercore crosstalk (the coupling coefficients are in the order of $h = 10^{-7}$ m^{-1}) 7- core homogeneous MCF. (c) Optimum number of photons per bit vs link distance L in km. (d) Net Normalized key rate (to the pulse repetition rate f_{rep}) per core vs link distance L in km for a low intercore crosstalk ($h = 10^{-11}$ m^{-1}) 7-core homogeneous MCF.

The results indicate that, in principle, multiple quantum channel transmission is viable both for moderate as well as for low inter-core crosstalk 7-core homogeneous MCFs. In the first case, at least 6 cores are expected to display identical performance in terms of net key rate, and distances of up to 40 km are reachable, which covers the access segment distance range. In the second, this figure can eventually rise to identical behavior of the 7 cores and transmission distances around 100 km for key rates over 1 kb/s per core. This covers access as well as moderate distance metropolitan segments.

6.2.3.2. Simultaneous transmission of quantum and classical channels

We consider the case of introducing one classical channel in the MCF, while the rest of the cores transmit quantum channels. In this case, the classical transmitter is a pulsed optical transmitter providing standard output power values (i.e., between 1 and 10 mW). This is well represented by a coherent state with $\mu_c = 10^6$. Two cases of interest correspond to transmitting the classical channel through the central core or a peripheral one, respectively. Fig. 6.5 represents the obtained results for these two cases when the transmission medium is a low intercore crosstalk ($h = 10^{-11}$ m^{-1}) 7-core MCF. Fig. 6.5(a) gives the results for the case where the classical core is sent through the central core, while Fig. 6.5(b) depicts the same results when the classical channel is transmitted by a peripheral core.

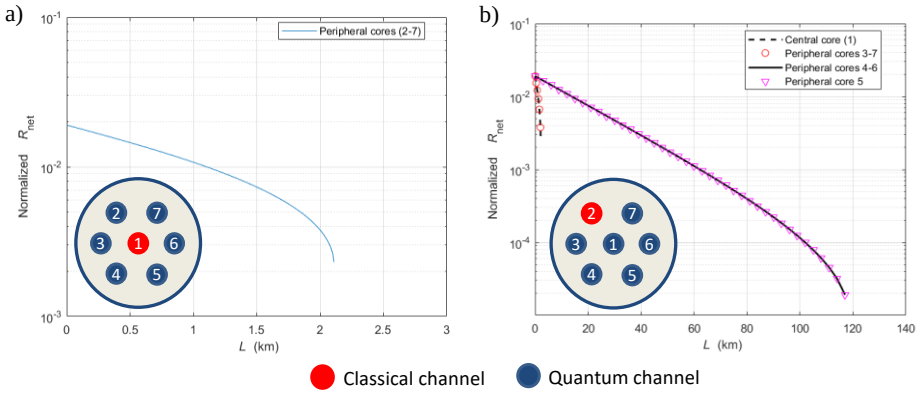

Fig. 6.5. Net Normalized key rate (to the pulse repetition rate f_{rep}) for QKD channels versus the link distance in an SDM-QKD link supporting one classical channel and 6 QKD channels and implemented using a 7-core homogeneous MCF with intercore coupling coefficients around $h = 10^{-11}$ m^{-1}. (a) Case where the classical channel is transmitted by the central core. (b) Case where the classical channel is transmitted by peripheral core #2.

As we can appreciate, the introduction of a classical channel in the central core has a profound impact over the maximum reach of the rest of quantum channels, posing a severe restriction, in the range of 2-2.5 km. In practical terms, this makes QKD transmission unfeasible except for a very short reach distance. When the classical channel is transmitted through a peripheral core, it impacts the central core and the other two near peripheral neighbors while the other three peripheral cores are unaffected.

To accommodate both quantum and classical channels and be able to use all the cores in the MCFs, further simulations have shown that one needs coupling coefficients in the range of $h = 10^{-14}$ m^{-1} or smaller. These can only be attained by means of heterogeneous MCFs and we consider the ultralow-crosstalk design reported in section 6.2.2.2. Fig. 6.6 shows the results for different cases of combined classical and quantum channel transmission. Intercore coupling coefficients between the three groups of cores are, $h_{1,2} = 4 \cdot 10^{-17}$, $h_{2,3} = 4 \cdot 10^{-16}$ and $h_{1,3} = 1.5 \cdot 10^{-15}$ m^{-1}. Fig. 6.6(a) corresponds to the case where a single classical channel is transmitted through the central core (core #1) and quantum channels are delivered in the rest of the peripheral cores (#2 to #7). As it can be appreciated, both transmission regimes are supported by the MCF. Key rates for QKD channels are almost identical within the linear range (up to 80 km), with a departure from that attainable in cores belonging to the group formed by #2, #4, #6 and that attainable in cores belonging to the group formed by #3, #5, #7. This behavior is to be expected as the inter-core coupling coefficients with core #1 are different. Since cores #2, #4, #6 have a very small (in fact negligible) coupling coefficient with #1, they feature a performance in terms of net key rate identical to a channel with zero coupling as shown in the inset of Fig. 6.6(b). Channels #3, #5, #7 have a slightly higher coupling coefficient ($h_{1,3}$), which is enough to result in a different key rate for higher distances. In any case, both the classical and quantum channels can coexist within the heterogeneous MCF transmission link.

Figure 6.6(b) corresponds to the case where a single classical channel is transmitted through a peripheral core (core #2). In this case, QKD transmission is feasible in the rest of the cores with the same key rates, which corresponds to negligible crosstalk impact as it can be appreciated by comparing to the inset of Fig. 6.6(b). Equal performance can be attained up to 100 km. The possibility of using more than one core for classical transmission is demonstrated by the results given in Fig. 6.6(c) and (d). Fig. 6.6(c) illustrates the results for the case where 3 cores (#2, #3 and #7) are employed for classical transmission and 4 (#1, #4, #5 and #6) are employed for QKD. Again, QKD transmission with almost equal net key rate per core is feasible, with a slight worse value for the central core (#1) that experiences the highest inter-core crosstalk values. Equal core performance for up to around 80 km is possible. Finally, Fig. 6.6(d) shows the case where 6 classical channels and one QKD (in core #1) are transmitted. This corresponds to the highest impact of intercore crosstalk. Again, in this case QKD transmission is feasible up to distances around 80 km. These results should be compared to those of Fig. 6.5.

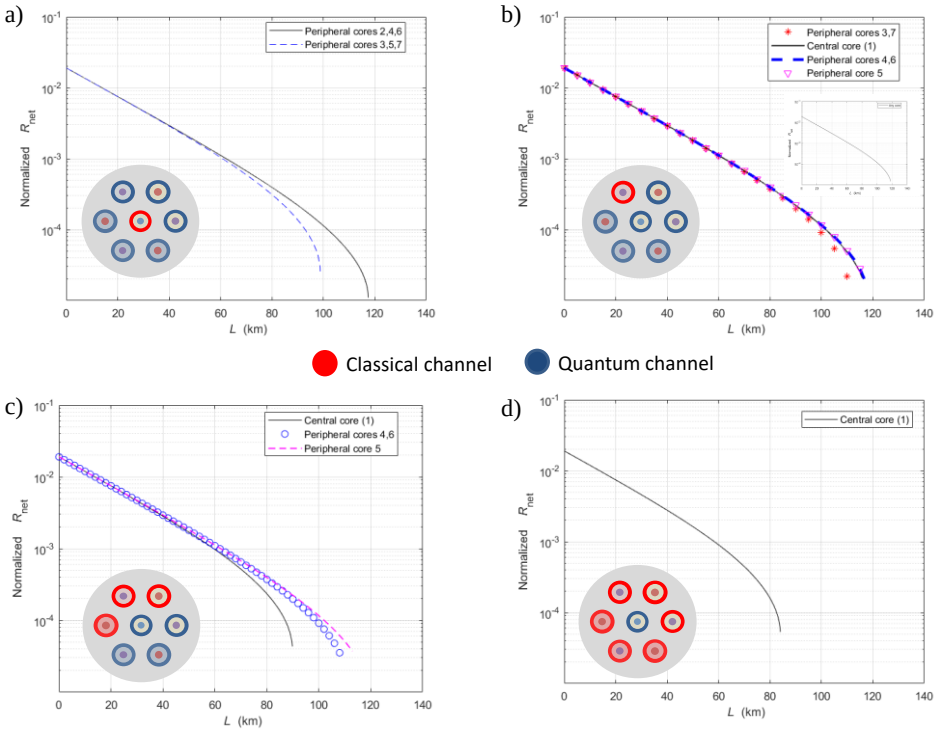

Fig. 6.6. Net Normalized key rate (to the pulse repetition rate f_{rep}) per core vs link distance L in km for very low inter-core crosstalk (coupling coefficients range from $h = 10^{-15}$ m^{-1} to $h = 10^{-17}$ m^{-1}). (a) One classical channel transmitted by the central core (core #1) and 6 QKD channels (cores #2-#7). (b) One classical channel transmitted by the peripheral core (core #2) and 6 QKD channels (cores #1 and #3-#7). (c) Three classical channels transmitted by cores #2, #3 and #7 and four QKD channels (#1, #4, #5 and #6). (d) One QKD channel transmitted by the central core (#1) and six classical channels transmitted by the peripheral cores (#2-#7). Color code for cores transmitting classical and quantum channels is the same as in Fig. 6.5.

6.2.3.3. Final remark

Here we have analyzed the feasibility of QKD transmission in 7-core MCFs for two scenarios of practical interest. The first accounts for the use of SDM to transmit only QKD channels. We have found that standard homogeneous MCFs enable transmission distances compatible with the required net key rate, which are very close to those of single-core SMFs. Therefore, parallel QKD transmission of N channels or a xN multiplication of a single channel key rate over a given link distance is possible. The second scenario accounts for the simultaneous transmission of QKD and classical channels. Here we found that homogeneous MCFs cannot support this transmission regime as the inter-core crosstalk is too high. Heterogeneous MCFs can be designed to reduce this value to such levels that make this option feasible.

6.3. Dispersion compensation

6.3.1. Motivation and background

In a fiber transmission system three major parameters must be managed: losses, chromatic dispersion and nonlinearities. First, losses can be easily compensated by using optical amplifiers such as EDFAs or Raman amplification. Second, as it is widely known, chromatic dispersion causes pulse broadening and can lead to inter-symbol interference, limiting the signal's bit rate per propagation distance product. For instance, the transmission length for a 1-dB eye-closure penalty reduces from 58 to 3.6 km when the bitrate is increased from 10 to 40 Gb/s [129]. Therefore, dispersion must be managed for high-capacity communication channels such as in terrestrial/submarine long-haul links. Typically, dispersion-compensating fibers (DCF) have been used to counteract the effect of chromatic dispersion after a given transmitting fiber. The transmitting fiber is generally a standard SMF or a NZ-DSF and each type of fiber requires its own DCF design [129]. Lastly, nonlinearities such as self-phase modulation and four-wave mixing limit the amount of power and WDM channels that can be carried in an optical fiber. As introduced in Chapter 2, nonlinearities are regarded as the main limitation on current systems (i.e., nonlinear Shannon limit) [2], [130]. In current high-speed coherent systems, these two effects are managed by DSP, which can compensate for arbitrary amounts of accumulated chromatic dispersion, PMD and self-phase modulation. However, these are active systems that need to scale up with the number of channels. Consequently, the complexity and energy consumption that they require could be unachievable in the future.

In an analogous situation, we can consider a fiber link where the transmitting fiber is an MCF. With the development of multicore EDFAs, optical losses can be compensated efficiently in MCF networks by using a single element instead of having to amplify each spatial path individually. Related to this, the first demonstration of a MCF cable with an integrated EDFA was done recently [131]. A MCF with dispersion compensation cores could be used to compensate dispersion effects and could also be easily integrated into future dispersion-managed cables. This approach has the advantage of being a passive component and would also reduce the processing requirements for DSP systems.

6.3.2. MCF design

As explained in Chapter 2, MCFs with the standard SMF cladding diameter (125 μm) have the advantage of reduced mechanical failure probability, improved fiber fabrication productivity and compatibility with current optical components (connectors, cables, splicing techniques, etc.) [31], [33]. For those reasons, future optical networks could be comprised of 125-μm cladding diameter MCFs. In that work, they propose different homogeneous 4-core MCFs meant to upgrade current SMF links in different situations. The core count is limited to 4 because the core pitch (Λ) is optimized for inter-core crosstalk and low excess loss in the outer cores (caused by a low outer cladding thickness). Therefore, taking into account all the above

considerations, we consider a 4-core MCF with the standard cladding diameter of 125 μm for our MCF design, as shown in Fig. 6.7(a).

To obtain negative dispersion we need to select an appropriate core refractive index profile. First-generation DCF designs had a single layer comprised of a highly doped small core [132]. By allowing the mode to propagate outside the core, material dispersion contributions are reduced and thus waveguide dispersion becomes dominant [129]. These designs focused on compensating dispersion in a single wavelength and had limited performance compensating several WDM channels simultaneously, due to same-sign dispersion slope [132]. Second-generation designs include different additional layers and generally comprise a depressed region and/or a ring to obtain normal dispersion. Adding more layers gives better control over the chromatic dispersion and its slope. Negative dispersion below -100 ps/km/nm can be easily obtained with this core type, whilst also having a negative dispersion slope. Further DCFs developments have demonstrated the possibility of achieving a large negative dispersion (<-1000 ps/km/nm) [133], [134]. These approaches, though, either depend on phase-matching conditions between the modes in the core and the ring [134] which translates into a narrowband behavior in which dispersion peaks at a given wavelength. Or use higher order modes, as in [133], where the LP02 mode provides a large negative dispersion coefficient with large effective area. The drawback is that multipath interference between the different modes produces modal noise, which is generally undesirable.

Hence, we investigate the inclusion of triple cladding refractive index profiles in an MCF. Fig. 6.7(b) represents the core refractive index profile which is comprised of a GeO_2-doped triangular-index core surrounded by a Fluorine-doped trench and a GeO_2-doped raised ring. The design target is to obtain large negative dispersion with sufficiently low inter-core crosstalk at the optical wavelength of 1550 nm. Additionally, the dispersion slope should be negative to compensate several WDM channels at the same time. Lastly, as managing crosstalk is the main problem to obtain large negative dispersion in MCFs with this type of core, we compare a homogeneous and a heterogeneous design.

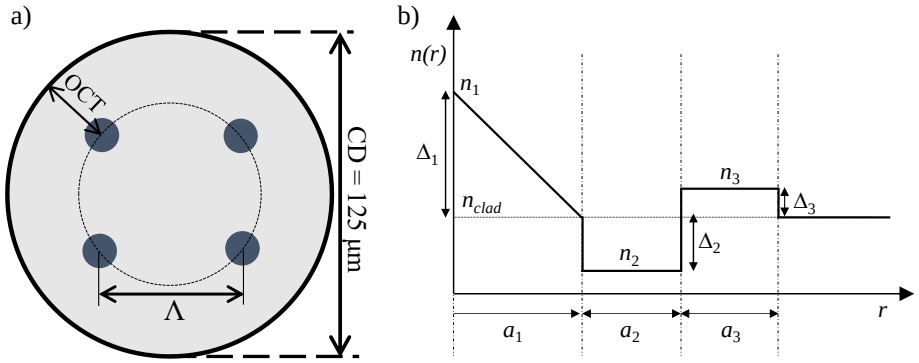

Fig. 6.7. (a) Cross section of a 4-core MCF with standard cladding diameter. OCT: outer cladding diameter CD: cladding diameter. Λ: core pitch. (b) Refractive index of a triangular-index triple cladding profile core.

Figure 6.8(a) represents the contour plot of the chromatic dispersion for different core radii (a_1) and relative core-cladding index differences (Δ_1). The effective index (n_{eff}) of the fundamental mode (red dashed curves) is also represented. The trench width (a_2) and the ring width (a_3) are both set to 2 μm, while the trench-cladding relative index difference (Δ_2) and the ring-cladding relative index difference (Δ_3) are -0.62% and 0.5%, respectively. As aforementioned, we can see that to get negative dispersion the core needs to be small and highly doped, what inevitably results in lower effective index and thus lower mode confinement. This could be problematic in an MCF because low-confined cores tend to increase intercore crosstalk. Fig. 6.8(b) represents the average inter-core crosstalk (in dB/km) in the case of a homogeneous MCF with Λ = 40 μm. Here, the average inter-core crosstalk is approximated by calculating the mode coupling coefficient of a step-index core with the analytical expression from [38] and by the coupled-power expressions for the average crosstalk developed by Koshiba et al. in [44]. As can be observed, the cores with the largest negative chromatic dispersion have a n_{eff} below 1.4450 and produce high intercore-crosstalk levels (>-30 dB/km). Thus, we look for the cores with n_{eff} above this level. Despite this, a relatively large negative chromatic dispersion (<-100 ps/km/nm) can still be obtained with this profile when considering a core-to-cladding relative index difference Δ_1 > 2%.

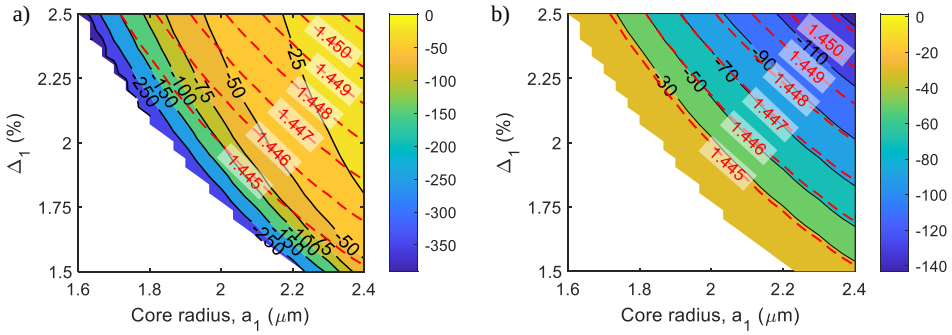

Fig. 6.8. (a) Contour representation of chromatic dispersion against a_1 and Δ_1. The rest of parameters are a_2 = 2 μm, a_3 = 2 μm, Δ_2 = -0.62% and Δ_3 = 0.05%. Red dashed lines represent the effective index of the fundamental mode. (b) Contour representation of the approximated average inter-core crosstalk (dB/km) at 70 mm against a_1 and Δ_1. In this calculation, cores are separated by Λ = 40 μm and the fiber is bent on a 70-mm radius. A correlation length (d) of 50 mm is used to calculate the average inter-core crosstalk.

We have seen the dependence of the chromatic dispersion on both a_1 and Δ_1 when the rest of the parameters are kept fixed. On the other hand, increasing the trench width (a_2) and trench dopant concentration (Δ_2) enhances waveguide dispersion when the mode field is outside the core (small a_1 and/or Δ_1). However, the mode effective index (n_{eff}) decreases and thus intercore-crosstalk increases. Further, mode confinement is enhanced by increasing the ring parameters (a_3 and Δ_3), but then higher-order modes start propagating within the ring at certain point, which further increases the design complexity. Table 6.3 summarizes the dependence of the modal propagation characteristics with the design parameters.

Table 6.3. Summary of the effect that increasing the different core design parameters has on the main optical propagation characteristics.

	D	n_{eff}	Crosstalk
$\uparrow a_1$	↑↑	↑↑	↓↓
$\uparrow \Delta_1$	↑↑	↑↑	↓↓
$\uparrow a_2$	↓↓	↓↓	↑↑
$\uparrow \Delta_2$	↓↓	↓↓	↑↑
$\uparrow a_3$	↑	↑	↓
$\uparrow \Delta_3$	↑	↑	↓

Once we know how to tune the different design parameters to obtain the required propagation characteristics, it is important to evaluate the design from the fabrication point of view. Apart from the fabrication tower itself, the fiber preform is the costliest element in the fabrication of an optical fiber. As we saw in the previous chapter, once the preform is produced, the only option to obtain the required dispersion is to scale it down with the proper scaling factor. For that reason, we analyze the behavior of a preform with the scaling factor.

Figure 6.9 represents the scaling factor dependence on both the chromatic dispersion (a) and the dispersion variation due to fabrication (dD/dFactor) (b). Here we consider a preform with $w = a_1$ and $\Delta_1 = 2.43\%$ for three different trench-to-core proportions (a_2/a_1). A scale factor of 1 corresponds to a core radius of 2 μm. As we appreciate in Fig. 6.9(a), a lower a_2/a_1 enhances mode confinement and provides similar dispersion to the other cases. In Fig. 6.9(b), the preform performance is analyzed from the point of view of variability during the fabrication (dD/dFactor). The dD/dFactor represents, in a certain way, the derivative of the chromatic dispersion with the scaling factor; more specifically, it represents the variation on the chromatic dispersion for an equivalent scaling factor change of 0.1 μm in the core radius. We can see that a narrower trench (a_2/a_1 = 0.75) minimizes the dispersion variability with slight variations on the scaling factor, while, at the same time, we can reach sufficiently negative dispersions with lower crosstalk levels. Therefore, we set a_2/a_1 = 0.75 for the final design.

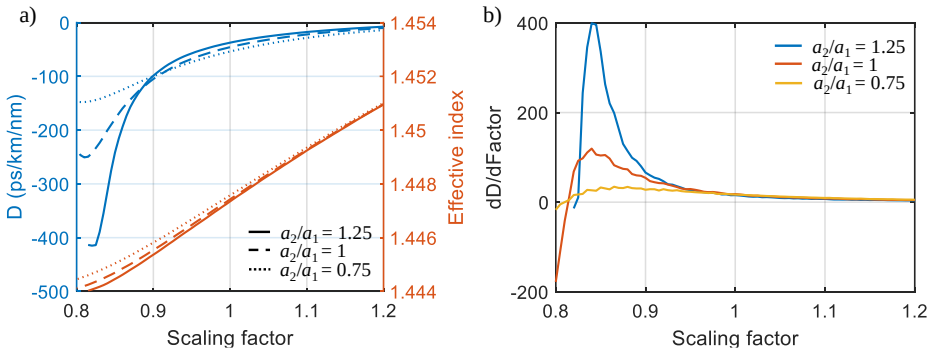

Fig. 6.9. Scale factor dependence of (a) chromatic dispersion D and (b) dD/dFactor for different a_2/a_1 values. The preform parameters are $a_3 = a_1$ and $\Delta_1 = 2.43\%$.

Figure 6.10 shows the dependence of (a) the chromatic dispersion and the effective index n_{eff} and (b) the dispersion slope S with the scale factor. Considering the n_{eff} limit of 1.4450 established earlier, a minimum D of approximately -130 ps/km/nm can be obtained with a scale factor of 0.85 (a_1 = 1.6 μm). The dispersion slope is negative in the whole range of scaling factors that we consider. Therefore, the only remaining design target parameter is the inter-core crosstalk. To obtain a more reliable result, we compute numerically the MCC by simulating the actual refractive index profile of each core in *Fimmave* software (detailed in Annex AI). The electromagnetic fields obtained with the finite element method (FEM) simulation are extracted and processed. The average inter-core crosstalk is calculated with the MCC computed in the previous step and by CPT with Eqs. (2.6)-(2.8).

The final scaling factor in each design is chosen simply by ensuring that the crosstalk level at 1550 nm is below -30 dB/km at the bending radius of 70 mm. The MCCs calculated with the FEM simulation are higher than those derived from the analytical approximation. This further limit the attainable dispersion that can be obtained, especially in the homogeneous case. In contrast, a heterogeneous design with two types of cores can be realized to present lower crosstalk and dispersion than their homogeneous counterpart. The first core type is selected to provide the maximum negative dispersion and the second core type sets the effective index difference (Δn_{eff}). Table 6.4 summarizes the main parameters of the final designed cores along with their most important propagation characteristics.

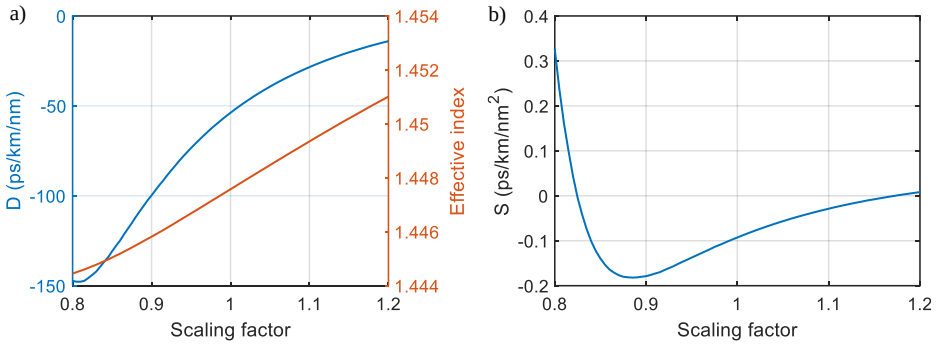

Fig. 6.10. Final preform scaling factor dependence of (a) the dispersion D and (b) the dispersion slope S. The preform parameters are a_3/a_1 = 1, a_2/a_1 = 0.75 and Δ_1 = 2.43%.

Table 6.4. Core design parameters for the homogeneous and heterogeneous case. Optical propagation characteristics calculated at 1550 nm.

Core type	Scaling factor	a_2/a_1	a_3/a_1	D (ps/km/nm)	n_{eff}	S (ps/km/nm^2)	A_{eff}
Homogeneous	0.925	0.75	1.00	-83.7	1.4463	-0.1729	18.2
Heterogeneous – A	0.86	0.75	1.00	-130.8	1.4450	-0.1396	29.3
Heterogeneous – B	0.96	0.75	1.00	-74.4	1.4466	-0.1375	17.7

Figure 6.11 represents the crosstalk dependence on the bending radius for the homogeneous design (a), and the heterogeneous design (b). In the first case, we can see that crosstalk increases steadily with the bending radius. A correlation length of 50 mm is used to calculate the average crosstalk. We could obtain a core type with a dispersion of -83.7 ps/km/nm and an inter-core crosstalk level of -36.9 dB/km at R_b = 70 mm bending radius. In the second case, two types of cores were obtained (A and B). Core A provides a dispersion of -130.8 ps/km/nm, higher than the homogeneous case. Then, we adjusted the scale factor of core B to obtain a threshold bending radius (R_{pk}) below 70 mm with sufficiently low inter-core crosstalk. Consequently, the dispersion of core B is lower than that of core A but it's quite close to that of the homogeneous case. The effective index difference Δn_{eff} is 1.6 x 10^{-4} which sets the critical bending radius (R_{pk}) to 34.91 mm and falls to -34.6 dB/km at R_b = 70 mm. Contrary to the homogeneous case, crosstalk does not increase with the bending radius after the peak. A negative dispersion slope is obtained for both designs and the effective area has similar values to those on existing DCFs.

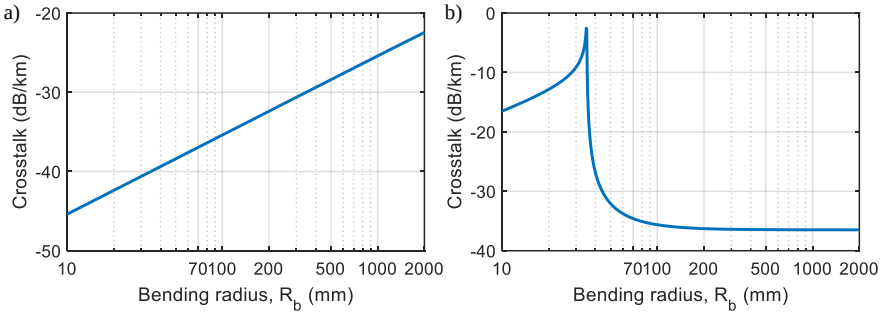

Fig. 6.11. Calculated average inter-core crosstalk at 1550 nm as a function of bending radius for the homogeneous design (a) and the heterogeneous design (b).

In summary we have obtained homogeneous and heterogeneous dispersion-compensation MCF designs. In the homogeneous structure, we obtain moderate negative dispersion whilst in the heterogeneous case a higher dispersion could be reach (at least in one core type). Since probably the transmitting fiber will be a homogeneous MCF, the homogeneous design seems more advantageous because the accumulated dispersion effect on the signal is compensated equally with the same rate in all cores. However, the heterogeneous solution could also be used for instance by rotating alternatively the MCF in each DCF span.

6.4. Pulse repetition rate multiplication (PRRM)

6.4.1. Theoretical background

When a beam of coherent light is transmitted (or reflected) from a periodic 1D or 2D object, one can observe that exact images of that object are reproduced at certain repetitive distances of it. This is known generally as the spatial Talbot effect (named after the first person who reported it in 1836, H.F. Talbot) or self-imaging effect. The temporal equivalent of this effect is known as temporal Talbot effect or temporal self-imaging effect. It is produced when a periodic signal, such as a train of pulses,

propagates through a dispersive medium [135], [136]. Moreover, it is important to note that the shape and energy of the original periodic signal is preserved. For that reason, Jannson and Jannson [137] proposed the exploitation of this phenomenon to transmit information through optical fibers without distortion and established the exact distances at which the Talbot effect occurs. The Talbot length z_T is the distance where an "integer" self-image appears, [138]:

$$z_T = \frac{T_r^2}{2\pi|\beta_2|}, \tag{6.3}$$

where T_r is the pulse repetition period and β_2 is the group velocity dispersion of the medium (also known as the slope of the group delay).

Analogously to the integer case, the fractional Talbot effect is produced at specific distances where the signal reemerges as rate-multiplied images of the initial pulse train. The effect of dispersion redistributes the energy of the initial pulse train in different temporal patterns that are the rate-multiplied replicas of the input pulse train [136]. PRRM is achieved when the right amount of dispersion is applied on a given periodic signal. The fractional self-images appear at the distances given by:

$$z = \frac{s}{m} z_T \ , \tag{6.4}$$

where the integer factor m defines the multiplication factor experienced by the input periodic signal and s is a positive integer mutually prime with m. Here we need to take into account that when the repetition rate is multiplied by m, the intensity of the input signal gets divided by the same factor. This means that when the multiplication factor $m = 2$, the repetition period of the input signal is doubled but its intensity is cut in half. Table 6.5 shows the smallest values of m and s at which the fractional Talbot effect is produced. The column s/m indicates the point where a particular repetition rate multiplication is produced.

Table 6.5. Fractional Talbot effect factorization.

m	*s*	*s/m*
1	1	1
2	1	0.5
3	[1,2]	[0.333, 0.666]
4	[1,3]	[0.25, 0.75]
5	[1,2,3,4]	[0.2, 0.4, 0.6, 0.8]
10	[1,3,7,9]	[0.1, 0.3, 0.7, 0.9]
…	…	

Figure 6.12 represents the evolution of a train of short pulses through a first-order dispersive medium. This representation is also known as Talbot carpet. As we observe, the train of pulses disperses initially and regains its initial temporal position

at s/m = 1. As described previously, the initial signal reappears with a higher repetition rate at the position defined by Eq. (6.4).

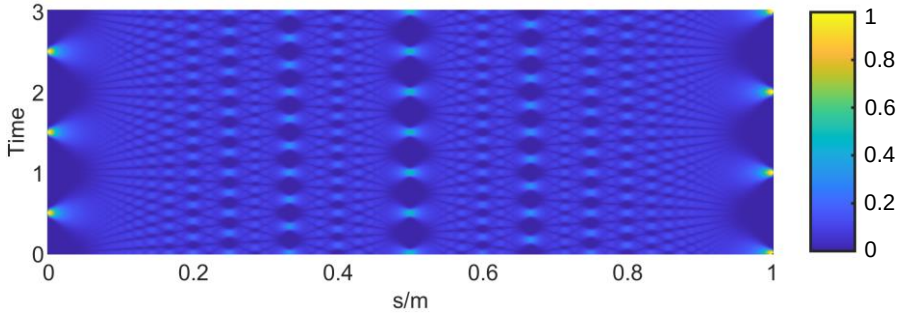

Fig. 6.12. Normalized Talbot carpet representation. Three periods of the initial signal are represented, and propagation distance is normalized to z_T.

As second-order dispersion effects (as in the case of SMFs at 1550 nm) are detrimental to the Talbot phenomena [137], other dispersive media such as linearly chirped fiber Bragg gratings (LCFBGs) have been proposed for PRRM [8], [136]. Likewise, in [139] a combination of LCFBG and DCFs is used to obtain a 128-GHz rate pulse train from a 250-MHz signal (a multiplication factor of 512). In that work, second-order dispersion distortion from the DCF was compensated by a programmable optical filter (*Waveshaper*). Lastly, as the characteristics of the dispersive medium are generally fixed, to obtain a different rate multiplication the period of the input signal is varied instead [8]. However, in [138] they demonstrated that programmable PRRM can be achieved by phase-modulating the input signal with the phase profile of the desired rate-multiplied factor. This last approach, though, is constrained by the performance of the phase profile signal generators that feed the modulator.

In a similar way, we propose to implement temporal Talbot effect through MCFs. In particular, we envisioned that a fiber with multiple dispersion values, such as a dispersion-tailored MCF, could be useful as it would bring some flexibility to choose a particular Talbot condition. Therefore, we look into an MCF design that could achieve this.

6.4.2. MCF design for PRRM

Now, since the amount of chromatic dispersion is key to implement the Talbot effect, we can obtain parallel PRRM by tailoring the chromatic dispersion of each core. For instance, one core could be assigned to generate the integer Talbot effect, so that the initial signal arises at the fiber output, while the other cores could provide PRRM at the fiber output with a different rate. The required chromatic dispersion to get a specific m rate-multiplication can be expressed as (after converting β_2 in Eq. (6.3) to the equivalent D value):

$$D_m = \frac{s}{m} D_1, \tag{6.5}$$

where D_1 is the necessary chromatic dispersion for the integer Talbot effect case. Note that, attending to Eq. (6.3), D_1 (and so D_m) could be either positive or negative. Considering the particular case in which a train of pulses with T_r = 100 ps (f_r = 10 GHz) and z_T = 10 km, the required $|D_1|$ equals 124.78 ps/km/nm. In solid core fibers, this chromatic dispersion value can only be reached with normal (negative) dispersion fiber designs.

As the dispersion D_1 can be obtained with the preform designed in the previous section, we use that same preform here. To obtain PRRM, the remaining cores must have a certain dispersion D_m (dictated by Eq. (6.4)). The main design targets then the chromatic dispersion of each core and the Δn_{eff} (to avoid inter-core crosstalk issues). Additionally, the chromatic dispersion slope (S) should be as low as possible to avoid second-order dispersion distortion [137].

From Fig. 6.10(a) we see that for a scale factor of 0.855, the chromatic dispersion decreases to -124.78 ps/km/nm, which was the value required for the integer Talbot effect described above. Then, by scaling up the preform, different PRRM cores can be obtained by choosing the scaling factor that provides the adequate chromatic dispersion values. Table 6.6 contains the required dispersion D_m to get factor m rate multiplication and the corresponding scaling factor of the preform, together with the associated main core optical properties. Due to the Talbot effect quadratic dependence on the repetition rate (Eq. (6.3)), the designed cores are chosen to provide $m = 2^n$ multiplication factor (n = 0, 1, 2, 3, …) at the MCF output. This brings some advantages on the scalability of the design, since, for instance, halving the length of the link doubles the multiplication factor (for the input signal). Here, it is important to take into account that when $m > 2$, there are several alternatives for s. However, higher dispersion is required when $s > 1$, causing greater pulse broadening, so we generally prefer to select the case s = 1.

Table 6.6. Preform scaling options to obtain PRRM. The main optical properties (D, n_{eff}, S, A_{eff}) of the corresponding cores are listed. Rows in bold indicate candidate cores for an MCF design.

Fractional Talbot effect factors			**Core optical properties**			
m	s	Required D (ps/km/nm)	Scale factor	n_{eff}	S (ps/km/nm^2)	A_{eff} (μm^2)
1	**1**	-124.78	0.855	**1.4452**	-0.1640	24.10
2	**1**	-62.39	0.974	**1.4472**	-0.1140	15.64
3	1	-41.59	1.040	1.4484	-0.0594	14.69
3	2	-83.26	0.925	1.4463	-0.1563	17.64
4	**1**	-31.20	1.084	**1.4492**	-0.0376	14.38
4	3	-93.59	0.910	1.4460	-0.1670	18.39
8	**1**	-15.56	1.185	**1.4508**	0.0042	14.30
16	**1**	-7.80	1.265	**1.4521**	0.0243	14.57
32	**1**	-3.90	1.321	**1.4528**	0.0336	14.80
64	**1**	-1.95	1.360	**1.4535**	0.0390	15.00

From Table 6.6 we select seven cores to realize a 7-core fiber (cores in bold in Table 6.6). Fig. 6.13(a) shows the core arrangement of the MCF designed. Cores are numbered in ascending order with its corresponding multiplication factor *m*. The position of the outer cores is chosen to minimize inter-core crosstalk by interleaving cores with the highest and the lowest n_{eff}. The core for $m = 8$ is chosen as the central core to maximize the Δn_{eff} with the outer cores. The worst case Δn_{eff} between neighboring cores is $1.3 \cdot 10^{-3}$. Fig. 6.13(b) displays the average inter-core crosstalk at 1550 nm, calculated by computing the MCC as shown in Annex I and with Eqs. (2.6) -(2.8)), between cores 4-5 (the ones with the lowest Δn_{eff}). The critical bending radius (R_{pk}) is 34.43 mm for this fiber and the core pitch is 30 μm. A low inter-core crosstalk is obtained in this design because most of the cores are generally well confined.

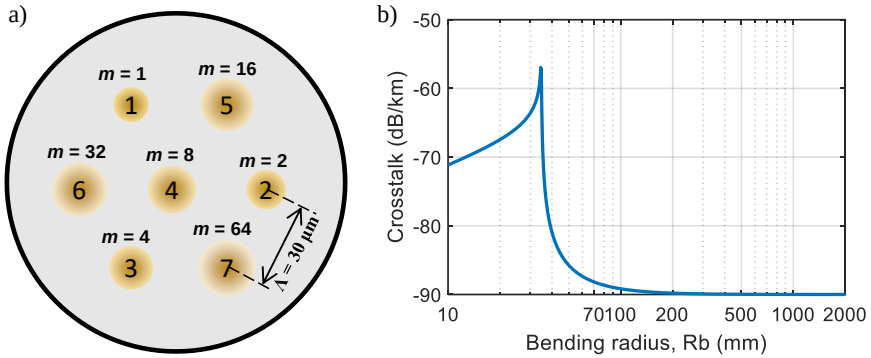

Fig. 6.13. (a) Core arrangement in the designed MCF. (b) Crosstalk dependence with the bending radius R_b for cores 4 and 5.

6.4.3. Pulse repetition rate multiplication simulation

We have obtained a MCF design with a different rate-multiplication factor in each core. Now, we simulate the propagation of a periodic signal through each one of the cores. The input signal is Fourier-transformed into the frequency domain and then is linearly propagated [140]. We take into account the specific first-order and second-order dispersion of each core (from Table 6.6). Optical losses are neglected in these simulations. The input signal comprises 1-ps-FWHM-width Gaussian pulses with an initial repetition rate of 100 ps (f_r =10 GHz).

Figure 6.14 gathers the simulation results after propagation through each core of the designed MCF. It shows that the output signals are rate-multiplied correctly, since based on the pulses' position, the output signals experience the intended Talbot effect. In the first case ($m = 1$), the output signal shows the same input signal with a temporal shift of half a period. In the rest of cores, the repetition rate is multiplied by *m*. However, severe second-order dispersion distortion appears at the output of cores 1-2. Small sub-pulses emerge next to the main pulse due to this (which depend on the magnitude and sign of *S* [140]). In this regard, cores 3-5 present little to no distortion (negligible in the case of core 4). In the last two cores (6 and 7), the main distortion comes from temporal overlapping between the individual pulses. Temporal overlapping is originated by pulse broadening while intensity fluctuations are caused

by second-order dispersion. To reduce this effect, we look for another possibility in which the Talbot condition is achieved with a shorter fiber length.

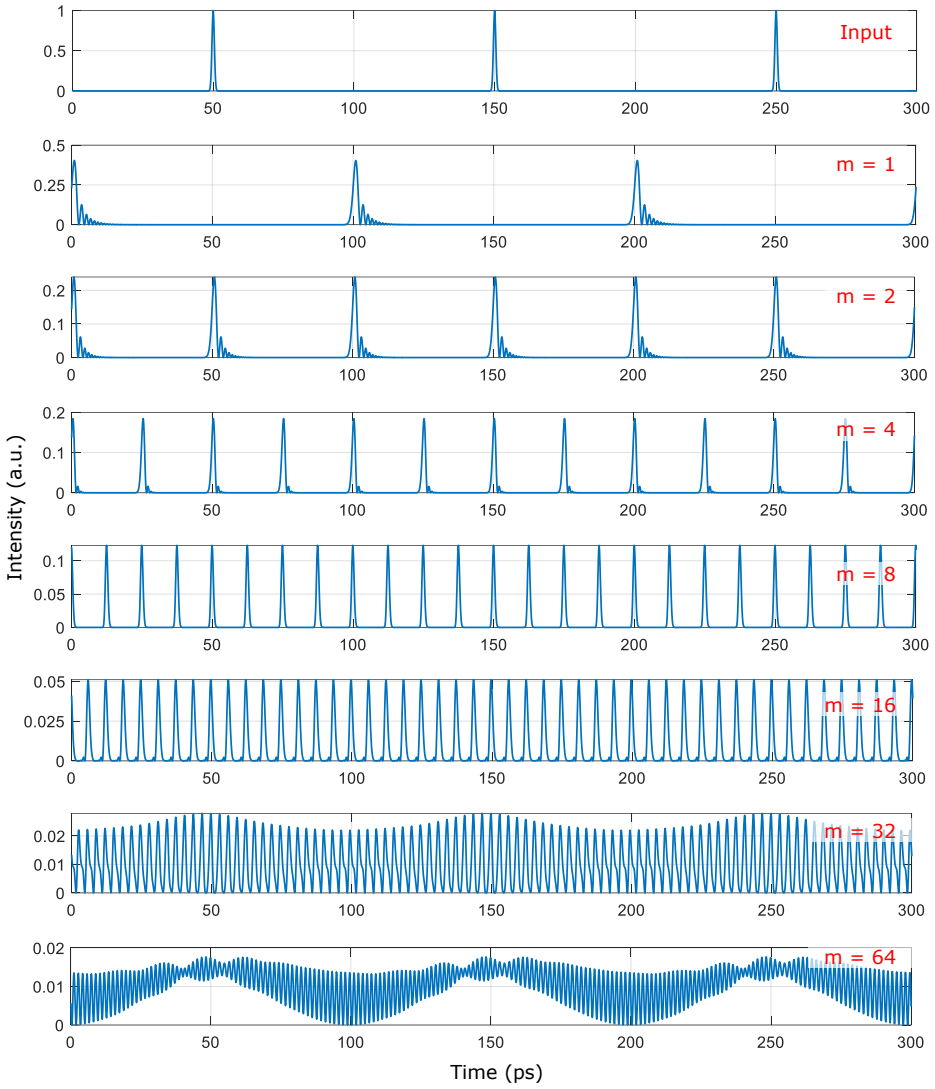

Fig. 6.14. The 10-GHz-repetition-rate input signal and the output signals after being propagated through a 10-km dispersive medium with the optical parameters listed in Table 6.6.

Figure 6.15 represents the output train of pulses when the fiber length is reduced to 2.5 km. As stated before, this is done to limit the impact of second-order dispersion. In comparison with the previous case, the pulse width is kept at 1 ps and f_r doubles to 20 GHz to keep the same multiplication factors. As a result of reducing the propagation length, second-order dispersion distortion have less effect on the pulse shape as compared to the previous case (only visible in the first two cores). Accordingly, the central cores (3-5) show no distortion at all as the dispersion slope

is small. On the other hand, the last two cores present an even higher temporal overlapping as the inter-pulse width is now half the initial value. A solution to this could be reducing the pulse width, but that would also enhance pulse broadening which increases with the bandwidth of the signal [140]. Second-order distortion would also increase as well.

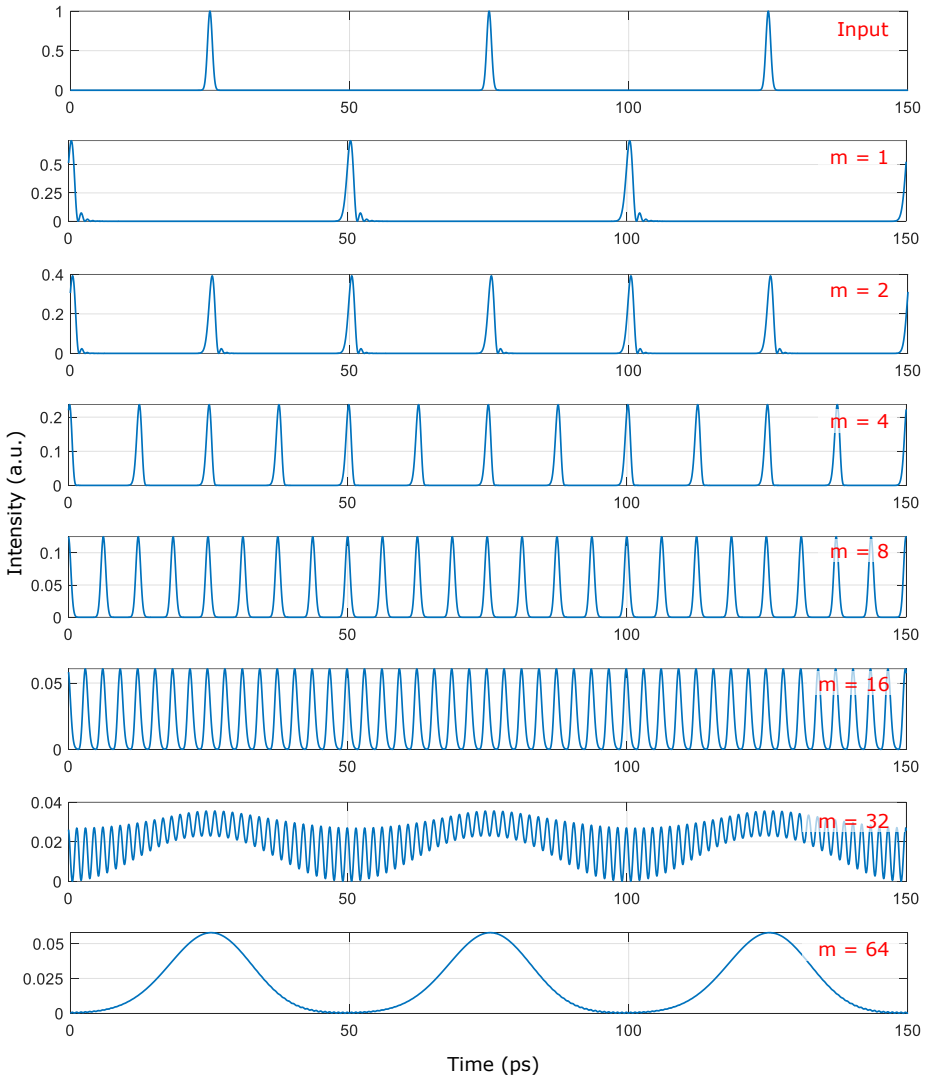

Fig. 6.15. The 20-GHz repetition-rate input signal and the output signals after being propagated through a 2.5-km dispersive medium with the optical parameters listed in Table 6.6.

To conclude, we have explored the possibility of designing an MCF for PRRM with several multiplication factors using the preform scaling preform technique. We obtained a design with quadratic-scaling multiplication factors up to 64. We note that quadratic-scaling factors provide a better solution compared to arbitrary factors as

the Talbot effect depends intrinsically on the fiber length and the input signal characteristics. This means, for instance, that halving the length doubles the multiplication factor for a particular case. A similar logic applies in the case of the input signal repetition rate. Then, after verifying PRRM performance on this MCF design through simulation, we conclude that the maximum multiplication factor we can reach without distortion is 16. Pulse broadening introduced by first- and second-order dispersions limits the maximum multiplication factor that can be achieved. To solve dispersion slope distortion, one can look for a dedicated MCF design (i.e., an individual preform per core) or employ another type of fiber with flat dispersion such as a photonic crystal fiber [141]. Another alternative would be to compensate the distortion using an optical filter as in [139].

6.5. Conclusions

In this chapter, we have explored different applications in which a specific heterogeneous MCF design is required. The multiplicity of optical spatial paths is exploited to bring more capacity (QKD), a necessary optical fiber network building block (dispersion compensation) or pulse repetition-rate scalability (PRRM).

In the first case, we design an ultra-low crosstalk heterogeneous MCF with three types of cores. Then, we compare existing homogeneous MCFs and a customized ultra-low crosstalk heterogeneous MCF as the transmission media for classical channels and QKD channels in the same fiber. The results indicate that the heterogeneous design can support QKD channels in the presence of classical channels, even in the worst-case scenario (a central core surrounded by six transmitting cores) up to 80-km transmission distance.

In the second case, we have presented the design of two specific MCFs to enable passive dispersion compensation in standard 125-μm-cladding-diameter 4-core MCFs with a core pitch of 40 μm. We have proposed a homogeneous design with a negative dispersion of D = -83.7 ps/km/nm in all the cores. Alternatively, we also designed a heterogeneous 4-core MCF with two types of cores in which the core chromatic dispersions are -130.8 and -74.4 ps/km/nm, respectively. Both designs feature inter-core crosstalk levels below -34.6 dB/km (at 1550 nm for R_b = 70 mm).

Lastly, we designed a 7-core heterogeneous MCF in which the dispersion of each core is tailored to provide parallel Talbot self-images for the integer and fractional cases. The designed MCF provides PRRM with a multiplication factor that scales quadratically from 2 to 64. The simulation results imply that dispersion-induced distortion (pulse broadening and distortion) limits the multiplication factors that could be obtained effectively. Even so, cores 3-5 could provide a multiplication factor of 4, 8 and 16, respectively, with little to no distortion at the output.

Chapter 7
Conclusions and future work

7.1. Summary and conclusions

In this PhD Thesis, we have reported the design, implementation and validation of fiber-distributed signal processing solutions built upon heterogeneous multicore fibers for both optical and microwave signals. We started validating a custom-designed dispersion-diversity heterogeneous 7-core multicore fiber in terms of TTDL operation. We demonstrated a set of MWP signal processing applications implemented among this fiber and developed a novel dispersion-diversity 19-core heterogeneous MCF that behaves as a tunable sampled TTDL for dispersion-managed signal processing. In addition, we propose the design of different application-specific heterogeneous MCFs for optical signal distribution and processing.

Chapter 2 introduces the fundamentals on which this Thesis is based on. In the first part, we have reviewed the state of the art of multicore fibers, detailing both their modeling and general applications. In the second part, this chapter introduces the Thesis research background, including the topic of Microwave Photonics and the implementation of tunable TTDLs with heterogeneous multicore fibers.

Then, in chapter 3, we characterized a previously fabricated 5-km long dispersion-diversity heterogeneous 7-core MCF that acts as a TTDL. This fiber was fabricated using 7 individual fiber preforms designed to provide specific propagation characteristics. We investigated the performance of the TTDL by measuring insertion losses, inter-core crosstalk, differential group delay and chromatic dispersion over the whole link. In terms of insertion losses and inter-core crosstalk, this fiber does not pose a problem for the implementation of the TTDL. Regarding differential delays, cores 3-5 provide the expected behavior in a 30-nm range for spatial diversity operation. On the other hand, cores 1-2, can be used in a shorter range as were more affected by fabrication inaccuracies. We also investigated the stability of the group delay where we observed fluctuations of less than 1 ps in a 2-hour period.

In line with the group delay temporal stability, in chapter 3 we also investigated the detrimental impact introduced by temperature changes. We measured the DGD between the outer fiber cores when the temperature is varied in a climatic chamber.

The observed DGD fluctuations were less than 1 ps/ºC. Moreover, we investigated the adverse effects introduced by fiber bending and twisting on the performance of the TTDL. We theoretically and experimentally evaluated how fiber bending induces group delay variations between the outer cores of an MCF. We obtained analytical expressions for calculating the accumulated DGD on a given fiber length for a constant twist rate. Although a big impact on the DGD is obtained because of bends, we observed that the effect of twisting counteracts it. We experimentally demonstrated this by measuring the DGD of a 7-core MCF in different twist conditions, observing considerable fluctuations that would distort the TTDL performance. Nonetheless, we concluded that this detrimental effect is fixed and can be compensated once the fiber has been deployed.

In chapter 4, we experimentally demonstrated several MWP signal processing functionalities implemented with the fiber characterized in the chapter 3. First, we achieved reconfigurable RF signal filtering in the spatial- and wavelength-diversity domains. In the spatial-diversity domain, the filter response is varied by moving the operation wavelength, while in the wavelength domain, is adjusted by changing the optical carrier separation. Then, we demonstrated optical beamforming for phased array antennas in a real-antenna implementation. We measured the radiation pattern of a PAA in iTEAM's anechoic chamber, where we observed how the beam could be steered in a continuous way by tuning the optical wavelength. Finally, we demonstrated arbitrary waveform generation with an incoherent balanced photodetection scheme. Ultra-wideband pulses were generated using a different combination of cores in each case. Besides signal processing, we showed that the MCF could also be used to distribute high-frequency 5G radio signals in parallel along all cores. We found out that crosstalk-induced penalties can limit the transmission of high-bandwidth signals, particularly in the central core, where crosstalk levels are higher than in the rest of cores. Overall, parallel channels can be distributed independently in most cases.

Chapter 5 gathers the full design and fabrication of a heterogeneous 19-core MCF developed to operate as a 15-sample TTDL. The novelty lies in the fact that three fiber preforms, each with a different refractive index profile, are scaled down to obtain the required chromatic dispersion properties in all the cores. Starting from a preliminary design, we adapted it after evaluating the fabricated preforms. The preforms were characterized by drawing single-core test fibers to gain information on how to scale the preforms properly to obtain the required chromatic dispersion, and by contrasting this with the simulation of the refractive index profile of the single-core test fibers and preforms. A first trial fiber was fabricated at Max Planck Institute for the Science of Light during my stay there. Unfortunately, more time is required to overcome some problems derived from fabrication and fully characterize the full behavior of this preliminary fiber as a TTDL.

Lastly, chapter 6 deals with the proposal of three heterogeneous multicore fiber designs for QKD, dispersion compensation and parallel temporal Talbot effects. First, we investigated the feasibility of coexisting traditional data with QKD channels in the same fiber considering both homogeneous MCFs and a heterogeneous ultralow-crosstalk MCF. The latter would enable the simultaneous transmission of quantum

keys and traditional data in the same fiber (and at the same optical wavelength). Second, we propose the concept of a dispersion-compensation MCF to counteract the effect of different chromatic dispersions in parallel on future MCF transmission networks. Following the current trend, we designed both homogeneous and heterogeneous four-core fibers with the standard cladding diameter for standard SMFs. Last, we introduced the concept of parallel temporal Talbot effects. For that, we obtained a 7-core MCF design with specific chromatic dispersion in each core aimed for pulse repetition rate multiplication. For a fixed repetition rate, the MCF provides 7 different multiplication factors. We studied the performance of this fiber in achieving PRRM by simulating the propagation of a train of gaussian pulses in each core of the fiber.

7.2. Future work

We would like to propose additional lines of work in the field of fiber-distributed signal processing:

- The characterization and fabrication of the 19-core MCF, and the experimental demonstration of distributed signal processing functionalities built upon it. Unfortunately, we have not been able to characterize the first fabricated 19-core MCF fully. We do not know if the fabrication procedure successfully obtained the required propagation characteristics for TTDL operation. Up to date, we found out the fiber has high optical propagation losses and a couple of defects that interrupt light propagation. After removing the defects, the fiber can be characterized by measuring for instance the chromatic dispersion with the CSE method [93]. With that information, the design can be readjusted if necessary, as shown in chapter 5, and thus proceed with a second fabrication round.

- The implementation and experimental demonstration of additional MWP functionalities built upon TTDL MCFs. In chapter 4 we demonstrated the implementation of signal filtering, optical beamforming and arbitrary waveform generation. The latter was demonstrated by choosing specific amplitude weights for UWB pulse generation. However, a more general approach can be realized to obtain temporal differentiation over other types of signals (i.e., time differentiation). Moreover, finite temporal integration can be realized by combining the delayed-temporal samples generated by the TTDL. Lastly, time-interleaved analog-to-digital conversion is another field of application where the TTDL could be applied.

- The development of a specific device for the monitoring and dynamic control of the group delays at the anchor wavelength. Until now, our experiments have been conducted in laboratories where we have major control over the transmission link. Yet, in practice, we must face several challenges regarding time-delay performance stability in distributed signal processing systems. As we saw in chapter 3, the differential time delay between cores is susceptible to change because of temperature fluctuations as well as fiber bending and twisting effects. A significant temperature variation could cause a detrimental impact on the performance of the TTDL, for instance, by changing the beam-pointing angle

of a phased array antenna. Therefore, developing a tool that monitors this and automatically compensates for the fluctuation would be welcomed.

- The experimental demonstration of 2D beamforming using the spatial and wavelength diversities simultaneously. In this Thesis, we have demonstrated optical beamforming for a linear antenna array employing the spatial-diversity domain. The time-delayed signals are detected individually and fed a given antenna element in a one-dimension array. This can also be implemented with the wavelength diversity by demultiplexing each wavelength-multiplexed sample separately. Considering a *N*x*M* antenna array, it could be fed by employing an array of *M* lasers in each core of a *N*-core MCF.

- The experimental demonstration of parallel temporal Talbot effects implemented by a single multicore fiber. A typical constraint in such demonstrations is that the required accumulated chromatic dispersion is fixed for a particular signal repetition rate at the input. Adapting to another input signal with a different rate (or to another Talbot phenomenon output) is achieved by varying the fiber length or using another optical device. An MCF with specific dispersion coefficients would provide multiple different dispersion coefficients under the same link length. Therefore, several multiplication factors can be demonstrated with the same fiber length, or the same Talbot condition can be achieved for different repetition-rate input signals.

- The fabrication and experimental demonstration of parallel dispersion compensation. As stated in chapter 6, a low crosstalk MCF with negative dispersion cores could be fabricated to work like conventional DCFs in current fiber-optic communication systems. The fabrication of the MCF would require the use of a single fiber preform.

Annex I
Mode-coupling coefficients

AI.1. Mode-coupling coefficients (MCCs) for SI and TA-SI cores

As we saw in Chapter 2, the inter-core crosstalk of an MCF can be calculated by using Eq. (2.2), which is the general expression for the MCC of two cores. Particularizing for a couple of step-index cores, it is expressed as in [128]:

$$\kappa_{pq} = \frac{\omega\varepsilon_0}{4P_p}\int_0^{2\pi}\int_0^{a_{1,p}} (n_p^2 - n_{cl}^2)\boldsymbol{E}_{\boldsymbol{p}}^{*}\cdot\boldsymbol{E}_{\boldsymbol{q}} r dr d\theta\,, \tag{AI.1}$$

being ω the angular frequency, ε_0 the electric permeability in vacuum, n_p the refractive index distribution inside core p, n_{cl} the refractive index of the cladding, **E** and **H** the normalized vector fields of the electric and magnetic fields of each mode, and * indicates the complex conjugate and where P_p is the portion of power traversing core p cross-section:

$$P_p = \frac{1}{2}\int_{-\infty}^{+\infty}\int_{-\infty}^{+\infty}\left(\boldsymbol{E}_{\boldsymbol{p}}^{*}\times\boldsymbol{E}_{\boldsymbol{q}}\right)\cdot\hat{z}dxdy. \tag{AI.2}$$

Several analytical expressions have been derived to calculate the MCC of homogeneous SI cores [37] and TA-SI cores [142]; and heterogenous SI cores [143]–[147] and TA-SI cores [128]. Table AI.1 classifies some of the analytical expressions that can be found in literature based on the refractive index profile that can be applied to and the core homogeneity (i.e., whether it can be used for homogeneous or heterogeneous cores).

Here the term (n_p^2-n_{cl}^2) in Eq. (AI.1) is only valid for step-index cores. Numerical integration is required when at least one of the cores involved has a different refractive index profile, such as a graded-index or a triangular index core.

Table AI.1. Analytical expressions to calculate the MCC between a couple of cores.

Reference	Year of publication	Core refractive index profile	Core homogeneity
[37]	1972	SI	Homogeneous
[142]	2014	TA-SI	Homogeneous
[143]	2012	SI	Heterogeneous
[144]	2015	SI	Heterogeneous
[145]	2016	SI	Heterogeneous
[146]	2019	SI	Heterogeneous
[147]	2021	SI	Heterogeneous
[128]	2012	TA-SI	Heterogeneous

AI.2. MCC calculation for arbitrary-index profile cores

This section describes the calculation of the MCC of two cores with an arbitrary refractive index profile. First, the refractive index profile of the two cores involved is created in the optical simulation software *Photon Design - Fimmwave*. Fig. AI.1 represents the cross-section of two homogeneous cores. Then, the modes in each core are solved by Finite Element Method (FEM). The electromagnetic fields are exported to MATLAB to compute the MCC. The electromagnetic field components (E_x, E_y, E_z, H_x, H_y, H_z) are filtered in the equivalent area where the other core is located (indicated as a red dashed circle in Fig. AI.1 in each case) [38], [128]. Then, Eq. (AI.1) is solved numerically with the filtered fields. The refractive index of the core is considered in this step. Fig. AI.2 compares the core pitch dependence of the calculated MCC, obtained analytically from the expression in reference [142] and [128], respectively, and the one calculated numerically for the cores represented in Fig. AI.1. We observe that the numerical calculation matches well with the analytical expression from Ye et al. [142] (yellow dotted line). The expression from Tu et. al [128], is also solved numerically as it is non-integrable.

The presented calculation method permits obtaining the MCC between cores with dissimilar refractive index profile (e.g., between SI and TI profile cores), when an analytical expression is not available. This is crucial to estimate the crosstalk in MCF with different types of cores, as is the case in Chapter 5 and 6.

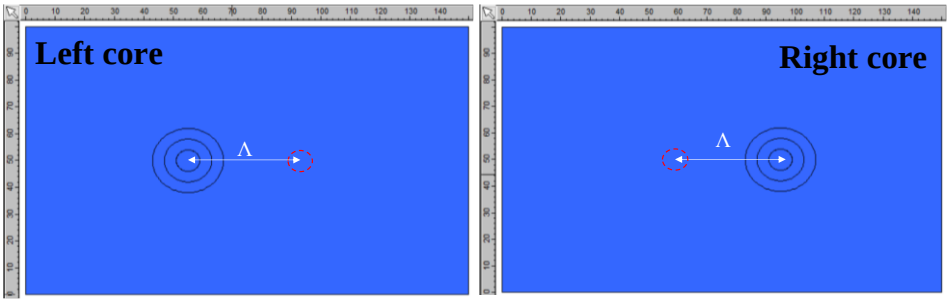

Fig. AI.1. Screenshots taken from Fimmwave design window showing the cross section of the right and left cores. The integration area is indicated in red dashed line.

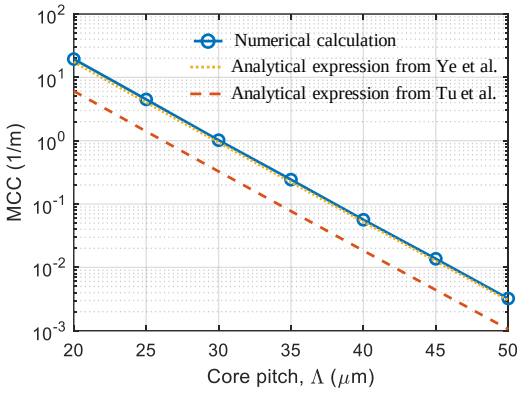

Fig. AI.2. Calculated MCC dependence on core pitch for a couple of homogeneous TA-SI cores with a3 = a2 = a1 = 4 μm and 4% n1 dopant concentration at 1550 nm. Blue circle markers represent the simulation, the solid line is the trendline, the dashed line is the calculation with the heterogeneous analytical expression from [128] and the dotted line is the calculation with the homogeneous analytical expression from [142].

List of Publications

Peer-reviewed international Journal publications

[J1] **M. Ureña**, I. Gasulla, F. J. Fraile, and J. Capmany, "Modeling optical fiber space division multiplexed quantum key distribution systems," *Opt. Express* vol. 27, pp. 7047-7063, 2019.

[J2] S. García, **M. Ureña**, and I. Gasulla, "Bending and twisting effects on multicore fiber differential group delay," *Opt. Express*, vol. 27, pp. 31290-31298, 2019.

[J3] S. García, **M. Ureña**, and I. Gasulla, "Dispersion-Diversity Multicore Fiber Signal Processing", *ACS Photonics*, vol. 9, no. 8, pp. 2850-2859, 2022.

[J4] **M. Ureña**, Sergi García, J. I. Herranz, and I. Gasulla, "Experimental demonstration of dispersion-diversity multicore fiber optical beamforming," *Opt. Express*, vol. 30, pp. 32783-32790, 2022.

International Conference publications

[C1] S. García, **M. Ureña**, R. Guillem, and I. Gasulla, "Multicore Fiber Delay Line Performance Against Bending and Twisting Effects," *2018 European Conference on Optical Communication (ECOC)*, Rome, Italy, 2018, pp. 1-3.

[C2] S. García, R. Guillem, **M. Ureña,** and I. Gasulla, "Space-Division Multiplexing for Microwave Photonics," *2019 24th OptoElectronics and Communications Conference (OECC) and 2019 International Conference on Photonics in Switching and Computing (PSC)*, Fukuoka, Japan, 2019, pp. 1-3. (Invited)

[C3] S. García, **M. Ureña,** and I. Gasulla, "Demonstration of distributed radiofrequency signal processing on heterogeneous multicore fibres," *45th European Conference on Optical Communication (ECOC 2019)*, Dublin, Ireland, 2019, pp. 1-4.

[C4] S. García, **M. Ureña,** and I. Gasulla, "Heterogeneous multicore fiber for optical beamforming," *2019 International Topical Meeting on Microwave Photonics (MWP)*, Ottawa, ON, Canada, 2019, pp. 1-4.

[C5] **M. Ureña**, S. García, and I. Gasulla, "Space-Division Multiplexing Fibers for Microwave Signal Processing," *2020 Conference on Lasers and Electro-Optics (CLEO)*, San Jose, CA, USA, 2020, pp. 1-2. (Invited)

[C6] S. García, R. Guillem, **M. Ureña,** and I. Gasulla, "Space-Division Multiplexing fibers for radiofrequency signal processing," *2020 IEEE Photonics Society Summer Topicals Meeting Series (SUM)*, Cabo San Lucas, Mexico, 2020, pp. 1-2. (Invited)

[C7] **M. Ureña** et al., "Specialty fibers exploiting spatial multiplexing for signal processing in radio access networks," *2021 International Conference on Optical Network Design and Modeling (ONDM)*, Gothenburg, Sweden, 2021, pp. 1-3. (Invited)

[C8] **M. Ureña**, S. García, J. I. Herranz and, I. Gasulla, "Experimental Demonstration of Optical Beamforming on a Dispersion-Engineered Heterogeneous Multicore Fiber," *2022 Conference on Lasers and Electro-Optics (CLEO)*, San Jose, CA, USA, 2022, pp. 1-2.

[C9] **M. Ureña**, S. García, and I. Gasulla, "Ultra-Wideband Pulse Generation Based on Dispersion-Diversity Multicore Fiber," *2023 Optical Fiber Communication Conference (OFC)*, San Diego, CA, USA, 2023, pp. 1-2.

References

[1] D. J. Richardson, J. M. Fini, and L. E. Nelson, “Space-division multiplexing in optical fibres,” *Nature Photonics*, vol. 7, no. 5, pp. 354–362, May 2013, doi: 10.1038/nphoton.2013.94.

[2] W. Klaus, P. J. Winzer, and K. Nakajima, “The Role of Parallelism in the Evolution of Optical Fiber Communication Systems,” *Proceedings of the IEEE*, vol. 110, no. 11, pp. 1619–1654, Nov. 2022, doi: 10.1109/JPROC.2022.3207920.

[3] B. J. Puttnam, G. Rademacher, and R. S. Luís, “Space-division multiplexing for optical fiber communications,” *Optica, OPTICA*, vol. 8, no. 9, pp. 1186–1203, Sep. 2021, doi: 10.1364/OPTICA.427631.

[4] Y. Liu, L. Ma, C. Yang, W. Tong, and Z. He, “Multimode and single-mode fiber compatible graded-index multicore fiber for high density optical interconnect application,” *Opt. Express, OE*, vol. 26, no. 9, pp. 11639–11648, Apr. 2018, doi: 10.1364/OE.26.011639.

[5] F. Lei, D. Dong, X. Liao, and J. Duato, “Bundlefly: a low-diameter topology for multicore fiber,” in *Proceedings of the 34th ACM International Conference on Supercomputing*, in ICS ’20. New York, NY, USA: Association for Computing Machinery, Jun. 2020, pp. 1–11. doi: 10.1145/3392717.3392747.

[6] G. B. Xavier and G. Lima, “Quantum information processing with space-division multiplexing optical fibres,” *Commun Phys*, vol. 3, no. 1, Art. no. 1, Jan. 2020, doi: 10.1038/s42005-019-0269-7.

[7] S. Rommel, D. Perez-Galacho, J. M. Fabrega, R. Muñoz, S. Sales, and I. Tafur Monroy, “High-Capacity 5G Fronthaul Networks Based on Optical Space Division Multiplexing,” *IEEE Transactions on Broadcasting*, vol. 65, no. 2, pp. 434–443, Jun. 2019, doi: 10.1109/TBC.2019.2901412.

[8] J. Azana and M. A. Muriel, “Temporal self-imaging effects: theory and application for multiplying pulse repetition rates,” *IEEE Journal of Selected Topics in Quantum Electronics*, vol. 7, no. 4, pp. 728–744, Jul. 2001, doi: 10.1109/2944.974245.

[9] J. Capmany, J. Mora, I. Gasulla, J. Sancho, J. Lloret, and S. Sales, “Microwave Photonic Signal Processing,” *Journal of Lightwave Technology*, vol. 31, no. 4, pp. 571–586, Feb. 2013, doi: 10.1109/JLT.2012.2222348.

[10] I. Gasulla and J. Capmany, "Microwave Photonics Applications of Multicore Fibers," *IEEE Photonics Journal*, vol. 4, no. 3, pp. 877–888, Jun. 2012, doi: 10.1109/JPHOT.2012.2199101.

[11] S. García and I. Gasulla, "Design of heterogeneous multicore fibers as sampled true-time delay lines," *Opt. Lett., OL*, vol. 40, no. 4, pp. 621–624, Feb. 2015, doi: 10.1364/OL.40.000621.

[12] A. J. Seeds, "Microwave photonics," *IEEE Transactions on Microwave Theory and Techniques*, vol. 50, no. 3, pp. 877–887, Mar. 2002, doi: 10.1109/22.989971.

[13] J. Yao, "Microwave Photonics," *J. Lightwave Technol., JLT*, vol. 27, no. 3, pp. 314–335, Feb. 2009.

[14] M. Agiwal, A. Roy, and N. Saxena, "Next Generation 5G Wireless Networks: A Comprehensive Survey," *IEEE Communications Surveys & Tutorials*, vol. 18, no. 3, pp. 1617–1655, 2016, doi: 10.1109/COMST.2016.2532458.

[15] M. Jaber, M. A. Imran, R. Tafazolli, and A. Tukmanov, "5G Backhaul Challenges and Emerging Research Directions: A Survey," *IEEE Access*, vol. 4, pp. 1743–1766, 2016, doi: 10.1109/ACCESS.2016.2556011.

[16] S. Mattisson, "An Overview of 5G Requirements and Future Wireless Networks: Accommodating Scaling Technology," *IEEE Solid-State Circuits Magazine*, vol. 10, no. 3, pp. 54–60, 2018, doi: 10.1109/MSSC.2018.2844606.

[17] W. Jiang, B. Han, M. A. Habibi, and H. D. Schotten, "The Road Towards 6G: A Comprehensive Survey," *IEEE Open Journal of the Communications Society*, vol. 2, pp. 334–366, 2021, doi: 10.1109/OJCOMS.2021.3057679.

[18] GSMA, "The Mobile Economy 2023," 2023. [Online]. Available: https://www.gsma.com/mobileeconomy/wp-content/uploads/2023/03/270223-The-Mobile-Economy-2023.pdf

[19] X. Lin and N. Lee, Eds., *5G and Beyond*, 1st edition. Springer International Publishing, 2021.

[20] T. Hayashi *et al.*, "Randomly-Coupled Multi-Core Fiber Technology," *Proceedings of the IEEE*, vol. 110, no. 11, pp. 1786–1803, Nov. 2022, doi: 10.1109/JPROC.2022.3182049.

[21] K. Takenaga, S. Tanigawa, N. Guan, S. Matsuo, K. Saitoh, and M. Koshiba, "Reduction of crosstalk by quasi-homogeneous solid multi-core fiber," in *2010 Conference on Optical Fiber Communication (OFC/NFOEC), collocated National Fiber Optic Engineers Conference*, Mar. 2010, pp. 1–3. doi: 10.1364/OFC.2010.OWK7.

[22] T. Hayashi, T. Taru, O. Shimakawa, T. Sasaki, and E. Sasaoka, "Design and fabrication of ultra-low crosstalk and low-loss multi-core fiber," *Opt. Express, OE*, vol. 19, no. 17, pp. 16576–16592, Aug. 2011, doi: 10.1364/OE.19.016576.

[23] T. Sakamoto *et al.*, "Crosstalk suppressed hole-assisted 6-core fiber with cladding diameter of 125 μm," in *39th European Conference and Exhibition on Optical Communication (ECOC 2013)*, Sep. 2013, pp. 1–3. doi: 10.1049/cp.2013.1274.

[24] B. J. Puttnam *et al.*, "2.15 Pb/s transmission using a 22 core homogeneous single-mode multi-core fiber and wideband optical comb," in *2015 European Conference on Optical Communication (ECOC)*, Sep. 2015, pp. 1–3. doi: 10.1109/ECOC.2015.7341685.

[25] M. Koshiba, K. Saitoh, and Y. Kokubun, "Heterogeneous multi-core fibers: proposal and design principle," *IEICE Electron. Express*, vol. 6, no. 2, pp. 98–103, 2009, doi: 10.1587/elex.6.98.

[26] Y. Amma *et al.*, "High-density multicore fiber with heterogeneous core arrangement," in *2015 Optical Fiber Communications Conference and Exhibition (OFC)*, Mar. 2015, pp. 1–3. doi: 10.1364/OFC.2015.Th4C.4.

[27] T. Mizuno *et al.*, "32-core Dense SDM unidirectional transmission of PDM-16QAM signals over 1600 km using crosstalk-managed single-mode heterogeneous multicore transmission line," in *2016 Optical Fiber Communications Conference and Exhibition (OFC)*, Mar. 2016, pp. 1–3.

[28] Y. Kokubun and T. Watanabe, "Dense heterogeneous uncoupled multi-core fiber using 9 types of cores with double cladding structure," in *17th Microopics Conference (MOC)*, Oct. 2011, pp. 1–2.

[29] Y. Sasaki, K. Takenaga, K. Aikawa, Y. Miyamoto, and T. Morioka, "Single-mode 37-core fiber with a cladding diameter of 248 μm," in *2017 Optical Fiber Communications Conference and Exhibition (OFC)*, Mar. 2017, pp. 1–3.

[30] J. Sakaguchi *et al.*, "228-Spatial-Channel Bi-Directional Data Communication System Enabled by 39-Core 3-Mode Fiber," in *2018 European Conference on Optical Communication (ECOC)*, Sep. 2018, pp. 1–3. doi: 10.1109/ECOC.2018.8535206.

[31] T. Matsui, P. L. Pondillo, and K. Nakajima, "Weakly Coupled Multicore Fiber Technology, Deployment, and Systems," *Proceedings of the IEEE*, vol. 110, no. 11, pp. 1772–1785, Nov. 2022, doi: 10.1109/JPROC.2022.3202812.

[32] S. Matsuo *et al.*, "High-Spatial-Multiplicity Multicore Fibers for Future Dense Space-Division-Multiplexing Systems," *J. Lightwave Technol., JLT*, vol. 34, no. 6, pp. 1464–1475, Mar. 2016.

[33] T. Matsui, Y. Sagae, T. Sakamoto, and K. Nakajima, "Design and Applicability of Multi-Core Fibers With Standard Cladding Diameter," *Journal of Lightwave Technology*, vol. 38, no. 21, pp. 6065–6070, Nov. 2020, doi: 10.1109/JLT.2020.3004824.

[34] T. Gonda *et al.*, "Design of Multicore Fiber Having Upgradability From Standard Single-Mode Fibers and Its Application," *Journal of Lightwave Technology*, vol. 37, no. 2, pp. 396–403, Jan. 2019, doi: 10.1109/JLT.2019.2895903.

[35] T. Hayashi, T. Sasaki, and E. Sasaoka, "Behavior of Inter-Core Crosstalk as a Noise and Its Effect on *Q*-Factor in Multi-Core Fiber," *IEICE TRANSACTIONS on Communications*, vol. E97-B, no. 5, pp. 936–944, May 2014.

[36] B. J. Puttnam *et al.*, "Impact of Intercore Crosstalk on the Transmission Distance of QAM Formats in Multicore Fibers," *IEEE Photonics Journal*, vol. 8, no. 2, pp. 1–9, Apr. 2016, doi: 10.1109/JPHOT.2016.2523993.

[37] A. W. Snyder, "Coupled-Mode Theory for Optical Fibers," *J. Opt. Soc. Am., JOSA*, vol. 62, no. 11, pp. 1267–1277, Nov. 1972, doi: 10.1364/JOSA.62.001267.

[38] K. Okamoto, *Fundamentals of Optical Waveguides*, 2nd edition. Academic Press, 2005.

[39] J. M. Fini, B. Zhu, T. F. Taunay, and M. F. Yan, "Statistics of crosstalk in bent multicore fibers," *Opt. Express, OE*, vol. 18, no. 14, pp. 15122–15129, Jul. 2010, doi: 10.1364/OE.18.015122.

[40] D. Marcuse, "Influence of curvature on the losses of doubly clad fibers," *Appl. Opt., AO*, vol. 21, no. 23, pp. 4208–4213, Dec. 1982, doi: 10.1364/AO.21.004208.

[41] M. Koshiba, K. Saitoh, K. Takenaga, and S. Matsuo, "Multi-core fiber design and analysis: coupled-mode theory and coupled-power theory," *Opt. Express, OE*, vol. 19, no. 26, pp. B102–B111, Dec. 2011, doi: 10.1364/OE.19.00B102.

[42] K. Saitoh, "Multi-Core Fiber Technology for SDM: Coupling Mechanisms and Design," *Journal of Lightwave Technology*, vol. 40, no. 5, pp. 1527–1543, Mar. 2022, doi: 10.1109/JLT.2022.3145052.

[43] T. Fujisawa *et al.*, "Crosstalk Analysis of Heterogeneous Multicore Fibers Using Coupled-Mode Theory," *IEEE Photonics Journal*, vol. 9, no. 5, pp. 1–8, Oct. 2017, doi: 10.1109/JPHOT.2017.2749439.

[44] M. Koshiba, K. Saitoh, K. Takenaga, and S. Matsuo, "Analytical Expression of Average Power-Coupling Coefficients for Estimating Intercore Crosstalk

in Multicore Fibers," *IEEE Photonics Journal*, vol. 4, no. 5, pp. 1987–1995, Oct. 2012, doi: 10.1109/JPHOT.2012.2221085.

[45] T. Hayashi, T. Sasaki, E. Sasaoka, K. Saitoh, and M. Koshiba, "Physical interpretation of intercore crosstalk in multicore fiber: effects of macrobend, structure fluctuation, and microbend," *Opt. Express, OE*, vol. 21, no. 5, pp. 5401–5412, Mar. 2013, doi: 10.1364/OE.21.005401.

[46] G. Rademacher *et al.*, "10.66 Peta-Bit/s Transmission over a 38-Core-Three-Mode Fiber," in *2020 Optical Fiber Communications Conference and Exhibition (OFC)*, Mar. 2020, pp. 1–3.

[47] D. Soma *et al.*, "10.16-Peta-bit/s Dense SDM/WDM Transmission over 6-Mode 19-Core Fiber across the C+L Band," *J. Lightwave Technol.*, pp. 1–1, 2018, doi: 10.1109/JLT.2018.2799380.

[48] A. Turukhin *et al.*, "105.1 Tb/s power-efficient transmission over 14,350 km using a 12-core fiber," in *2016 Optical Fiber Communications Conference and Exhibition (OFC)*, Mar. 2016, pp. 1–3.

[49] B. J. Puttnam *et al.*, "0.715 Pb/s Transmission Over 2,009.6 km in 19-Core Cladding Pumped EDFA Amplified MCF Link," in *2019 Optical Fiber Communications Conference and Exhibition (OFC)*, Mar. 2019, pp. 1–3.

[50] S. Jain *et al.*, "32-core erbium/ytterbium-doped multicore fiber amplifier for next generation space-division multiplexed transmission system," *Opt. Express, OE*, vol. 25, no. 26, pp. 32887–32896, Dec. 2017, doi: 10.1364/OE.25.032887.

[51] K. Igarashi *et al.*, "Super-Nyquist-WDM transmission over 7,326-km seven-core fiber with capacity-distance product of 1.03 Exabit/s·km," *Opt. Express, OE*, vol. 22, no. 2, pp. 1220–1228, Jan. 2014, doi: 10.1364/OE.22.001220.

[52] G. Rademacher *et al.*, "Multi-Span Transmission over 65 km 38-Core 3-Mode Fiber," in *2020 European Conference on Optical Communications (ECOC)*, Dec. 2020, pp. 1–4. doi: 10.1109/ECOC48923.2020.9333329.

[53] B. J. Puttnam, R. S. Luís, G. Rademacher, Y. Awaji, and H. Furukawa, "High-Throughput and Long-Distance Transmission With >120 nm S-, C- and L-Band Signal in a 125μm 4-Core Fiber," *Journal of Lightwave Technology*, vol. 40, no. 6, pp. 1633–1639, Mar. 2022, doi: 10.1109/JLT.2021.3128725.

[54] B. J. Puttnam, R. S. Luis, G. Rademacher, Y. Awaji, and H. Furukawa, "1 Pb/s Transmission in a 125μm diameter 4-core MCF," in *2022 Conference on Lasers and Electro-Optics (CLEO)*, May 2022, pp. 1–2.

[55] N. Gisin, G. Ribordy, W. Tittel, and H. Zbinden, "Quantum cryptography," *Rev. Mod. Phys.*, vol. 74, no. 1, pp. 145–195, Mar. 2002, doi: 10.1103/RevModPhys.74.145.

[56] V. Scarani, H. Bechmann-Pasquinucci, N. J. Cerf, M. Dušek, N. Lütkenhaus, and M. Peev, "The security of practical quantum key distribution," *Rev. Mod. Phys.*, vol. 81, no. 3, pp. 1301–1350, Sep. 2009, doi: 10.1103/RevModPhys.81.1301.

[57] A. Ekert and R. Renner, "The ultimate physical limits of privacy," *Nature*, vol. 507, no. 7493, Art. no. 7493, Mar. 2014, doi: 10.1038/nature13132.

[58] M. Lucamarini *et al.*, "Efficient decoy-state quantum key distribution with quantified security," *Opt. Express, OE*, vol. 21, no. 21, pp. 24550–24565, Oct. 2013, doi: 10.1364/OE.21.024550.

[59] Z. L. Yuan, B. E. Kardynal, A. W. Sharpe, and A. J. Shields, "High speed single photon detection in the near infrared," *Appl. Phys. Lett.*, vol. 91, no. 4, p. 041114, Jul. 2007, doi: 10.1063/1.2760135.

[60] M. Sasaki *et al.*, "Field test of quantum key distribution in the Tokyo QKD Network," *Opt. Express, OE*, vol. 19, no. 11, pp. 10387–10409, May 2011, doi: 10.1364/OE.19.010387.

[61] C. Elliott, A. Colvin, D. Pearson, O. Pikalo, J. Schlafer, and H. Yeh, "Current status of the DARPA Quantum Network." arXiv, Mar. 17, 2005. doi: 10.48550/arXiv.quant-ph/0503058.

[62] T.-Y. Chen *et al.*, "Metropolitan all-pass and inter-city quantum communication network," *Opt. Express, OE*, vol. 18, no. 26, pp. 27217–27225, Dec. 2010, doi: 10.1364/OE.18.027217.

[63] B. Fröhlich, J. F. Dynes, M. Lucamarini, A. W. Sharpe, Z. Yuan, and A. J. Shields, "A quantum access network," *Nature*, vol. 501, no. 7465, Art. no. 7465, Sep. 2013, doi: 10.1038/nature12493.

[64] J. F. Dynes *et al.*, "Quantum key distribution over multicore fiber," *Opt. Express, OE*, vol. 24, no. 8, pp. 8081–8087, Apr. 2016, doi: 10.1364/OE.24.008081.

[65] E. Hugues-Salas *et al.*, "11.2 Tb/s Classical Channel Coexistence With DV-QKD Over a 7-Core Multicore Fiber," *Journal of Lightwave Technology*, vol. 38, no. 18, pp. 5064–5070, Sep. 2020, doi: 10.1109/JLT.2020.2998053.

[66] T. A. Eriksson *et al.*, "Crosstalk Impact on Continuous Variable Quantum Key Distribution in Multicore Fiber Transmission," *IEEE Photonics Technology Letters*, vol. 31, no. 6, pp. 467–470, Mar. 2019, doi: 10.1109/LPT.2019.2898458.

[67] C. Cai, Y. Sun, Y. Zhang, P. Zhang, J. Niu, and Y. Ji, "Experimental wavelength-space division multiplexing of quantum key distribution with classical optical communication over multicore fiber," *Opt. Express, OE*, vol. 27, no. 4, pp. 5125–5135, Feb. 2019, doi: 10.1364/OE.27.005125.

[68] D. Bacco *et al.*, "Boosting the secret key rate in a shared quantum and classical fibre communication system," *Commun Phys*, vol. 2, no. 1, Art. no. 1, Nov. 2019, doi: 10.1038/s42005-019-0238-1.

[69] S. Rommel *et al.*, "Towards a Scaleable 5G Fronthaul: Analog Radio-over-Fiber and Space Division Multiplexing," *Journal of Lightwave Technology*, vol. 38, no. 19, pp. 5412–5422, Oct. 2020, doi: 10.1109/JLT.2020.3004416.

[70] M. Morant, A. M. Trinidad, E. Tangdiongga, and R. Llorente, "Multi-core Fiber Technology supporting MIMO and Photonic Beamforming in 5G Multi-Antenna Systems : (Invited paper)," in *2019 International Topical Meeting on Microwave Photonics (MWP)*, Oct. 2019, pp. 1–4. doi: 10.1109/MWP.2019.8892041.

[71] M. Morant, A. Trinidad, E. Tangdiongga, T. Koonen, and R. Llorente, "Multi-Beamforming Provided by Dual-Wavelength True Time Delay PIC and Multicore Fiber," *Journal of Lightwave Technology*, vol. 38, no. 19, pp. 5311–5317, Oct. 2020, doi: 10.1109/JLT.2020.2994536.

[72] C. Vázquez *et al.*, "Multicore Fiber Scenarios Supporting Power Over Fiber in Radio Over Fiber Systems," *IEEE Access*, vol. 7, pp. 158409–158418, 2019, doi: 10.1109/ACCESS.2019.2950599.

[73] J. D. López-Cardona *et al.*, "Power-over-fiber in a 10 km long multicore fiber link within a 5G fronthaul scenario," *Opt. Lett., OL*, vol. 46, no. 21, pp. 5348–5351, Nov. 2021, doi: 10.1364/OL.439105.

[74] H. Yang, S. Wang, D. Peng, Y. Qin, and S. Fu, "Optically powered 5G WDM fronthaul network with weakly-coupled multicore fiber," *Opt. Express, OE*, vol. 30, no. 11, pp. 19795–19804, May 2022, doi: 10.1364/OE.457347.

[75] J. Capmany and D. Novak, "Microwave photonics combines two worlds," *Nature Photonics*, vol. 1, no. 6, pp. 319–330, Jun. 2007, doi: 10.1038/nphoton.2007.89.

[76] D. Novak *et al.*, "Radio-Over-Fiber Technologies for Emerging Wireless Systems," *IEEE Journal of Quantum Electronics*, vol. 52, no. 1, pp. 1–11, Jan. 2016, doi: 10.1109/JQE.2015.2504107.

[77] J. Capmany, B. Ortega, D. Pastor, and S. Sales, "Discrete-time optical Processing of microwave signals," *Journal of Lightwave Technology*, vol. 23, no. 2, pp. 702–723, Feb. 2005, doi: 10.1109/JLT.2004.838819.

[78] R. A. Minasian, "Photonic signal processing of microwave signals," *IEEE Transactions on Microwave Theory and Techniques*, vol. 54, no. 2, pp. 832–846, Feb. 2006, doi: 10.1109/TMTT.2005.863060.

[79] J. Yao and J. Capmany, "Microwave photonics," *Sci. China Inf. Sci.*, vol. 65, no. 12, p. 221401, Dec. 2022, doi: 10.1007/s11432-021-3524-0.

[80] D. Marpaung, J. Yao, and J. Capmany, “Integrated microwave photonics,” *Nature Photon*, vol. 13, no. 2, Art. no. 2, Feb. 2019, doi: 10.1038/s41566-018-0310-5.

[81] D. B. Hunter and R. A. Minasian, “Microwave optical filters using in-fiber Bragg grating arrays,” *IEEE Microwave and Guided Wave Letters*, vol. 6, no. 2, pp. 103-, Feb. 1996, doi: 10.1109/75.482003.

[82] J. Sancho *et al.*, “Integrable microwave filter based on a photonic crystal delay line,” *Nat Commun*, vol. 3, no. 1, Art. no. 1, Sep. 2012, doi: 10.1038/ncomms2092.

[83] K. Wilner and A. P. van den Heuvel, “Fiber-optic delay lines for microwave signal processing,” *Proceedings of the IEEE*, vol. 64, no. 5, pp. 805–807, May 1976, doi: 10.1109/PROC.1976.10216.

[84] J. Xie, L. Zhou, Z. Li, J. Wang, and J. Chen, “Seven-bit reconfigurable optical true time delay line based on silicon integration,” *Opt. Express, OE*, vol. 22, no. 19, pp. 22707–22715, Sep. 2014, doi: 10.1364/OE.22.022707.

[85] I. Gasulla, D. Barrera, J. Hervás, and S. Sales, “Spatial Division Multiplexed Microwave Signal processing by selective grating inscription in homogeneous multicore fibers,” *Sci Rep*, vol. 7, no. 1, Art. no. 1, Jan. 2017, doi: 10.1038/srep41727.

[86] S. García, R. Guillem, J. Madrigal, D. Barrera, S. Sales, and I. Gasulla, “Sampled true time delay line operation by inscription of long period gratings in few-mode fibers,” *Opt. Express, OE*, vol. 27, no. 16, pp. 22787–22793, Aug. 2019, doi: 10.1364/OE.27.022787.

[87] S. Shaheen, I. Gris-Sánchez, and I. Gasulla, “True-Time Delay Line Based on Dispersion-Flattened 19-Core Photonic Crystal Fiber,” *Journal of Lightwave Technology*, vol. 38, no. 22, pp. 6237–6246, Nov. 2020, doi: 10.1109/JLT.2020.3011548.

[88] S. García, R. Guillem, and I. Gasulla, “Ring-core few-mode fiber for tunable true time delay line operation,” *Opt. Express, OE*, vol. 27, no. 22, pp. 31773–31782, Oct. 2019, doi: 10.1364/OE.27.031773.

[89] E. Nazemosadat and I. Gasulla, “Dispersion-tailored few-mode fiber design for tunable microwave photonic signal processing,” *Opt. Express, OE*, vol. 28, no. 24, pp. 37015–37025, Nov. 2020, doi: 10.1364/OE.412830.

[90] S. García, M. Ureña, and I. Gasulla, “Dispersion-Diversity Multicore Fiber Signal Processing,” *ACS Photonics*, vol. 9, no. 8, pp. 2850–2859, Aug. 2022, doi: 10.1021/acsphotonics.2c00910.

[91] S. García Cortijo, "Distributed radiofrequency signal processing based on space-division multiplexing fibers," PhD Thesis, Universitat Politècnica de València, 2020. doi: 10.4995/Thesis/10251/147858.

[92] C. Dorrer, N. Belabas, J.-P. Likforman, and M. Joffre, "Spectral resolution and sampling issues in Fourier-transform spectral interferometry," *J. Opt. Soc. Am. B, JOSAB*, vol. 17, no. 10, pp. 1795–1802, Oct. 2000, doi: 10.1364/JOSAB.17.001795.

[93] R. Hui and M. O'Sullivan, *Fiber Optic Measurement Techniques*, 1st edition. Academic Press, 2009.

[94] P. S. Andre, A. N. Pinto, and J. L. Pinto, "Effect of temperature on the single mode fibers chromatic dispersion," in *Proceedings of the 2003 SBMO/IEEE MTT-S International Microwave and Optoelectronics Conference - IMOC 2003. (Cat. No.03TH8678)*, Sep. 2003, pp. 231–234 vol.1. doi: 10.1109/IMOC.2003.1244863.

[95] T. Kato, Y. Koyano, and M. Nishimura, "Temperature dependence of chromatic dispersion in various types of optical fibers," in *Optical Fiber Communication Conference. Technical Digest Postconference Edition. Trends in Optics and Photonics Vol.37 (IEEE Cat. No. 00CH37079)*, Mar. 2000, pp. 104–106 vol.1. doi: 10.1109/OFC.2000.868384.

[96] A. Hartog, A. J. Conduit, and D. N. Payne, "Variation of pulse delay with stress and temperature in jacketed and unjacketed optical fibres," *Optical and Quantum Electronics*, vol. 11, pp. 265–273, Jan. 1979, doi: 10.1007/BF00620112.

[97] B. J. Puttnam, G. Rademacher, R. S. Luís, J. Sakaguchi, Y. Awaji, and N. Wada, "Inter-Core Skew Measurements in Temperature Controlled Multi-Core Fiber," in *2018 Optical Fiber Communications Conference and Exposition (OFC)*, Mar. 2018, pp. 1–3.

[98] F. Azendorf, A. Dochhan, F. Spinty, M. Lawin, B. Schmauss, and M. Eiselt, "Group Delay Measurements of Multicore Fibers with Correlation Optical Time Domain Reflectometry," in *2020 22nd International Conference on Transparent Optical Networks (ICTON)*, Jul. 2020, pp. 1–4. doi: 10.1109/ICTON51198.2020.9203412.

[99] R. S. Sohanpal *et al.*, "Clock and Data Recovery-Free Data Communications Enabled by Multi-Core Fiber With Low Thermal Sensitivity of Skew," *Journal of Lightwave Technology*, vol. 38, no. 7, pp. 1636–1643, Apr. 2020, doi: 10.1109/JLT.2020.2974319.

[100] B. J. Puttnam *et al.*, "Dynamic Skew Measurements in a Deployed 4-Core Fiber," in *Conference on Lasers and Electro-Optics (2020), paper STu4R.1*,

Optical Society of America, May 2020, p. STu4R.1. doi: 10.1364/CLEO_SI.2020.STu4R.1.

[101] R. T. Schermer and J. H. Cole, "Improved Bend Loss Formula Verified for Optical Fiber by Simulation and Experiment," *IEEE Journal of Quantum Electronics*, vol. 43, no. 10, pp. 899–909, Oct. 2007, doi: 10.1109/JQE.2007.903364.

[102] S. García, M. Ureña, and I. Gasulla, "Bending and twisting effects on multicore fiber differential group delay," *Opt. Express, OE*, vol. 27, no. 22, pp. 31290–31298, Oct. 2019, doi: 10.1364/OE.27.031290.

[103] J. Capmany, B. Ortega, and D. Pastor, "A tutorial on microwave photonic filters," *Journal of Lightwave Technology*, vol. 24, no. 1, pp. 201–229, Jan. 2006, doi: 10.1109/JLT.2005.860478.

[104] F. Grassi, J. Mora, B. Ortega, and J. Capmany, "Subcarrier multiplexing tolerant dispersion transmission system employing optical broadband sources," *Opt. Express, OE*, vol. 17, no. 6, pp. 4740–4751, Mar. 2009, doi: 10.1364/OE.17.004740.

[105] M. Sagues and A. Loayssa, "Optical beamforming for phased array antennas using stimulated Brillouin Scattering," in *2009 International Topical Meeting on Microwave Photonics*, Oct. 2009, pp. 1–4.

[106] R. J. Mailloux, *Phased Array Antenna Handbook*, 2nd edition. Artech House Publishing Co., 2000.

[107] I. Frigyes and A. J. Seeds, "Optically generated true-time delay in phased-array antennas," *IEEE Transactions on Microwave Theory and Techniques*, vol. 43, no. 9, pp. 2378–2386, Sep. 1995, doi: 10.1109/22.414592.

[108] R. D. Esman *et al.*, "Fiber-optic prism true time-delay antenna feed," *IEEE Photonics Technology Letters*, vol. 5, no. 11, pp. 1347–1349, Nov. 1993, doi: 10.1109/68.250065.

[109] K. Ito, M. Suga, Y. Shirato, N. Kita, and T. Onizawa, "Remote Beamforming Scheme With Fixed Wavelength Allocation for Radio-Over-Fiber Systems Employing Single-Mode Fiber," *Journal of Lightwave Technology*, vol. 40, no. 4, pp. 997–1006, Feb. 2022, doi: 10.1109/JLT.2021.3127529.

[110] B.-M. Jung and J. Yao, "A Two-Dimensional Optical True Time-Delay Beamformer Consisting of a Fiber Bragg Grating Prism and Switch-Based Fiber-Optic Delay Lines," *IEEE Photonics Technology Letters*, vol. 21, no. 10, pp. 627–629, May 2009, doi: 10.1109/LPT.2009.2015275.

[111] S. R. Forrest and R. B. Taylor, "Optically controlled phased array radar," in *International Topical Meeting on Microwave Photonics. MWP '96 Technical*

Digest. Satellite Workshop (Cat. No.96TH8153), Dec. 1996, pp. 193–196. doi: 10.1109/MWP.1996.662119.

[112] M. Burla *et al.*, "Integrated Photonic Ku-Band Beamformer Chip With Continuous Amplitude and Delay Control," *IEEE Photonics Technology Letters*, vol. 25, no. 12, pp. 1145–1148, Jun. 2013, doi: 10.1109/LPT.2013.2257723.

[113] H. Chi, F. Zeng, and J. Yao, "Photonic Generation of Microwave Signals Based on Pulse Shaping," *IEEE Photonics Technology Letters*, vol. 19, no. 9, pp. 668–670, May 2007, doi: 10.1109/LPT.2007.894979.

[114] R. Adams, R. Ashrafi, J. Wang, M. R. Dizaji, and L. R. Chen, "RF-Arbitrary Waveform Generation Based on Microwave Photonic Filtering," *IEEE Photonics Journal*, vol. 6, no. 5, pp. 1–8, Oct. 2014, doi: 10.1109/JPHOT.2014.2361637.

[115] L. A. Bui, "A Review of Photonic Generation of Arbitrary Microwave Waveforms," *Progress In Electromagnetics Research B*, vol. 75, pp. 1–12, 2017, doi: 10.2528/PIERB17011201.

[116] V. Torres-Company, J. Lancis, P. Andres, and L. R. Chen, "Reconfigurable RF-Waveform Generation Based on Incoherent-Filter Design," *Journal of Lightwave Technology*, vol. 26, no. 15, pp. 2476–2483, Aug. 2008, doi: 10.1109/JLT.2008.925629.

[117] M. Bolea, J. Mora, B. Ortega, and J. Capmany, "Photonic arbitrary waveform generation applicable to multiband UWB communications," *Opt. Express, OE*, vol. 18, no. 25, pp. 26259–26267, Dec. 2010, doi: 10.1364/OE.18.026259.

[118] J. Yao, F. Zeng, and Q. Wang, "Photonic Generation of Ultrawideband Signals," *Journal of Lightwave Technology*, vol. 25, no. 11, pp. 3219–3235, Nov. 2007, doi: 10.1109/JLT.2007.906820.

[119] M. Bolea, J. Mora, B. Ortega, and J. Capmany, "Optical UWB pulse generator using an N tap microwave photonic filter and phase inversion adaptable to different pulse modulation formats," *Opt. Express, OE*, vol. 17, no. 7, pp. 5023–5032, Mar. 2009, doi: 10.1364/OE.17.005023.

[120] M. Bolea, J. Mora, B. Ortega, and J. Capmany, "High-order UWB pulses scheme to generate multilevel modulation formats based on incoherent optical sources," *Opt. Express*, vol. 21, no. 23, p. 28914, Nov. 2013, doi: 10.1364/OE.21.028914.

[121] 3GPP, "ETSI TS 138 141-2 V16.4.0," 2020. [Online]. Available: https://www.etsi.org/deliver/etsi_ts/138100_138199/13814102/16.04.00_60/ts_13814102v160400p.pdf

[122] G. Rademacher, B. J. Puttnam, R. S. Luis, Y. Awaji, and N. Wada, "Time-dependent crosstalk from multiple cores in a homogeneous multi-core fiber," in *2017 Optical Fiber Communications Conference and Exhibition (OFC)*, Mar. 2017, pp. 1–3.

[123] G. Agrawal, *Fiber-Optic Communication Systems*, 3rd edition. Wiley, 2007.

[124] P. A. Merritt, R. P. Tatam, and D. A. Jackson, "Interferometric chromatic dispersion measurements on short lengths of monomode optical fiber," *Journal of Lightwave Technology*, vol. 7, no. 4, pp. 703–716, Apr. 1989, doi: 10.1109/50.19099.

[125] M. Ureña, I. Gasulla, F. J. Fraile, and J. Capmany, "Modeling optical fiber space division multiplexed quantum key distribution systems," *Opt. Express, OE*, vol. 27, no. 5, pp. 7047–7063, Mar. 2019, doi: 10.1364/OE.27.007047.

[126] A. V. T. Cartaxo and T. M. F. Alves, "Discrete Changes Model of Inter-core Crosstalk of Real Homogeneous Multi-core Fibers," *Journal of Lightwave Technology*, vol. 35, no. 12, pp. 2398–2408, Jun. 2017, doi: 10.1109/JLT.2017.2652067.

[127] Fibercore, "Multicore fiber datasheet." [Online]. Available: https://fibercore.humaneticsgroup.com/products/multicore-fiber/multicore-fiber/sm-7c150061125.

[128] J. Tu, K. Saitoh, M. Koshiba, K. Takenaga, and S. Matsuo, "Design and analysis of large-effective-area heterogeneous trench-assisted multi-core fiber," *Opt. Express, OE*, vol. 20, no. 14, pp. 15157–15170, Jul. 2012, doi: 10.1364/OE.20.015157.

[129] L. Gruner-Nielsen *et al.*, "Dispersion-compensating fibers," *Journal of Lightwave Technology*, vol. 23, no. 11, pp. 3566–3579, Nov. 2005, doi: 10.1109/JLT.2005.855873.

[130] R.-J. Essiambre, G. Kramer, P. J. Winzer, G. J. Foschini, and B. Goebel, "Capacity Limits of Optical Fiber Networks," *Journal of Lightwave Technology*, vol. 28, no. 4, pp. 662–701, Feb. 2010, doi: 10.1109/JLT.2009.2039464.

[131] H. Takeshita *et al.*, "First Demonstration of Uncoupled 4-Core Multicore Fiber in a Submarine Cable Prototype with Integrated Multicore EDFA," in *2022 Optical Fiber Communications Conference and Exhibition (OFC)*, Mar. 2022, pp. 1–3.

[132] B. P. Pal, "CHAPTER 1 - Optical Fibers for Broadband Lightwave Communication: Evolutionary Trends in Designs," in *Guided Wave Optical Components and Devices*, B. P. Pal, Ed., Burlington: Academic Press, 2006, pp. 1–25. doi: 10.1016/B978-012088481-0/50002-4.

[133] L. Grüner-Nielsen, K. G. Jespersen, D. Jakobsen, and K. S. Feder, "A dispersion compensating fiber with a factor 5 improvement in figure of merit and a factor 4.5 improvement in effective area," in *2011 Optical Fiber Communication Conference and Exposition and the National Fiber Optic Engineers Conference*, Mar. 2011, pp. 1–3.

[134] J. L. Auguste *et al.*, "Conception, Realization, and Characterization of a Very High Negative Chromatic Dispersion Fiber," *Optical Fiber Technology*, vol. 8, no. 1, pp. 89–105, Jan. 2002, doi: 10.1006/ofte.2002.0370.

[135] J. T. Winthrop and C. R. Worthington, "Theory of Fresnel Images. I. Plane Periodic Objects in Monochromatic Light*," *J. Opt. Soc. Am., JOSA*, vol. 55, no. 4, pp. 373–381, Apr. 1965, doi: 10.1364/JOSA.55.000373.

[136] J. Azaña and M. A. Muriel, "Temporal Talbot effect in fiber gratings and its applications," *Appl. Opt., AO*, vol. 38, no. 32, pp. 6700–6704, Nov. 1999, doi: 10.1364/AO.38.006700.

[137] T. Jannson and J. Jannson, "Temporal self-imaging effect in single-mode fibers," *J. Opt. Soc. Am., JOSA*, vol. 71, no. 11, pp. 1373–1376, Nov. 1981, doi: 10.1364/JOSA.71.001373.

[138] R. Maram, L. Romero Cortés, and J. Azaña, "Programmable Fiber-Optics Pulse Repetition-Rate Multiplier," *Journal of Lightwave Technology*, vol. 34, no. 2, pp. 448–455, Jan. 2016, doi: 10.1109/JLT.2015.2500538.

[139] M. Seghilani, R. Maram, L. R. Cortés, and J. Azaña, "Generation of a 128-GHz optical pulse train from a 250-MHz frequency comb using temporal self-imaging," in *2017 IEEE Photonics Conference (IPC)*, Oct. 2017, pp. 141–142. doi: 10.1109/IPCon.2017.8116041.

[140] G. Agrawal, *Nonlinear Fiber Optics*, 5th edition, Academic Press, 2013.

[141] A. Ferrando, E. Silvestre, J. J. Miret, and P. Andrés, "Nearly zero ultraflattened dispersion in photonic crystal fibers," *Opt. Lett., OL*, vol. 25, no. 11, pp. 790–792, Jun. 2000, doi: 10.1364/OL.25.000790.

[142] F. Ye, J. Tu, K. Saitoh, and T. Morioka, "Simple analytical expression for crosstalk estimation in homogeneous trench-assisted multi-core fibers," *Opt. Express, OE*, vol. 22, no. 19, pp. 23007–23018, Sep. 2014, doi: 10.1364/OE.22.023007.

[143] F. Y. M. Chan, A. P. T. Lau, and H.-Y. Tam, "Mode coupling dynamics and communication strategies for multi-core fiber systems," *Opt. Express, OE*, vol. 20, no. 4, pp. 4548–4563, Feb. 2012, doi: 10.1364/OE.20.004548.

[144] I. Gasulla and J. M. Kahn, "Performance of Direct-Detection Mode-Group-Division Multiplexing Using Fused Fiber Couplers," *J. Lightwave Technol., JLT*, vol. 33, no. 9, pp. 1748–1760, May 2015.

[145] A. Macho, M. Morant, and R. Llorente, "Unified Model of Linear and Nonlinear Crosstalk in Multi-Core Fiber," *Journal of Lightwave Technology*, vol. 34, no. 13, pp. 3035–3046, Jul. 2016, doi: 10.1109/JLT.2016.2552958.

[146] R. O. J. Soeiro, T. M. F. Alves, and A. V. T. Cartaxo, "Inter-core crosstalk in weakly coupled MCFs with arbitrary core layout and the effect of bending and twisting on the coupling coefficient," *Opt. Express, OE*, vol. 27, no. 1, pp. 74–91, Jan. 2019, doi: 10.1364/OE.27.000074.

[147] Y. Wang, T. Fujisawa, and K. Saitoh, "Analytical expression for mode-coupling coefficient between non-identical step-index cores and its application to multi-core fiber design within 125-μm cladding diameter," *Optics Communications*, vol. 506, p. 127552, Mar. 2022, doi: 10.1016/j.optcom.2021.127552.